Università degli Studi di Padova

Dipartimento di Ingegneria Industriale (DII)
Corso di Laurea Magistrale in Ingegneria dell'Energia Elettrica

Tesi di Laurea Magistrale

Design of Electric Motors for a Hybrid Farming Tractor

Studente
Elia Scolaro
Matricola 1197578

Relatore
Prof. Luigi Alberti

Correlatore
Dott. Diego Troncon

Anno Accademico 2019-2020

Contents

Riassunto esteso

In questa tesi viene presentato uno studio di fattibilità sull'elettrificazione del powertrain di un trattore agricolo da campo aperto. Il principale obiettivo è fornire utili risultati e validare metodologie pratiche per la progettazione di motori elettrici per trattori ibridi. In particolare in questo progetto sono stati dimensionati tre motori a magnete permanente superficiale a flusso radiale raffreddati a liquido.

L'elettrificazione delle macchine agricole negli ultimi anni ha iniziato ad assumere maggior rilievo nella letteratua tecnico-scientifica, spinta dal crescente interesse da parte delle aziende operanti nel settore. Sebbene già da circa un decennio siano stati pubblicati studi di fattibilità e analisi di scenario riguardo l'introduzione di trattori ibidi ed anche puramente elettrici, solo recentemente si sta iniziando a valuatare seriamente la loro industrializzazione. La spinta all'elettrificazione proviene in particolar modo dalle nuove legislazioni sulle emissioni. Infatti le recenti normative emenate sia nell'Unione Europea (Stage V) sia negli Stati Uniti (Tier 4) impongono stringenti limitazioni alle emissioni dei *Non-Road Mobile Machinery* (NRMM), categoria nella quale rientrano tutte le macchine agricole. Tali normative constringono all'introduzione di catalizzatori, filtri per il particolato e raccoglitori per gli oli esausti nei motori Diesel di tutti i trattori agricoli di nuova immatricolazione. Questi componenti rendono i motori più voluminosi e costosi. Quindi, parallelamente alla proposta di modelli di agricoltura a bassa meccanizzazione, sta riscontrando un crescente interesse l'elettrificazione dei veicoli agricoli, con il fine di seguire quanto si è già fatto e si sta facendo nell'industria automobilistica. Benchè la linea di sviluppo delineta possa essere simile a quanto fatto in campo automotive, con una prima introduzione di veicoli ibridi per poi passare progressivamente a powertrain totalmente elettrici, è già stato messo in luce come l'elettrificazione dei trattori presenti una complessità maggiore, a causa delle peculiarità delle macchine agricole che le distinguono largamente dai veicoli stradali. Rispetto a questi ultimi infatti è stato evidenziato che gli azionamenti elettrici nei trattori agricoli dovranno soddisfare requisiti diversi, poichè in questa applicazione la trazione rappresenta spesso solo una parte della coppia di carico richiesta. Infatti molte operazioni in agricoltura richiedono il traino di macchinari azionati dal motore del trattore tramite una presa di forza meccanica esterna (PTO: *Power Take Off*). Non sono poi trascurabili i carichi dovuti alle pompe dell'olio dei circuiti idraulici del servosterzo, nonché di alcuni tipi di macchinari che necessitano anche di una presa di forza idraulica. Inoltre nemmeno il carico di trazione è paragonabile ai ben noti cicli di lavoro standardizzati usati in campo automobilistico, poiché in agricoltura è frequente il traino di utensili (aratri, estirpatrici, ecc...) che richiedono coppie impulsive e molto oscillanti, come si potrà anche vedere nel corso di questa trattazione.

Durante questo lavoro di tesi è stata studiata l'elettrificazione del powertrain di un trattore agricolo da campo aperto da 280 $[Hp]$. Lo scopo è dimensionare un motore elettrico per trasformare il powertrain tradizionale del trattore in un ibrido. Il progetto è focalizzato in particolar modo sulla progettazione del motore elettrico, ma per la scelta delle specifiche di progetto è stata necessaria un'analisi del veicolo ibrido ed una sua modelizzazione semplificata. Inoltre nel corso del progetto si sono anche individuate alcune specifiche utili per la progettazione degli altri componenti dell'azionamento, quali l'inverter ed il pacco batteria, nonstante questi aspetti non siano stati approfonditi in dettaglio.

Durante il lavoro di tesi sono state utilizzate ed elaborate alcune misurazioni dei profili di coppia e velocità all'albero motore effettuate sul trattore in esame durante quattro diverse operazioni agricole. Le misurazioni sono state rese disponibli per questo lavoro di tesi nell'ambito del progetto PRIN 2017 intitolato *'Green SEED: Design of more-electric tractors for a more*

sustainable agriculture'. Tali dati sono stati essenziali per ricavare verosimili specifiche di progetto per la macchina elettrica e per dedurre o almeno ipotizzare le informazioni non disponibili riguardo al veicolo. In particolare il motore Diesel originale è stato ipotizzato comparando la caratteristica meccanica fornita nelle schede tecniche commerciali di alcuni motori ad uso agricolo con i punti di lavoro coppia-velocità e potenza-velocità estrapolati dalle misurazioni, per vedere quale profilo si adattasse meglio ai cicli di lavoro. Una volta scelto il motore termico del powertrain tradizionale, si sono selezionati anche tre motori di potenza via via inferiore, per studiare l'elettrificazione a grado di ibridazione crescente, cioè con un motore Diesel sempre più sottodimensionato ed una maggior richiesta di potenza alla macchina elettrica. Per il powertrain ibrido si è scelta un'architettura parallelo, con il motore elettrico calettato direttamente all'albero motore. Il motore elettrico e quello termico dunque lavorano sempre alla stessa velocità, se si trascurano i transitori meccanici. In questo studio preliminare si è deciso di adottare una semplice strategia di controllo (*power management*) a soglia, in cui è previsto che il carico meccanico venga bilanciato interamente dal motore Diesel fino ad una certa soglia prestabilita, oltre la quale interviene in aggiunta il motore elettrico per compensare i picchi di potenza richiesta. In tale sistema di controllo non è contemplata la ricarica del pacco batteria con veicolo acceso, in quanto non è previsto un eccesso di potenza da parte del motore termico rispetto al carico.

La richiesta di coppia e potenza al motore elettrico è stata calcolata simulando il bilancio di potenza all'albero motore attraverso un circuito meccanico. Le coppie di carico imposte nel circuito sono state ottenute dalle misurazioni disponibili nei quattro cicli di lavoro, mentre la coppia data dal motore termico è stata ricavata dalla caratteristica meccanica considerando il *power management* adottato. I test di ibridazione sono stati effettuati considerando sia le caratteristiche meccaniche di motori Diesel ad uso agricolo di potenza inferiore sia scalando la caratteristica meccanica del motore termico originale. E' stato provato che non c'è una differenza significativa tra le due procedure, nonstante i motori scelti siano forniti da produttori diversi. I profili di coppia e potenza richiesta alla macchina elettrica sono stati poi processati con un filtro passa-basso provando diverse costanti di tempo. La costante di tempo del filtro approssima la costante di tempo termica del motore. Le specifiche di coppia del motore elettrico infatti sono state scelte seguendo il metodo della coppia termica equivalente. Il concetto alla base di tale approccio, ampiamente usato in campo automotive, consiste nello scegliere un valore di coppia nominale inferiore alla massima coppia richiesta in modo che i picchi vengano compensati in sovraccarico, senza però pregiudicare la tenuta termica della macchina, in particolare dell'isolante in cava e dei magneti. Infatti con coppie nominali più basse, a parità di velocità, in genere si ottengono motori più compatti ed economici. Per identificare le specifiche di progetto quindi la dinamica del motore deve essere inizialmente ipotizzata, in particolare si è supposto un valore per la costante di tempo termica.

Tre motori elettrici a magnete permanente superficiale a flusso radiale sono stati dunque dimensionati per uno dei tre gradi di ibridazione analizzati. I motori differiscono principalmente nel numero di poli. Questa tipologia di motore è stata scelta per la sua elevata densità di potenza e perchè è particolarmente adeguato in applicazioni a velocità relativamente basse, come quella affrontata in questa tesi. La scelta del tipo di magnete come anche del numero di poli è stata giustificata. Inoltre per ottimizzare lo spazio occupato e soddisfare i vincoli di volume, un particolare dimensionamento preliminare è stato effettuato, tenendo conto sin da subito delle testate e del totale ingombro assiale. Diversi tentativi di dimensinamento sono stati eseguiti, variando il numero di cave, lo spessore ed il grado del magnete. La scelta delle dimensioni principali delle tre macchine è stata effettuata favorendo la compattezza e l'economicità. Si è proseguito dunque con il dimensionamento dell'avvolgimento, della lamiera di statore e di rotore. Una stima del costo dei materiale è stata effettuata alla fine della sintesi elettromagnetica delle tre macchine.

Le prestazioni dei motori sono state poi valuate con analisi agli elementi finiti e stime analitiche. Si sono verificate le prestazioni a vuoto, calcolando la saturazione della macchina, la forza elettromotrice e la coppia di impuntamento. Dunque si sono ricavate la coppia a carico nominale ed in massimo sovraccarico con relativo *ripple*. Sono stati calcolati la resistenza e l'induttanza sincrona e si è valutata di conseguenza la tensione richiesta dall'avvolgimento a carico nominale ed in massimo sovraccarico, con il relativo fattore di potenza. Anche le

perdite e l'efficienza della macchina sono state stimate. In particolare nel calcolo delle perdite nel ferro e nei magneti con gli elementi finiti si sono considerati anche i contributi dovuti al contenuto armonico dell'induzione nonchè la presenza di una componente armonica nella corrente di alimenatzione a frequenza di switching causata dalla PWM dell'inverter.

E' stato poi dimensionato il sistema di raffreddamento. Si è scelta un camicia esterna in acciaio inox con un condotto a spirale lungo la circonferenza esterna del pacco lamiere. Il liquido refrigerante è una soluzione antigelo di acqua-glicole. La geometria della camicia ed il circuito idraulico (il condotto di raffreddamento) sono stati progettati imponendo lo scambio termico convettivo richiesto per smaltire le perdite precedentente calcolate ed attraverso delle stime analitiche, avvalendosi dei numeri adimensionali che caraterizzano la fluidodinamica. Infine si è analizzato il comportamento termico della macchina a regime sotto carico nominale ed in transitorio durante i cicli di lavoro disponibili. La mappa termica a regime è stata ottenuta con gli elementi finiti, mentre le simulazioni in transitorio sono state effettuate con una rete termica equivalente a parametri concentrati.

Sebbene la costante di tempo termico effettiva risulti molto inferiore a quella supposta inizialmente a causa dei volumi contenuti dei motori, le sovratemperature durante il ciclo di lavoro più critico non superano il massimo valore ammesso dalla classe di isolamento scelta e dalla classe termica del magnete. Ciò nonostante la soglia di sicurezza raccomandata dalla normativa IEC è abbondantemente superata. Pertanto le prestazioni di coppia in sovraccarico dei motori deveono essere limitate per evitare danni ai materiali isolanti e perdite permanenti di isolamento elettrico. Tale calo delle prestazioni può essere accettato nei veicoli agricoli, nei quali non sono fondamentali grandi accelerazioni. Per gli altri cicli di lavoro infatti non si riscontrano problemi termici.

In questa tesi si è affrontato il dimensionamento e l'analisi di motori elettrici per un'applicazione non ancora studiata approfonditamente in letteratura scientifica. Quindi, nonstante i risultati raggiunti, il lavoro svolto si presta a molti possibili ulteriori sviluppi.

Introduction

In recent years the electrification of farming tractors has gained more relevance in the technical research [1], thanks to an increasing interest from the companies involved in the market of agricultural machinery [2]. Despite in the last decade some investigations have been proposed in the technical literature about both hybrid electric tractors (HETs) [3] and pure electric agricultural machinery (BETs: *Battery Electric Tractors*, FCETs: *Fuel Cell Electric Tractors*) [4], only now the industrialization of such vehicles is beginning to be seriously considered.

This growing interest is mainly due to the more strictly emissions regulations issued recently (2019-2020) both in the European Union (Stage V standard) [5] and in the United States (Tier IV standard) [6], that prescribe very low particulate emissions for the so-called non-road mobile machinery (NRMM), to which the farming tractors belong. The admissible threshold of emissions for the new agricultural vehicles has been lowered a lot, thus to observe the new standards the Diesel engines, which are installed on farming tractors almost worldwide, must be equipped with particulate filters (SCR: *Selective Catalytic Reducer*, DPF: *Diesel Particulate Filter*) and tanks for the exhaust oils. Such components make the engines more complex, bulky and expensive.

While the electric auxiliaries (fans, pumps, cooling systems,...) has been implemented in NRMMs since long ago [7], the powertrain electrification is still in an initial stage if compared to the on-road vehicles. Regarding this topic some progress have been done in case of wheel loaders [8] and robotic tractors [9], but for farming vehicles only few proposals have been made [3], [10], [11]. It has been underlined how the electric drives must fulfill different specifications than the ones commonly adopted in on-road vehicles. Indeed in such application the traction is only a limited part of the overall effort because the agricultural work often requires the pulling of various tools that need to be powered from the engine through a mechanical power take-off (PTO). Furthermore hydraulic loads such as power-steering pumps and lifting implements cannot be neglected. Moreover neither the traction load is comparable to the standard duty cycles commonly adopted in the automotive field, because operations such plowing and harrowing require high-varying and pulse torque, as it will be also presented in this thesis.

Even though the research is at the beginnings, the development course that has just interested electric cars and motorbikes could also be followed in this field [12]. At first the development of hybrid powertrains can be planned: starting from mild-hybrid tractors, where the electric motor will satisfy only the peak loads, full-hybrid powertrains will be gradually developed through a step-by-step downsizing of the Diesel engine. The electrical machine power capability will increase until the load could be entirely fulfilled in pure electric mode at least during light duty cycles. The electrification of auxiliaries and hydraulic circuits could be also involved in this first stage of the development course. Drive-by-wire systems have been proposed in place of the hydraulic power-steering [4]. The vehicle size and in particular the chassis should remain unchanged as much as possible to make the industrialization easier. So the power take off will be still mechanical.

For the hybrid powertrain the same architectures implemented in on-road vehicles have been proposed: series, parallel and power-splitter [13]. Scenarios forecasting and economic assessments have been presented in the technical literature [14] to evaluate which could be the best choices for a hybrid electric tractor. Lately a project regarding the design and analysis of a SPM motor (*Surface Permanent Magnet*) to electrify the powertrain of a specialized tractor for orchards and vineyards has been proposed in [10], [15].

In a second development stage the electrification of the PTO and the related implements will

be carried out. Finally the feasibility of pure electric tractors will be assessed. Prototypes of small-size electric agricultural machinery have been already manufactured for research purposes [11] and investigations about the charging systems as well as the power electronics and the battery packs have been just presented in literature [16].

The project presented in this thesis belongs to the context above described. The main goal is the assessment of the thermal equivalent torque approach as a design method for SPM motors in a hybrid electric farming tractor. The project follows what has been done by D. Troncon *et al.* in [10], [15] for a specialized farming vehicle, but a $280\,[Hp]$ open field tractor is here considered. A parallel architecture has been adopted for the hybrid powertrain: the electric motor has been supposed directly installed on the engine shaft, as it is usually done in mild-hybrid vehicles [13]. The power-management is based on a simple threshold logic [13], so that the electrical machine works only to boost the engine. An original Diesel engine have been chosen among commercial datasheets looking at some available torque and speed measurements taken on an open field farming tractor during four different agricultural operations. These data have been measured in the frame of the PRIN 2017 project entitled *'Green SEED: Design of more-electric tractors for a more sustainable agriculture'*. Then the available torque and speed trends have been used as inputs in a Simulink® mechanical circuit that model the power balance at the engine shaft. Three downsized engines with decreasing rated power have been selected to simulate growing hybridization factors. The torque required to the electric motor in each simulation has been processed through a low pass filter with various time constants to estimate the equivalent thermal torque. So the specifications needed to start the preliminary sizing of the electrical machines have been chosen supposing a thermal time constant and looking at the resulting torque trends. Then three SPM motors with a different number of poles have been designed. Displacement constrains have been evaluated and a particular preliminary sizing method has been implemented to cope with them. The machines main dimensions have been selected among different sizing attempts preferring the compactness and the cost-effectiveness. To assess the torque performances and evaluate the losses and efficiency a detailed electromagnetic analysis have been carried out on the designed machines both with analytical computations and FEA (*Finite Element Analysis*), using MATLAB® and the open source software FEMM, developed by David Meeker [17]. Finally the thermal behavior of the motors have been analyzed: the steady state condition at rated load has been simulated with the thermal solver implemented in FEMM (FEH: *Finite Element Heating*), while the step responses and the overtemperatures trends during the four real duty cycles have been obtained by means of an equivalent lumped parameters thermal network implemented in Simulink®. Hence the actual thermal time constant has been computed from the step responses and the resulting slot and magnet overtemperture trends have been compared to the expected ones.

The design of the other components of the electric drive, i.e. the inverter and the battery pack, as well as a detailed sizing of the mechanical parts are not covered in this thesis. However some information will be provided in order to give a starting point for further developments on these topics. Indeed one of the aims of this work is to give valid results and suggestions that could be useful in further electrification projects for farming tractors and agricultural machinery.

Chapter 1

Powertrain electrification

The electrification of an open field farming tractor will be presented in this first chapter.

After a brief classification of electric hybrid vehicles examining the hybridization factor, the original powertrain and a proposed hybrid architecture will be schematically described through a systemic point of view. Thus the description will be focused on the tasks and the significant features of the main components involved in power generation and transmission inside both powertrains, so that the most relevant differences between the original architecture and the electrified one are standing out. A very simple power management has been chosen for the proposed hybrid tractor: its operating workflow will be explained in order to highlight how it affects the performances of the vehicle and the technical requirements of the powertrain components. Meanwhile, advantages and drawbacks of the previously mentioned choices will be discussed.

1.1 Hybridization factor

An electric hybrid vehicle has two main mechanical power sources and two related energy sources: an internal combustion engine (ICE) whose injection system is fed by a fuel tank and an electrical machine (EM) driven by a power electronics unit and fed by a battery pack, or, in rare cases, by a fuel cell with a hydrogen tank. The ICE and EM work together to satisfy as best as possible all the mechanical loads of the vehicle. The cooperation between the ICE and the EM is supervised by the power management system of the vehicle which prescribes the working rules and dictates the input parameters for the driving controls of the engine and the electric motor, i.e. speed or torque references. Battery charge is also managed through the EM. A lot of different power management logics can be implemented, depending on the hybrid powertrain architecture and the duty cycles of the vehicle [13, 18, 19].

An electric hybrid vehicle can be classified looking at the hybridization factor H (or DOH: *degree of hybridization* [19, 20]) that is defined as the ratio between the rated power of the electrical machine P_{EM} and the total rated power of the powertrain, which is the sum of the rated power of the ICE P_{ICE} with P_{EM}:

$$H = \frac{P_{EM}}{P_{ICE} + P_{EM}} \tag{1.1}$$

The hybridization factor is an index expressing how much the powertrain is electrified. The definition of H does not consider other electric motors that can be mounted on the vehicle to power auxiliaries, such as pumps, air-cooling fans, electric servo-steering system, etc. H concerns only the powertrain and takes into account only the electric motor that develops torque for the main mechanical loads. It is relevant to notice that $H = 0\%$ means a traditional non-electrified powertrain ($P_{EM} = 0$) while $H = 100\%$ means a full electric vehicle ($P_{ICE} = 0$). Relating to the value of H, electric hybrid vehicles can be classified as presented in Table 1.1. Values of H in Table 1.1 stop at 60% as above this value an hybrid architecture has no longer advantages but a full electric powertrain is much more worthwhile [13, 18]. The classification

H [%]	**Hybrid type**
$0-5$	Light-hybrid
$5-20$	Mild-hybrid
$20-60$	Full-hybrid

Table 1.1: Electric hybrid vehicles classification

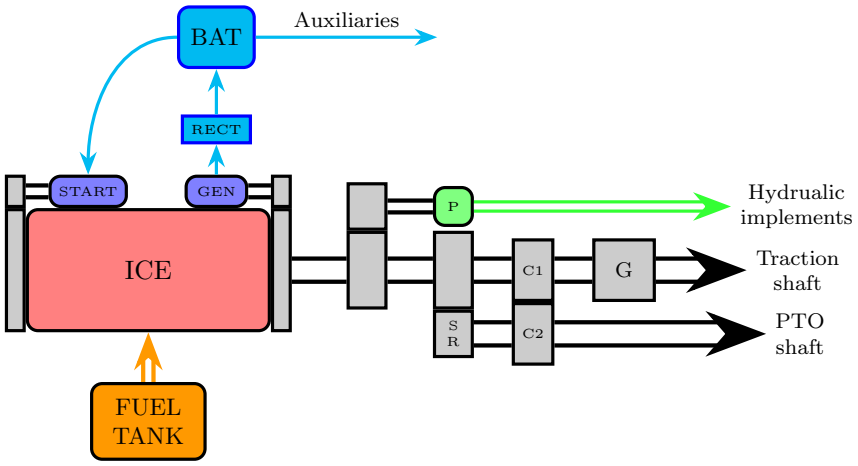

Figure 1.1: Original powertrain outline

in Table 1.1 is not overall accepted but the reported ranges of H vary slightly between different literature papers.

1.2 Original powertrain

The powertrain of a common open-field farming tractor is outlined in Figure 1.1. It is assumed to be the original powertrain under analysis as it is the most widespread architecture for agricultural machinery.

The main power source is an internal combustion engine (ICE). Open-field tractors with rated power higher than $100-120\,[Hp]$ usually have a turbocharged Diesel engine with in-line cylinders and electronic or hydraulic controlled common-rail injection. The ICE converts the chemical energy stored in the fuel, i.e. Diesel oil, into rotational mechanical energy and makes it available at the engine shaft.

The rotational energy can be directly converted into electric energy by a three-phase generator (GEN) that charges the battery pack (BAT) through a static conversion group (RECT) when required by the vehicle's ECU (Electronic Control Unit). The conversion group denoted with RECT is usually composed by a three-phase diodes rectifier followed by a DC-DC voltage-conditioning stage with a boost topology. In older tractors the generator could be even a dynamo and in such case there is no need for the diodes rectifier. The ICE is unable to start by itself: it cannot develop torque at null speed. So an electric motor, i.e. the starter (START), has the task to develop a sufficient torque to put the crankshaft in rotation, so that the engine pistons can do an adequate air compression inside the cylinders to ignite the first combustion process. The starter is almost always a DC motor designed to develop an high starting torque and being able to be fed safely by the battery. The generator and the starter are placed respectively in the engine's rear end and front end. Usually both of them are connected to the engine shaft through speed reducers, i.e. torque multipliers, as generally electrical machines exploit better high speed rates rather than high torque capabilities. In some new commercial tractors the generator and the starter tasks are often performed by the same electrical machine named ISA (Integrated Starter Alternator), resulting in a so-called light-hybrid powertrain architecture. ISAs are driven by bidirectional power electronics units that are able to guarantee both

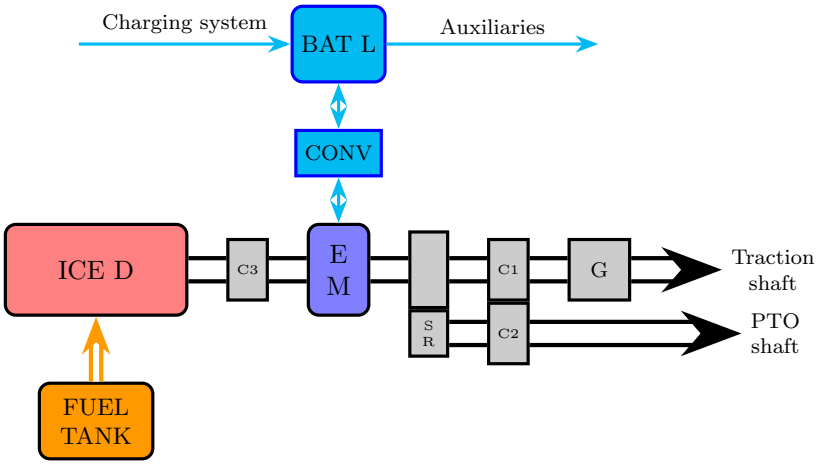

Figure 1.2: Hybrid powertrain outline

the battery discharging during the starting phases and the battery charging when required by the ECU.

Commonly the battery is a lead-acid valve regulated accumulator with a high power density in order to provide intensive discharges during the starts (currents peak values up to 1000 $[A]$), but a lower energy density; so when the engine is working the accumulator can be continuously recharged through the generator and a small capacity is sufficient to feed all the electrical auxiliaries, i.e. fans, lights, control electronics, etc.

The mechanical load applied at the engine shaft are represented by the traction effort, a mechanical power take off (PTO), some hydraulic implements and the already described generator. Traction effort requires the transmission of mechanical energy to the driving wheels' axles, that could be the rear wheels or all the four wheels in the 4x4 architectures. At the same time mechanical energy should be available even for the PTO shaft when the agricultural operations require the use of external implements such as pumps, power harrows, atomizers etc. The ICEs' are not suitable for traction purpose because they have a low torque capability, especially at low speed rates. So, as it happens for on-road vehicles, the engine's mechanical characteristics must be adapted to traction's power requirements with the help of a multi-gear transmission system (G) connected to the engine shaft through a clutch (C1). Farming tractors' transmission systems are much more complex than those commonly implemented in on-road vehicles due to the great diversity of agricultural operations. Furthermore, the mechanical PTO often is involved in the work together with traction. The analysis of the mechanical transmissions of farming tractors is not in the aims of this thesis. A lot of solutions can be implemented but, as far as this study concerns, only a double clutch (C2) with a speed reducer (SR) on the PTO shaft's side is considered as mechanical connection between the power source, i.e. the ICE, and the mechanical loads, i.e. traction and PTO. Hydraulic-powered implements such as rear or front lifts should be also taken into account: these loads require hydraulic circuits where the fluid, i.e. oil, is elaborated by pumps (P) that are powered by the engine.

During the last decade a lot of new technologies have been implemented in the field of agricultural machinery. More efficient and environmentally friendly Diesel engines with new control and management systems have been developed [21, 22], following the increasingly limiting European and American regulations on non-road vehicles' emissions. Self-driving tractors along with more safe and comfortable machinery are now available on the market [23]. Nevertheless the powertrain architecture outlined in Figure 1.1 has not gone through substantial changes, despite the variety of solutions proposed in recent years in the technical literature [4].

1.3 Hybrid powertrain

The hybrid powertrain proposed in this study is outlined in Figure 1.2.

The original ICE is replaced by a downsized Diesel engine (ICE D) of the same type, i.e. turbocharged in-line cylinders with common-rail injection. To cover the power capability lost due to the ICE downsizing an electric motor (EM) is included in the powetrain. The proper design of this electric machine is the main purpose of this thesis. The EM shaft is connected to the engine shaft through the clutch (C3). Thus the ICE and the EM are mechanically in parallel because the torque developed by ICE τ_{ICE} and the torque developed by the EM τ_{EM} sum up to balance the load torque τ_L at the shaft. So it can be stated that this hybrid powertrain has a parallel architecture. In the parallel architectures the ICE and the EM are mechanically connected through a torque adder [13, 18], a mechanical transmission device that, neglecting any dissipation due to frictions, does a weighted sum of the input torques τ_{ICE} and τ_{EM} to balance the load torque τ_L imposed by the vehicle duty cycle:

$$\tau_L = g_{ICE}\tau_{ICE} + g_{EM}\tau_{EM} \tag{1.2}$$

Where g_{ICE} and g_{EM} are dimensionless weights that depends on how the torque adder is physically made. The device working principle must fulfill the instantaneous mechanical power balance:

$$p_L = p_{ICE} + p_{EM}$$

Where p_L, p_{ICE} and p_{EM} are respectively the load, engine and electric motor instantaneous power. Remembering that the mechanical power $p\,[W]$ can be expressed as the product of instantaneous torque $\tau\,[Nm]$ by instantaneous rotational speed $\omega\,[rad/s]$, the power balance can be written as follows:

$$\tau_L\omega_L = \tau_{ICE}\omega_{ICE} + \tau_{EM}\omega_{EM}$$

Consequently, substituting τ_L of Equation 1.2 in the previous expression yields to the following relations, where it is stated that both the rotational speed of the ICE ω_{ICE} and the EM ω_{EM} are binded to the speed required by the driver ω_L:

$$\begin{cases} \omega_{ICE} = g_{ICE}\omega_L \\ \omega_{EM} = g_{EM}\omega_L \end{cases} \tag{1.3}$$

In full-hybrid vehicles with parallel architectures, the torque adder is usually realized with a set of three cogged gears as represented in the schematic drawing of Figure 1.3 [13]. In this implementation the weights g_{ICE} and g_{EM} depend on the ratio between the gears diameters. So during the powertrain design the most suitable values can be chosen to fit as best as possible the features of the engine and the EM. Generally this solution leads to an easier design of the EM because the machine can be sized for a high rated speed and a low rated torque, with a benefit in efficiency too. Nevertheless, an easier implementation of the torque adder has been adopted in this project, which is quiet common in mild-hybrid vehicles. The device consists of a single shaft shared between the ICE and the EM, except for the clutch C3. In this case the coefficients g_{ICE} and g_{EM} are both equal to 1 and Equations 1.2-1.3 becomes respectively:

$$\tau_L = \tau_{ICE} + \tau_{EM}$$

$$\omega_L = \omega_{ICE} = \omega_{EM}$$

The EM and the ICE operate at the same speed, which is imposed by the driver, while the power management system establishes how to split the torque contribution to balance the overall load requirement. The clucth C3 is normally closed during ICE and EM cooperation (hybrid mode) and also when only the ICE develops torque. C3 opens just in the case of full electric mode, when only the EM develops torque. Thus, full electric mode is an optional in this architecture and, if there are no interest in using it, C3 could be omitted.

The solution presented above has been chosen because it minimizes the transformation costs of a traditional tractor into an hybrid one, due to the minimal changes required for the mechanical structure of the vehicle. Indeed a commercial downsized Diesel engine could be selected and, in the volume made available by the reduction of the engine displacement, a proper designed EM and a clutch could be installed. In such a way, there is no need for further

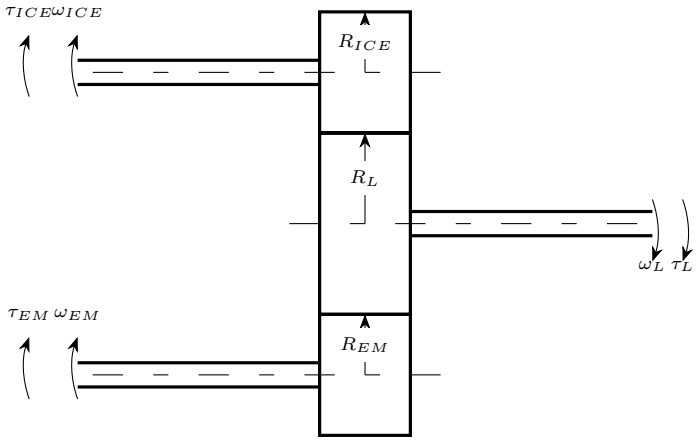

Figure 1.3: Torque adder three-gears implementation

bulky mechanical gears, that would also increase the friction losses. Besides the chassis does not require any variation. In a tractor the chassis is the most expensive piece to change as it is often manufactured by welding together cast iron bars. So any change in the chassis size and shape should be avoided during a hybridization project in order to reduce manufacturing costs. Nevertheless, this choice has some drawbacks, in particular regarding the EM design and features. Indeed the EM must be sized for high rated torque and low rated speed, resulting in a more complex design and a less efficient machine [24]. Furthermore, to fit in the volume cleared by the engine displacement's reduction, the electrical machine must have a low aspect ratio, i.e. an high stator inner diameter compared to the axial stack length, a feature that in radial flux machines highly compromises the efficiency. Besides the EM must have a great torque density so that liquid cooling systems are required. Moreover, the EM should have a low inertia and should produce low unload losses because, as explained before, it is mechanically connected to the engine even when it is not developing torque, thus it represents quite always a rotating mechanical load for the ICE.

The starter and the generator are no longer needed, as their tasks can now be performed by the EM itself. One static conversion group (CONV) drives the EM. This power electronics unit could be a unidirectional six-leg inverter if the EM behaves only as motor, or it could be a bidirectional active rectifier with a DC-DC voltage conditioning stage to allow both the charging and discharging of the battery pack (BAT L) when the electrical machine works respectively as a generator or as a motor. In the former case the battery pack could be recharged only through an external electric socket and a charging system, while in the latter case the charging is possible even when the vehicle is running.

The battery pack is a lithium-ion accumulator. Such battery type has a power density comparable to lead-acid accumulators but with a greater energy density. Indeed the battery in an electric hybrid powertrain must be designed to feed the electric motors with high current values (rms values up to $250\,[A]$) and to provide a proper energy storage to power all the other electric loads. The design of the battery pack and the power electronics unit is not a goal of this study, but some information and recommendations which could be useful to size such components will be provided during the presentation.

The hydraulic implements of the tractor are assumed to be electrified with separate electric drives. So the oil pumps are considerably powered by other electric motors through distinct static conversion groups. It has been proved that in such a way the overall efficiency of the vehicle is improved [7]. Thus only the mechanical loads, i.e. traction and PTO, are contemplated in the following analysis.

1.4 Power management system

A large variety of power management systems have been proposed in the technical literature for hybrid parallel architecture powertrains and many of them have been successfully implemented in commercial on-road vehicles. But for farming tractors the research about this topic is still at an initial stage and only few industrial solutions have been investigated [25]. Therefore, as the focus of this thesis is on the electrical machine design, the most simple power management has been chosen for the hybrid powertrain under analysis.

As the speed of both the ICE and the EM is imposed by the driver (and by the multi-gear transmission), the power management system has only the task to establish instantaneously how the torque contribution is split between the ICE and the EM to balance the mechanical loads when the vehicle operates in hybrid mode. The chosen system is based on a threshold logic. The load torque is fully provided by the ICE until a limit threshold τ_{lim} is reached. If the load torque exceeds the value of τ_{lim} the EM is activated to develop the exceeding torque. In case of negative load torque, i.e. by braking or driving downhill, the EM behaves as an electromechanical brake, namely an electric generator, and it charges the battery recovering the braking mechanical energy. The above described system workflow is mathematically represented by the following expressions:

$$\tau_{ICE} = \begin{cases} 0 & \tau_L \leq 0 \\ \tau_L & 0 < \tau_L \leq \tau_{lim} \\ \tau_{lim} & \tau_L > \tau_{lim} \end{cases} \qquad \tau_{EM} = \begin{cases} \tau_L & \tau_L \leq 0 \\ 0 & 0 < \tau_L \leq \tau_{lim} \\ \tau_L - \tau_{lim} & \tau_L > \tau_{lim} \end{cases} \tag{1.4}$$

It is important to specify that τ_{lim} is not a fixed constant, but it depends on the speed instantaneous value $\omega_{ICE} = \omega_L$. The threshold τ_{lim} is actually a torque versus speed curve obtained by a chosen downscaling of the ICE rated mechanical characteristic. This limiting curve can be calculated searching the torque-speed working points with the highest efficiency for every speed value in the range of the feasible values. Indeed in a parallel architecture powertrain the ICE cannot always operate at its maximum efficiency working point, but the power management system can exploit the highest efficiency regions for every speed value [13]. In agricultural Diesel engines the highest efficiency curve fit well the 75% of the rated mechanical characteristic, as it will be proved in the next sections of this chapter. Thus a downscaling factor of 0.75 was applied to the rated mechanical characteristic of the selected downsized ICEs for the hybrid powertrain in order to obtain the τ_{lim} threshold curve. It is relevant to underline that with such a power management logic the ICE's highest efficiency working points are not fully exploited because the engine does not always work near the τ_{lim} curve; yet in order to follow lower load torque requirements, it can operate far below the threshold curve.

Looking at the electrical machine behavior, it has been demonstrated that for agricultural duty cycles the braking energy recovering is negligible [26]. Then the electric motor works only as torque boost for the engine.

Moreover the chosen power management does not allow the battery charging through an ICE exceeding torque development. Thus the battery should have a very important capacity to feed properly the electrical systems of the vehicle during a whole working day, as it can be recharged only by an external socket. So the volume needed to place the battery pack becomes a very relevant constrain in the design of this hybrid powertrain.

The above statements will find further explanations in the next sections of this chapter with the help of graphs and charts of the chosen engines' mechanical characteristics and the processed data.

Chapter 2

Case study: open field farming tractor

The case study that concerns this thesis will be presented in this chapter.

Some available data about four different duty cycles of an open field tractor have been analyzed in detail to obtain all the needed information to carry on the hybridization process of the original powertrain, or at least to make reliable assumptions. Then the available duty cycles data have been processed with a Simulink® one-dimensional mechanical model of the vehicle to identify the torque and speed specifications of the electrical machine for three different choices of downsized engines in the hybrid powertrain. Data analysis, the vehicle circuital model and the method used to choose the electric motor torque and speed requirements are all described in detail and the related results are discussed.

2.1 Data analysis

Some preliminary measurements on an open field farming tractor working in four different conditions are available. They have been developed in the frame of the PRIN 2017 project entitled *'Green SEED: Design of more-electric tractors for a more sustainable agriculture'*. Information not yet available about the tractor powertrain and regarding the data have been supposed.

The measurements have been performed by means of specifically-implemented transducers and digital signal processor units (DSPUs). Different quantities have been measured and sampled over time during the following four operations in open field tests.

- **Plough 60**: the tractor dragged a plow on the ground to make furrows with depth of about 60 cm.
- **Plough 100**: the tractor dragged a plow on the ground to make furrows with depth of about 100 cm.
- **Power harrow**: the tractor drove a power harrow through its power take off (PTO) shaft and pulled it in the field.
- **Transportation**: the tractor carried an unknown load in the field.

The available data for each test are here reported and analyzed. Relevant details about some of them deserve a significant attention related to the next data elaboration in order to find out the right inputs for the mechanical circuit model of the powertrain.

2.1.1 Plowing tests measurements

For the two plowing tests the following measures are available:

- **engine torque** [$\boldsymbol{Nm}$]; torque developed by the ICE measured at engine shaft;
- **engine speed** [$\boldsymbol{rpm}$]; engine shaft rotational speed;
- **vehicle speed** [$\boldsymbol{km/h}$]; tractor linear velocity.

The **plowing draft** [$\boldsymbol{N}$]was measured too, probably with a system made up by a force transducer installed on the plough implement used for this specific purpose. The measured force is the component of the ground resistance acting on the plow parallel to the tractor motion.

Engine parameters (torque and rotational speed at the shaft) have been sampled with the same frequency, as the same number of samples are available for both quantities. The vehicle speed and the draft force have been sampled with different time steps compared to the one used for the engine torque and the engine speed, maybe because the vehicle speed was sampled by the internal ECU of the tractor, while the draft force was sampled by a different DSPU than the one used to process the engine quantities. As available data result from fewer vehicle speed samples and more draft samples, it is feasible that the vehicle speed was sampled with a bigger time step while the draft force was sampled by a smaller one compared to engine torque and engine speed data.

Time samples are given in the same number of engine quantities samples, so vehicle speed and draft force data are referred to engine measurements time step through a linear interpolation in order to make comparable plots of all data. Therefore the time reference of the plots is based on the given time samples.

All the available data about the two plowing tests are plotted in Figure 2.1-2.2. The instantaneous power developed by the engine during the tests $p_{_{ICE}}$ has been computed as the product of the measured torque $\tau_{_{ICE}}[Nm]$ by the instantaneous engine shaft speed converted to $[rad/s]$ $\omega_{ICE}[rad/s]$:

$$p_{_{ICE}} = \tau_{_{ICE}} \cdot \omega_{_{ICE}} \tag{2.1}$$

2.1.2 Power harrow test measurements

At this working stage both traction and PTO have been involved.

- **engine torque** [$\boldsymbol{Nm}$]; torque developed by ICE measured at engine shaft;
- **engine speed** [$\boldsymbol{rpm}$]; engine shaft rotational speed;
- **PTO torque** [$\boldsymbol{Nm}$]; torque measured at PTO shaft;
- **PTO speed** [$\boldsymbol{rpm}$]; PTO shaft rotational speed;
- **vehicle speed** [$\boldsymbol{km/h}$]; tractor linear velocity.

Engine's quantities (torque and rotational speed at the shaft) and PTO quantities have been sampled with the same frequency, as the same number of samples are available for these four data sets. Instead the vehicle's speed has been sampled with a smaller frequency (i.e. a bigger time step), probably because it was processed by the internal ECU, while for the other measurements an external DSPU has been used. Time samples are not given for this test, thus their overall number is assumed equal to the one of the engine and PTO quantities and the same time step from the plowing tests is supposed. Therefore the vehicle's speed samples are referred to the time step using a linear interpolation.

All the available data are plotted in Figure 2.3. The instantaneous power developed by the engine is computed as in Equation 2.1 while the instantaneous power required by the PTO $p_{_{PTO}}$ is calculated as:

$$p_{_{PTO}} = \tau_{_{PTO}} \cdot \omega_{_{PTO}}$$

Where $\tau_{_{PTO}}$ $[Nm]$ is the instantaneous torque required at the PTO shaft and $\omega_{_{PTO}}$ is the instantaneous PTO shaft speed in $[rad/s]$.

Looking at Figure 2.3, it is very important to notice that engine shaft and PTO shaft have different rotational speeds. PTO shaft speed is about half of the engine shaft speed. This

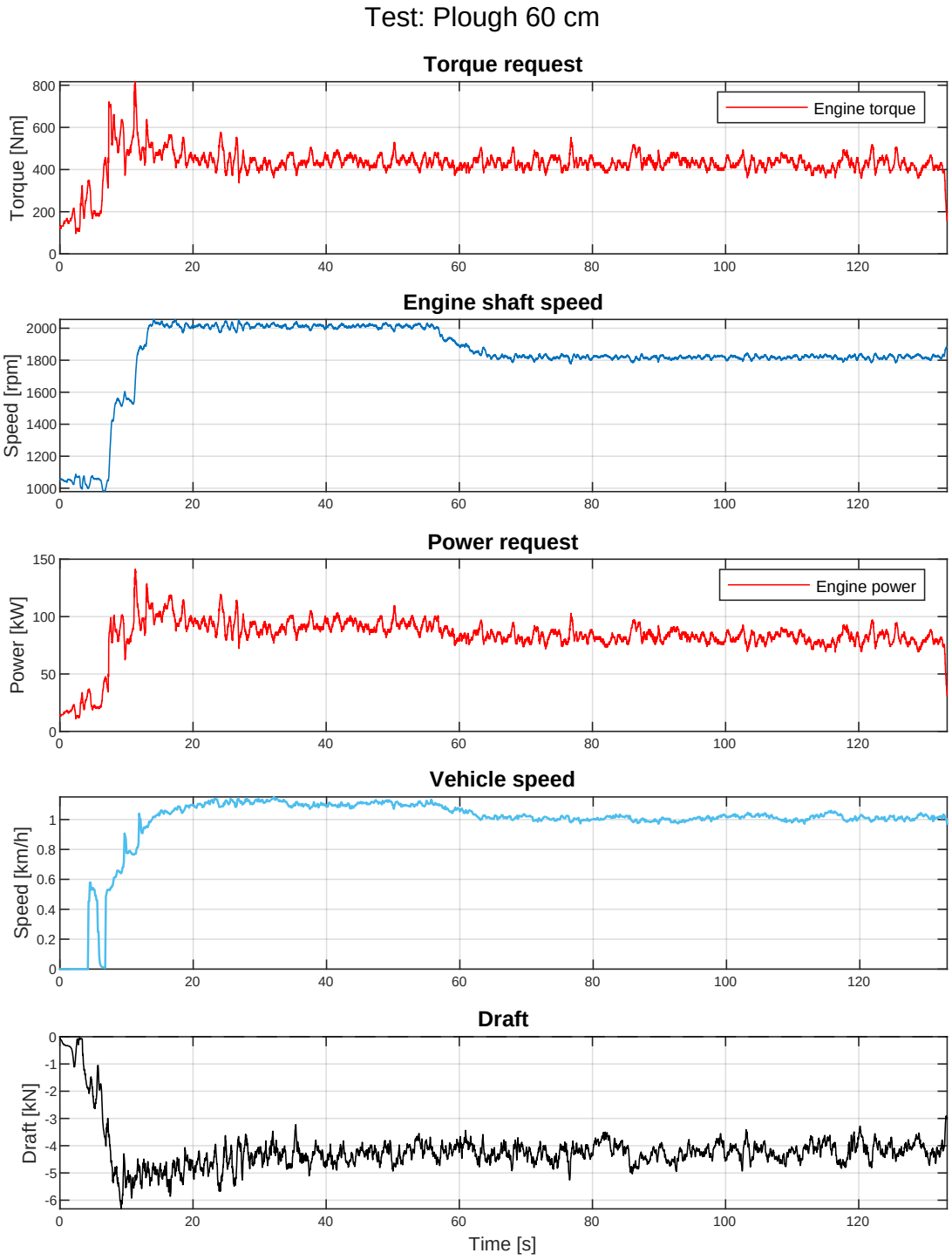

Figure 2.1: Available data from plough 60 test.

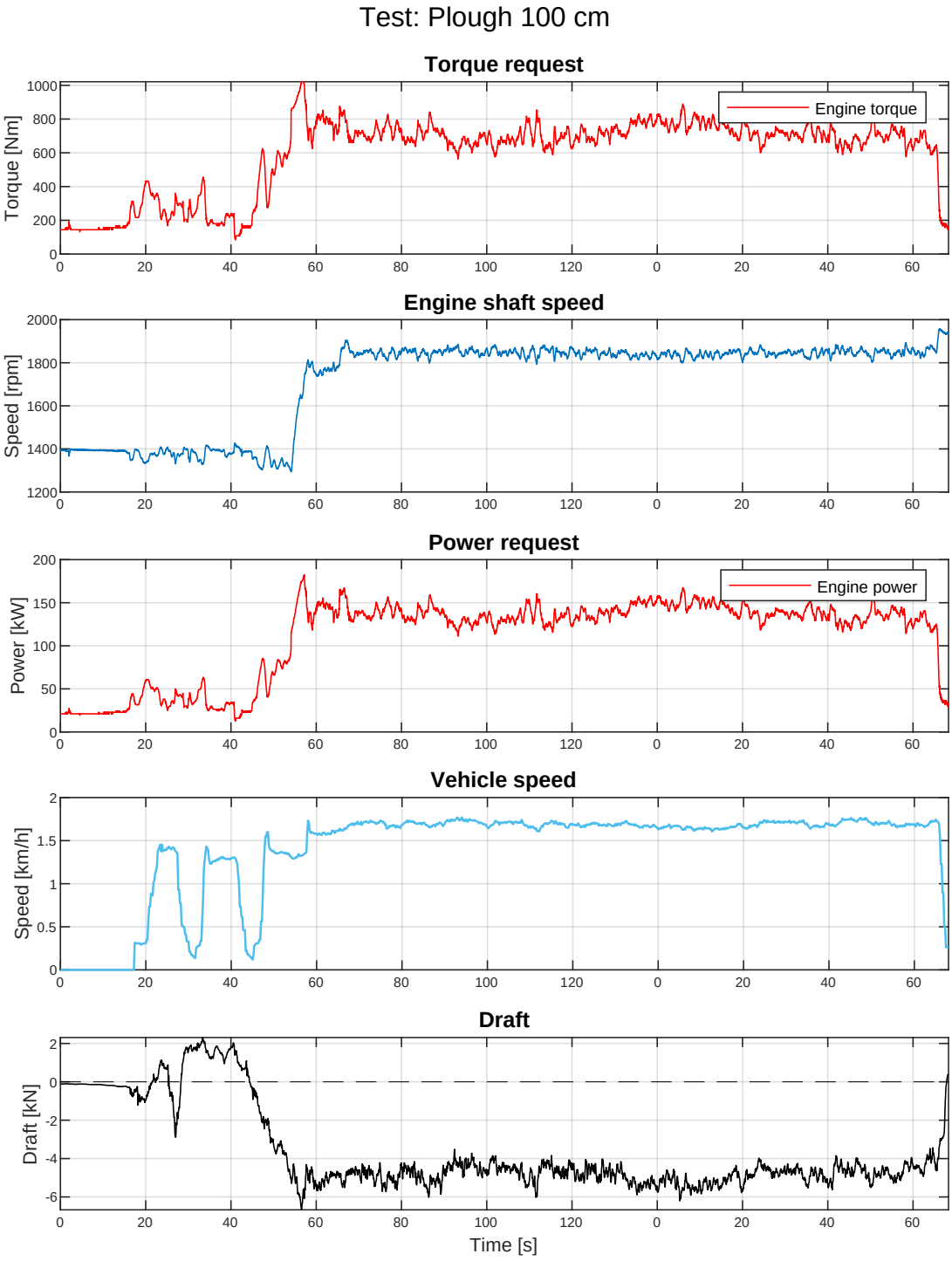

Figure 2.2: Available data from plough 100 test.

means that during the test the engine shaft and the PTO shaft have been connected through a **speed reducer with a fixed gear ratio**, as previously outlined in Figure 1.1. This fixed gear ratio G can be estimated as the ratio between the mean over time of the engine shaft speed $\bar{\Omega}_{ICE}[rad/s]$ and the mean over time of the PTO shaft speed $\bar{\Omega}_{PTO}[rad/s]$:

$$G = \frac{\bar{\Omega}_{ENG}}{\bar{\Omega}_{PTO}} \cong 1.89 \tag{2.2}$$

Where $\bar{\Omega}_{ICE}$ and $\bar{\Omega}_{PTO}$ are evaluated in discrete form as the sum of the samples values Ω_k divided by the number of the considered samples, instead of the continuous integral average over time:

$$\bar{\Omega}_{ICE} = \frac{\int_{t_0}^{t_1} \omega_{ICE} dt}{t_1 - t_0} \cong \frac{\sum_{k=n_0}^{n_1} \Omega_{ICE_k}}{n_1 - n_0}$$

$$\bar{\Omega}_{PTO} = \frac{\int_{t_0}^{t_1} \omega_{PTO} dt}{t_1 - t_0} \cong \frac{\sum_{k=n_0}^{n_1} \Omega_{PTO_k}}{n_1 - n_0}$$

In the computation of the mean values only halfway samples are considered, i.e. from n_0 at time t_0 to n_1 at time t_1, in order to select a time interval which in the speed trend does not change too much.

The identification of this gear ratio G is very relevant to the next data processing: later it will be used to find out the right inputs for the circuital simulator of the hybrid powertrain outlined in Figure 1.2.

2.1.3 Transportation test measurements

All the available measures for this test have been taken from the same DSPU. They are the following:

- **engine torque** $[\boldsymbol{Nm}]$; torque developed by ICE measured at engine shaft;
- **engine speed** $[\boldsymbol{rpm}]$; engine shaft rotational speed;
- **vehicle speed** $[\boldsymbol{km/h}]$; tractor linear velocity.

All the three quantities have been sampled with the same frequency and the reference time samples are given. All the available data are plotted in Figure 2.4. The instantaneous power developed by the engine is computed as in Equation 2.1.

2.2 Mechanical circuit model and data pre-processing

Since the goal of a hybridization process is to identify the speed and torque requirements for the electrical machine design, a mechanical equivalent circuital model of the hybrid powertrain outlined in Figure 1.2 was developed in Simulink® SimScape® to achieve this purpose[10]. The mechanical circuit implemented in the simulator is shown in Figure 2.5.

The engine is represented as a torque generator which imposes a torque value on the shaft that corresponds to the maximum one available at a given rotational speed, according to the mechanical characteristic of the chosen engine. Thus the ICE can be seen as a speed-regulated torque generator. The engine rotational speed and its rated mechanical characteristic are the first inputs for the model. The torque developed by the ICE can be decreased proportionally with a reduction factor R ($0 \leq R \leq 1$). This operation consists of a downscale of the mechanical characteristic of the chosen engine and it was implemented for two purposes: first of all, setting the reduction coefficient R is an easy method to pass a torque threshold curve τ_{lim} to the power management system; secondly, R could be used to simulate a large range of increasing hybridization grade, from the traditional powertrain ($R = 1$, $H = 0\%$) to a full electric one ($R = 0$, $H = 100\%$), without using the rated mechanical characteristics of the downsized ICEs. This topic will be deeply discussed in the next sections.

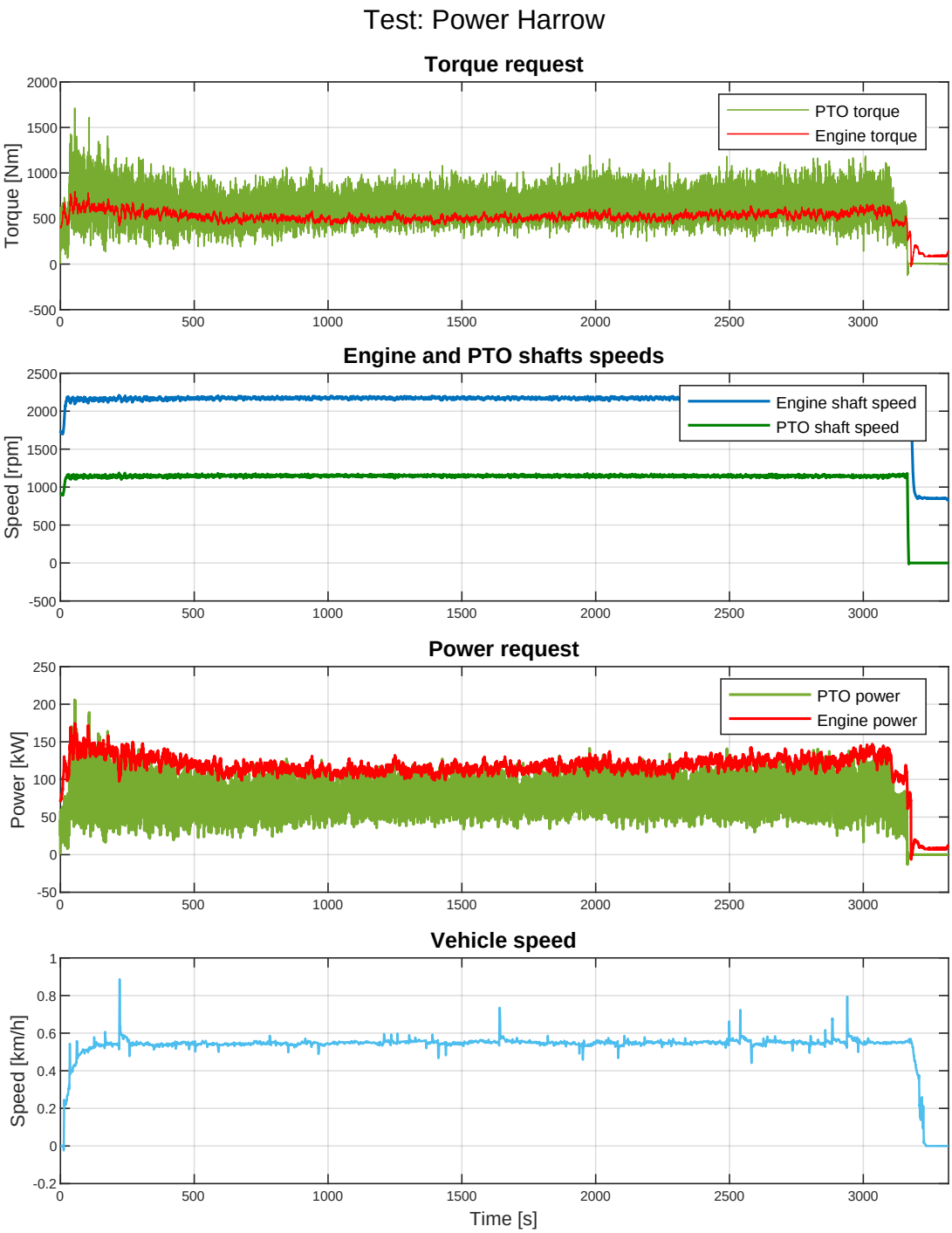

Figure 2.3: Available data from power harrow test.

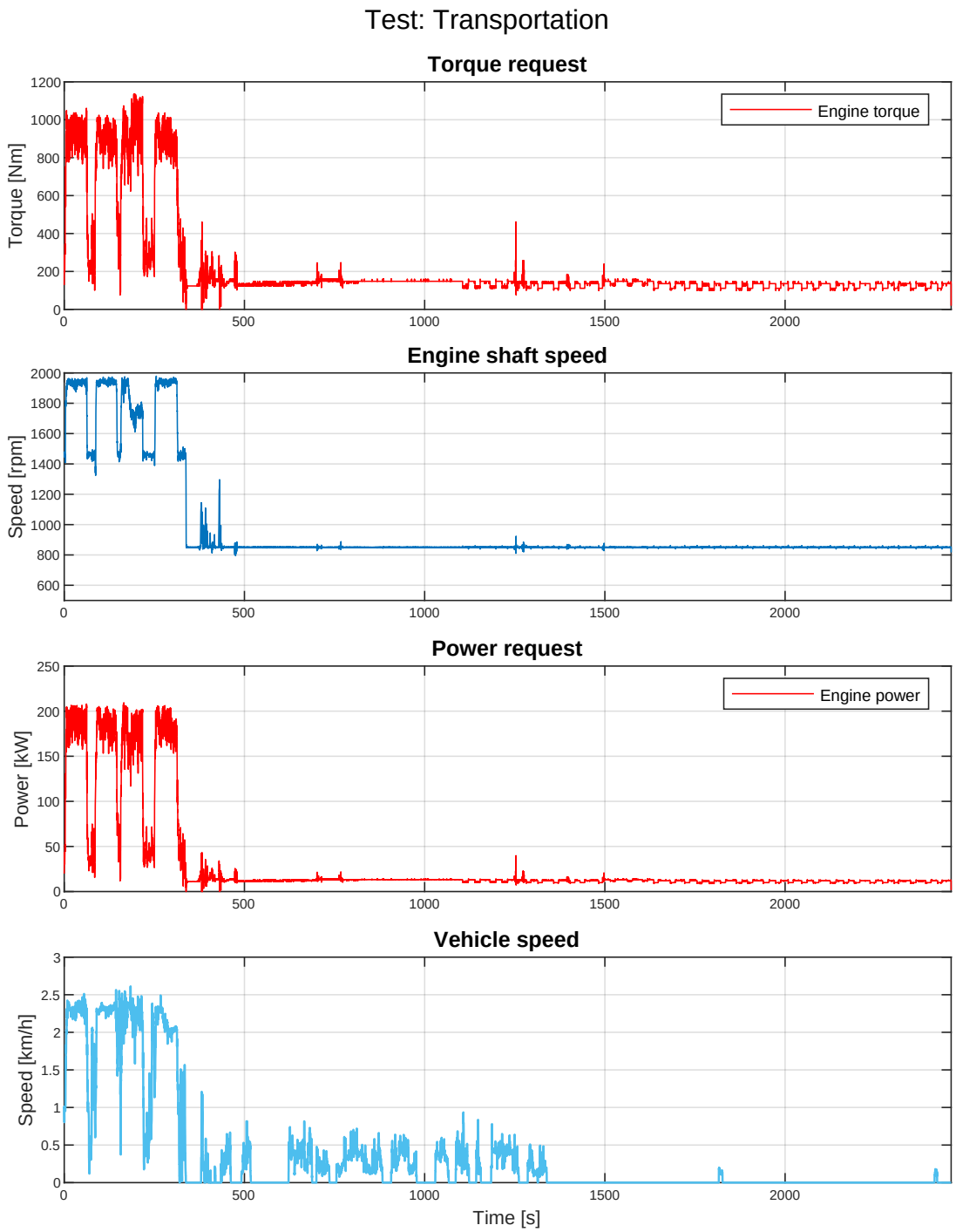

Figure 2.4: Available data from transportation test.

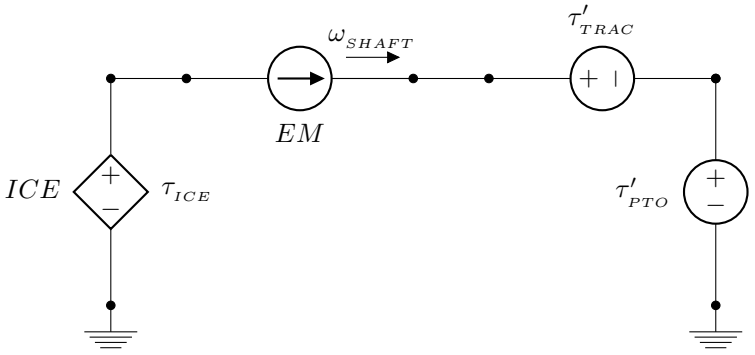

Figure 2.5: Mechanical circuital model.

The load torque, i.e. traction and PTO, is also represented with torque sources, but they are not regulated by the rotational speed. Indeed they impose on the engine shaft a given torque regardless of the rotational speed of the shaft. So the traction torque τ'_{TRAC} and the PTO torque τ'_{PTO} are inputs for the circuital model. It is important to underline that these inputs must be referred to the engine shaft. In such a circuit all the quantities are referred to the engine shaft. In this way the auxiliaries energy consumption as well as the friction losses in the multi-gear transmission system are included in the model without the need of specific data about this power contributions. The available data do not report the traction torque, and the PTO torque is not referred to the engine shaft in power harrow test. So for each test the traction torque used in the simulations is computed with the following torque balance, where any friction in the shaft bearings and in the speed reducer is neglected:

$$\tau'_{TRAC} = \tau_{ICE} - \frac{\tau_{PTO}}{G}$$

The PTO torque referred to the engine shaft is obtained as:

$$\tau'_{PTO} = \frac{\tau_{PTO}}{G}$$

Where G is the gear ratio of the speed reducer computed in Equation 2.2. From the previous equations it can be seen that the traction torque requested at the engine shaft τ'_{TRAC} is equal to the engine torque τ_{ENG}, except for the power harrow test, where the PTO is involved too.

The EM is simulated with a speed generator which imposes the engine speed ω_{SHAFT} on the shaft. The ICE and the EM are installed on the same single shaft (except for the clutch C3) so they are bounded to the same rotational speed. All the components in the circuit have the same rotational speed ω_{SHAFT}, which is an input for the model, so the speed requirements for the EM are automatically dictated by the duty cycles of the tractor.

The instantaneous torque on the EM is the only unknown in the circuit: it is computed by the simulator starting from the following mechanical power balance on the shaft:

$$p_{ICE} + p_{EM} + p_{TRAC} + p_{PTO} = 0$$

A mechanical power is calculated as the product of torque by rotational speed. So the power balance can be rewritten as:

$$\tau_{ICE} \cdot \omega_{ICE} + \tau_{EM} \cdot \omega_{EM} + \tau'_{TRAC} \cdot \omega'_{TRAC} + \tau'_{PTO} \cdot \omega'_{PTO} = 0$$

Since all the rotational speed are equal as all the quantities are referred to the engine shaft, the previous equation becomes:

$$\tau_{ICE} + \tau_{EM} + \tau'_{TRAC} + \tau'_{PTO} = 0$$

And finally the EM torque is expressed as:

$$\tau_{EM} = -\tau_{ICE} - \tau'_{TRAC} - \tau'_{PTO}$$

The load torques referred to the engine shaft τ'_{TRAC} and τ'_{PTO} are processed by the simulator as negative quantities while the ICE torque τ_{ICE} is processed as a positive quantity. Under these statements a torque balance equivalent to the previous one can be obtained with the application of Kirchhoff law at the only mesh in the circuit of Figure 2.5. Hence the Kirchhoff *'torque'* law returns:

$$\tau_{EM} = \tau'_{TRAC} + \tau'_{PTO} - \tau_{ICE}$$

Where both the load torque and the engine torque in this case are considered as positive quantities.

The resulting EM torque is positive when the EM works as motor to boost the ICE and it is negative when the engine torque is greater than the load torque, hence the EM behaves as an additional load developing a braking torque and possibly working as an electric generator. The latter case is not take into account in this study due to the chosen power management system, whose logic, represented by Equation 1.4, does not allow the battery charging through an exceeding engine power production. Thus only the positive torque values of the EM will be considered to find out a sizing torque specification.

2.3 Data post-processing: thermal equivalent torque

The EM boosting torque signals have been post-processed according to the equivalent thermal torque method in order to obtain the needed information that can be used to choose the torque specifications for the electric motor design. This method is commonly used to size electrical machines that have to withstand high changing duty cycles, for example it is applied to identify the torque requirements of traction motors for electric vehicles. The base concept is to design the EM not on the maximum torque value reached in the duty cycle, but to choose a smaller rated performance and fulfill the peak values exploiting a proper overload capability. Indeed it is not convenient to size the machine on the maximum torque because in a rapidly changing duty cycle the peak values are reached only for small time intervals, if compared to the total duration. So an electric motor designed in such a way will result greatly oversized and it will not be suitable for applications where a small displacement is required, as the one that concerns this project. Instead a machine sized on a smaller rated torque will be more worthwhile in terms of volume and weight reduction.

The selected rated torque must be a halfway value that allows the EM to withstand the peaks during the entire duty cycle avoiding excessive in-slot overtemperatures ϑ that can damage the insulator materials. Moreover for permanent magnets motors a particular care must be taken for the magnets overtemperatures too. To identify such a rated specification the equivalent thermal torque can be computed. The computation is performed using a low pass filter applied on the EM boosting torque signals, in order to approximate the average integral in the root-mean-square definition of the thermal equivalent torque, as reported in [10, 15], so the thermal dynamics of the machine must be supposed. Indeed the equivalent thermal torque can be defined as the torque trend that produces the same total Joule losses $P_{J_{tot}}$ of the actual duty cycle. The thermal behavior of an electric motor can be summarized by the simplified RC equivalent thermal circuit shown in Figure 2.6, characterized by its thermal time constant τ_{th} $[s]$:

$$\tau_{th} = R_{th_{eq}} C_{th_{eq}} \tag{2.3}$$

$R_{th_{eq}}$ $[^\circ K/W]$ and $C_{th_{eq}}$ $[J/^\circ K]$ are respectively the thermal equivalent resistance and the thermal equivalent capacity of the machine. They depend upon the thermal properties of the material used to manufacture the machine and its volume and weight.

τ_{th} is the time constant of the low pass filter used to process the EM boosting torque. Therefore some feasible values of τ_{th} must be supposed. The electrical machine type chosen for this project is a radial flux liquid cooled surface permanent magnets (SPM) motor. For such a

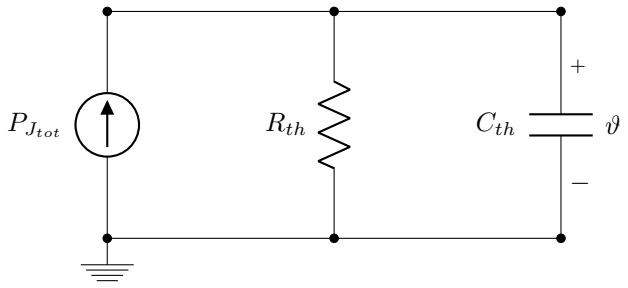

Figure 2.6: Simplified equivalent thermal circuit of an EM.

kind of machines the thermal time constant τ_{th} spans in the range $200 \div 1000\,[s]$, regarding to rated torque specifications in the range $100 \div 400\,[Nm]$. A detailed mathematical explanation of the equivalent thermal torque is reported by D. Troncon *et al.* in [15].

Choosing a suitable time constant is a thorny point, as the selected value should be verified at the end of the machine design through a sufficiently detailed transient thermal analysis. The choice is not trivial. With the same duty cycle, low values of τ_{th} lead to the choice of higher rated specifications and lower overload capabilities, while high values of τ_{th} lead to lower rated torque requirements and higher overload capabilities. But the thermal dynamic behavior of an EM depends strongly on its thermal equivalent capacity, as expressed in Equation 2.3, rather than on its equivalent thermal resistance, that should be minimized to limit the steady state overtemperature. High values of C_{th} imply high weights. On the contrary, low τ_{th} are typical of smaller machine with a lower rated torque, while high τ_{th} are characteristic of bigger machines with higher rated specifications.

The above statements will be clarified in the next sections, when the hybridization tests' results will be presented and the torque specifications for the EM design will be definitively chosen. Further explanations on the thermal behavior of electric motors will be provided in Chapter 5.

2.4 Engines selection

Since the model described in Section 2.2 requires at least one engine mechanical characteristic, the ICE mounted on the original powertrain must be feasibly supposed from the available duty cycles data .

Looking at the power and torque trends in all four working conditions reported in Figures 2.1-2.2-2.3-2.4 it can be observed that the transportation duty cycle is the most critical one, when the engine worked at the top of its performance during the first starting and acceleration phase. From Figure2.4 it could be deduced that the original ICE should be able to supply a mechanical power a bit greater than $200\,[kW]$ and a torque of about $1100\,[Nm]$ at a speed a bit lower than $2000\,[rpm]$. Moreover, always looking at Figure 2.4, after the first acceleration it could be noticed that the tractor stopped for a long time, i.e. $2000\,[s] \cong 33\,[min]$. During this period the engine was kept on and it was working at idle speed, which is lower than $800\,[rpm]$, providing the torque only to power the auxiliaries, since no traction nor PTO torque was required. The original ICE worked at its maximum speed during the power harrow operation. Looking at Figure 2.3 the deduced maximum speed lies in the range $2200 \div 2300\,[rpm]$.

Therefore different agricultural Diesel engines, whose declared technical specifications are close to the values identified above, have been selected from commercial datasheets provided by different companies [27, 28, 29, 30]. All the engines are manufactured under the Stage III EU standard or under the corresponding Tier III US regulation. Their mechanical characteristics (rated torque and rated power curves) are plotted together with the experimental points in all four working conditions to see which one fits the working points better. The overload capability of turbocharged Diesel engines has not been considered, so that the rated mechanical characteristic corresponds to the maximum torque and maximum power versus speed curves. These curves have been obtained by inspection from the datasheets of the selected engines.

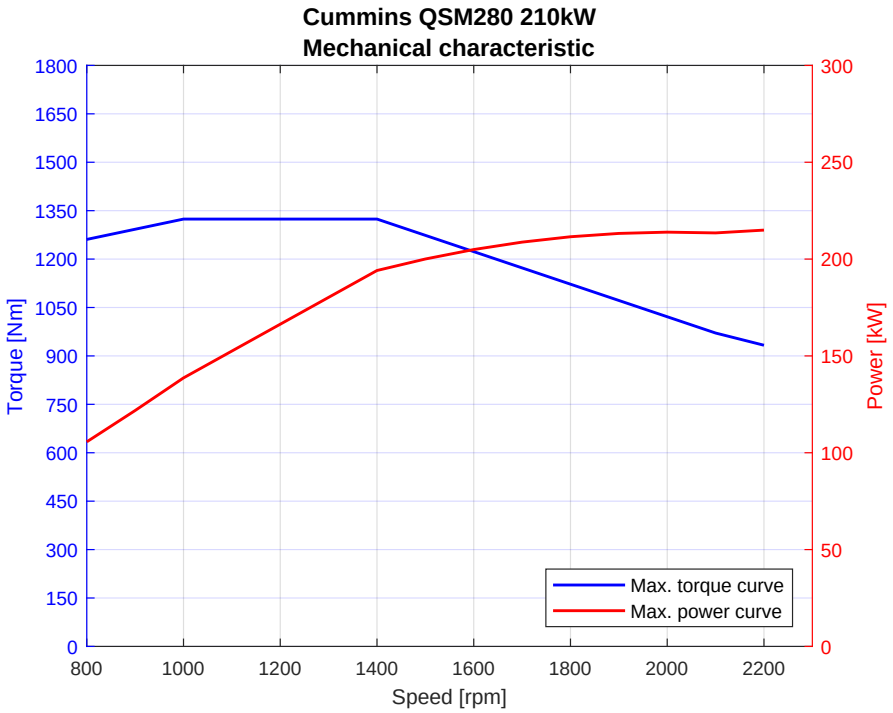

Figure 2.7: Original ICE mechanical characteristic.

Instead the experimental points, since they are the working points of the original ICE during the four different operations, have been extrapolated from the available duty cycles data (see Section 2.1) through some plots of engine torque versus speed. The different mechanical characteristics have been compared with the experimental points in order to determine a feasible original ICE. All the experimental points in each working condition must be possible working points for the engine, so they must be under the curves. Furthermore, there is no benefit in choosing an extremely powerful engine because it will not be useful to the later downsizing in the hybridization process and it is not feasible that the original engine were too much oversized.

Hence, under such considerations, the selected ICE that fits better the experimental points is the Cummins QSM280 [27], a turbocharged in-line six-cylinder Diesel engine with a declared rated power of 210 $[kW]$ (280 $[Hp]$), whose mechanical characteristic is reported in Figure 2.7. Figure 2.8 shows the comparison between the candidate ICEs mechanical characteristics and the working points during the transportation test, which is the most critical duty cycle in terms of torque and power requirements and indeed it is the test that allowed the selection of the original ICE.

Once a feasible original engine has been chosen, three downsized ICEs with a decreasing rated power have been selected for the hybrid powertrain to perform the hybridization tests. The downsized ICEs are all made by FPT Industrial under Stage IV European standard (Tier IV US regulation) [30]. The goal is to achieve Stage V emission requirements without selective catalytic reducer (SCR) and Diesel particulate filters (DPF), thanks to the lower fuel consumption of the electric hybrid powertrain. A different manufacturer was chosen than the one which supply the supposed original ICE, i.e. Cummins, but for simplicity all downsized engines belong to the same series, namely FPT N67ENT.

2.5 Hybridization tests

Two hybridization processes have been carried out. The first one is performed through a progressive downscaling of the supposed original ICE mechanical characteristic (Cummins QSM280 210 $[kW]$) by decreasing gradually the reduction coefficient R (see Section 2.2). Simulations

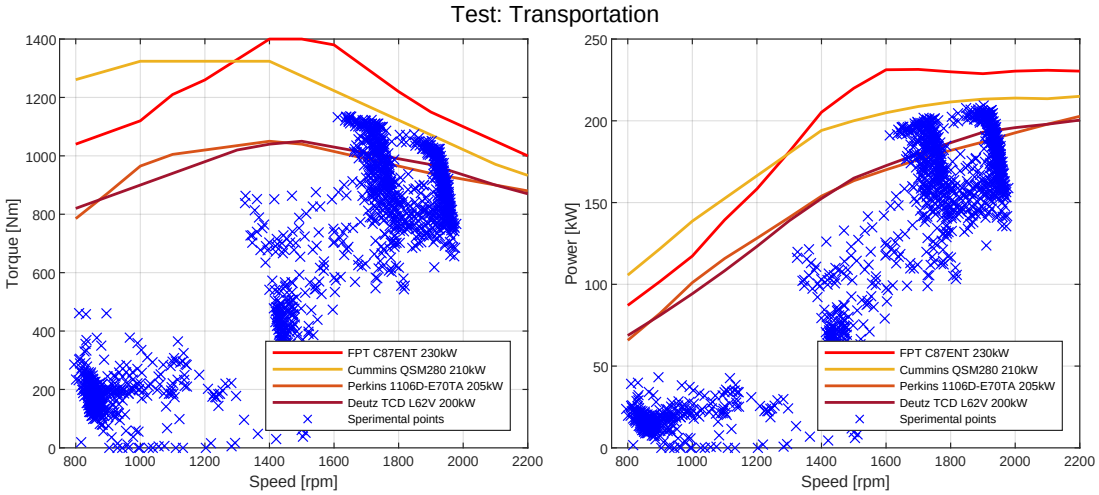

Figure 2.8: Original ICE research. Comparison against experimental points in transportation working condition.

have been done with the following values of R.

- $\boldsymbol{R = 1}$: ICE develops the maximum torque available at any rotational speed; the engine works on the original mechanical characteristic; the hybridization grade is $\boldsymbol{H = 0\,\%}$ and the model represents the traditional vehicle powertrain.
- $\boldsymbol{R = 0.75}$: ICE develops the **75 %** of the maximum torque available at any rotational speed; the engine works on a mechanical characteristic reduced by **25 %** .
- $\boldsymbol{R = 0.50}$: ICE develops the **50 %** of the maximum torque available at any rotational speed; the engine works at half of its maximum performances.
- $\boldsymbol{R = 0.25}$: ICE develops the **25 %** of the maximum torque available at any rotational speed; the engine works on a mechanical characteristic reduced by **75 %**.
- $\boldsymbol{R = 0.00}$: ICE does not develop torque at any rotational speed; the hybridization grade is $\boldsymbol{H = 100\,\%}$ and the vehicle works in pure electric mode; the required power is entirely given by the EM.

Differently, the second hybridization process has been performed using the mechanical characteristics of the three downsized ICEs previously selected. The mechanical characteristics of the three different engines have been obtained by inspecting their commercial datasheets [30]. It is relevant to highlight that the simulations with the downsized ICEs have been done by setting the engines at the 75% of their maximum torque and power performances, i.e. with $R = 0.75$, in order to simulate a threshold curve τ_{lim} that permits to exploit highest efficiency regions. The above statement has been proved by comparison of the actual highest efficiency curve with the mechanical characteristic of a selected engine reduced by 25%. The results are summarized in Figure 2.9, where it can be seen that the curve with $R = 0.75$ stays almost always above the real highest efficiency curve. The curves are plotted over the BSFC map (Brake Specific Fuel Consumption) of the engine FPT N67ENT 175 $[kW]$, one among the three downsized ICEs. The efficiency map has been computed with an interpolating function that fits the parameters of a large variety of agricultural Diesel engines. Its values are reported in terms of specific fuel consumption $[g/kWh]$, thus the actual highest efficiency curve has been computed by searching the working point with the minimum BSFC for every speed value.

The two hybridization processes are represented and compared in Figure 2.10. The graphs show that there is not a great distance in terms of mechanical characteristics between the downsized ICEs and the corresponding torque and power reductions of the original engine through the R coefficient, even if the original ICE and the downsized ones are made by different

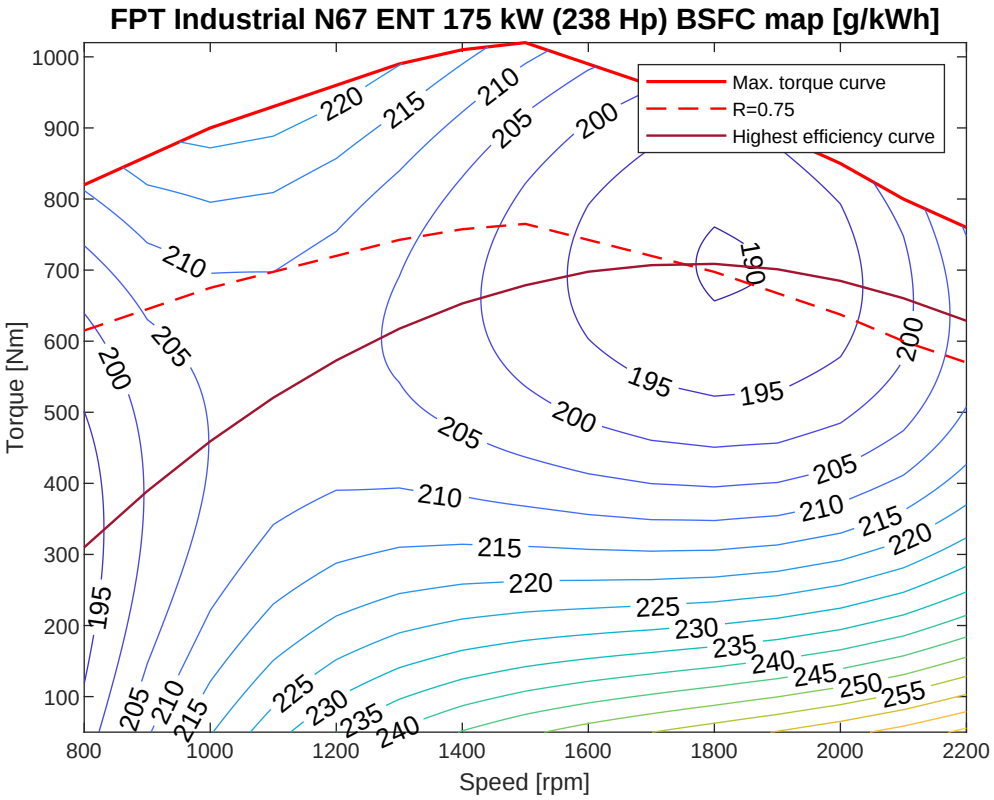

Figure 2.9: Comparison between the threshold curve with $R = 0.75$ and the actual highest efficiency curve over the BSFC map of the engine FPT N67ENT 175 $[kW]$

manufacturers. As an example, always looking at Figure 2.10, it can be seen that the curve obtained with the mechanical characteristic of the FPT N67ENT 175 $[kW]$ fits sufficiently the threshold curve obtained after the reduction of the mechanical characteristic of the original Cummins QSM280 210 $[kW]$ with $R = 175/210 \cong 0.83$. Indeed the resulting EM boosting torque profiles obtained from the hybridization tests performed using the reduction coefficients R indicated in Figure 2.10 and multiplied by 0.75 are very similar to the results achieved with the downsized ICEs mechanical characteristics limited with $R = 0.75$. For brevity purpose, only the latter findings will be reported in the next section.

Such outcome proves that only the original ICE parameters and the rated torque of the downsized engine need to be known in order to carry out an effective preliminary hybridization process for any powertrain with an equivalent circuital model referred to the engine shaft. Furthermore, a sweep among the values of the R coefficient could be used to perform optimization analysis on the hybrid powertrain in order to establish which ones could be the most advantageous hybridization degrees.

2.6 Hybridization results

For brevity purpose, only the outcomes achieved using the downsized ICEs characteristics limited at the 75% are here reported and, among them, only the results that are relevant to identify a rated torque specification for the electrical machine design are presented. Figures 2.11-2.12-2.13 show the EM boosting torque profiles filtered with time constants τ in the range $200 \div 1000$ $[s]$ for each downsized ICE during the transportation duty cycle, which is the most critical one.

As expected, the torque requirements to the electric motor increase with the decrease of the engine rated power, i.e. with the increase of the hybridization factor. Besides, in the same duty

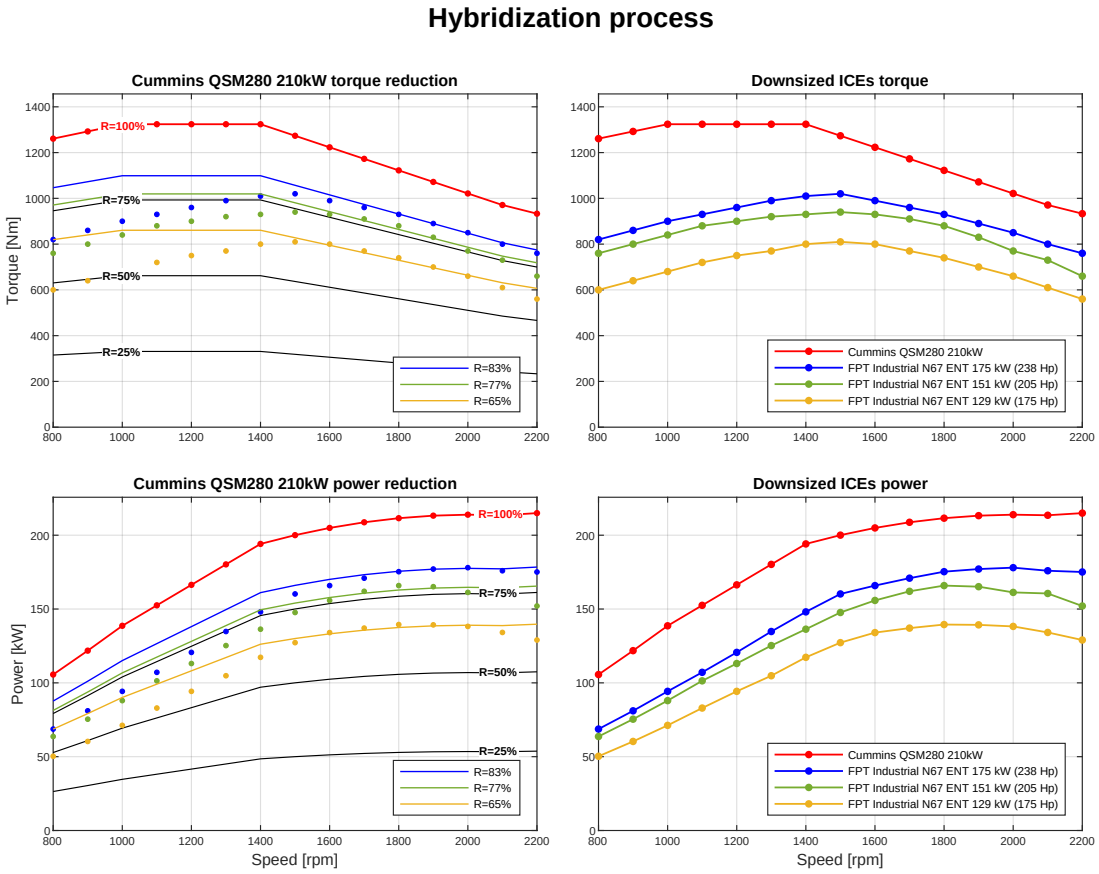

Figure 2.10: Hybridization processes comparison.

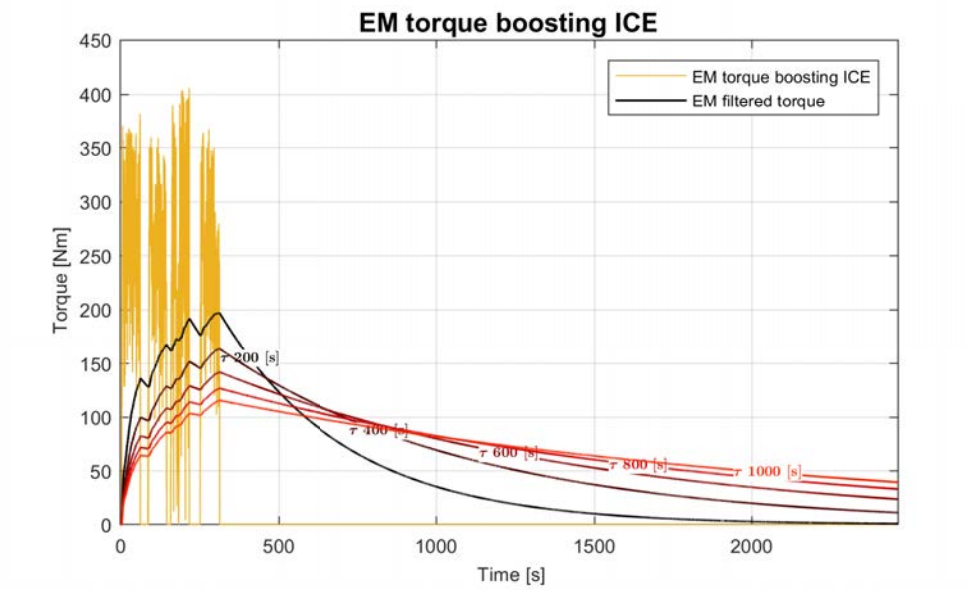

Figure 2.11: Powertrain with FPT N67ENT 175 $[kW]$ at 75% of max. performance. EM filtered boosting torque during transportation duty cycle.

cycle with the same downsized ICE, the equivalent thermal torque has lower peak values for higher thermal time constants τ, as previously disclosed in Section 2.3. Indeed machines with higher τ heat up much slower when an overload current flows in the winding. But high values of τ demand high overload capabilities to fulfill the peak torque requests.

Referring to Figures 2.11-2.12-2.13 the torque requirements to size the electric motor has been chosen for each hybridization test. To do so the thermal time constant τ has been supposed in the range $800 \div 1000$ $[s]$. Synchronous SPM machines have been chosen for this project, thus the rated speed has been set to the maximum value $n_R = 2300$ $[rpm]$ demanded in the power harrow duty cycle. Thanks to this choice the EM should be controlled always in the MTPA working region (Maximum Torque Per Ampere), so that the driving conversion group components could be sized for lower current values and also the battery should withstand lower discharging current [31]. Moreover, SPM machines have a very limited flux-weakened working region, therefore there are few advantages in exploiting it. These concepts will be further presented in the next chapter.

Once a rated torque $\mathcal{T}_R$ $[Nm]$ and a rated speed n_R $[rpm]$ have been chosen, the rated power $P_{EM} = P_R$ $[W]$ has been computed for every EM as follows:

$$P_R = \mathcal{T}_R \cdot n_R \cdot \frac{2\pi}{60}$$

Consequently, the actual hybridization factor H has been obtained as expressed in Equation 1.1 and each hybrid powertrain has been classified according to Table 1.1. Besides the overload torque capability $\mathcal{T}_{OL}$ has been selected to make sure that the motor can fulfill the peak torque requests. The chosen specifications are summarized in Table 2.1. It is relevant to point out that such values are not mandatory. They are only needed to size the electric motor but they could be changed or not fully observed during the machine design and analysis, providing that in the end the motor is able to withstand all the duty cycles with sufficient performances.

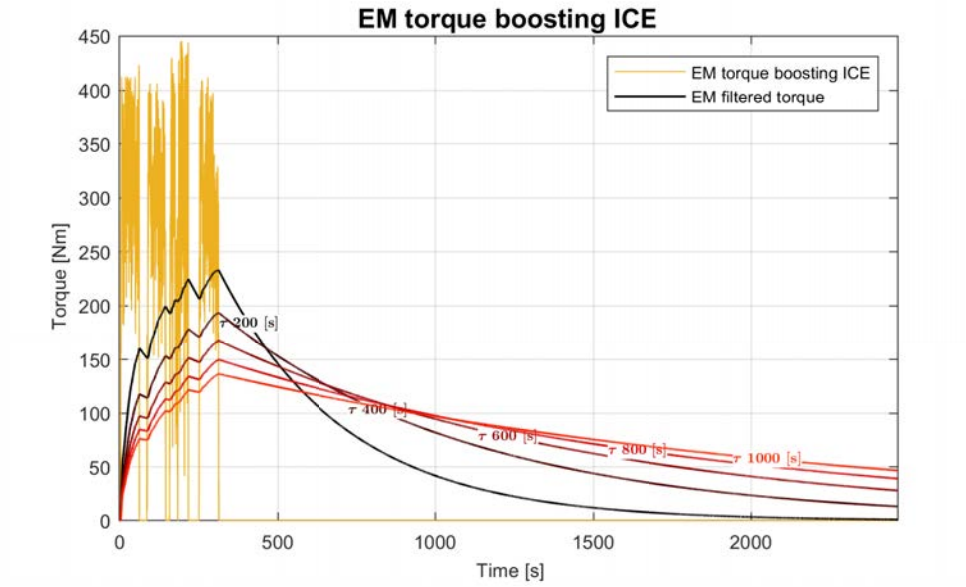

Figure 2.12: Powertrain with FPT N67ENT 151$[kW]$ at 75% of max. performance. EM filtered boosting torque during transportation duty cycle.

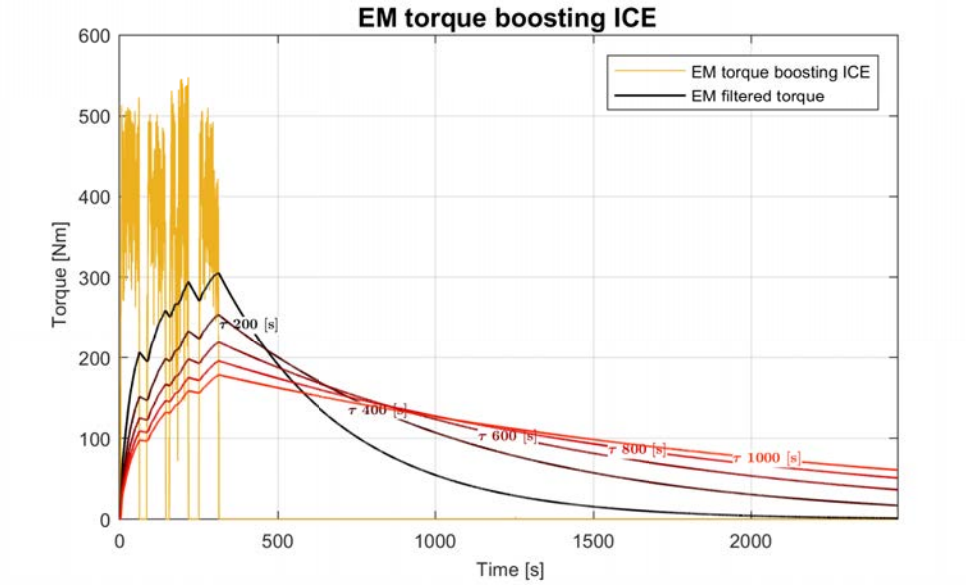

Figure 2.13: Powertrain with FPT N67ENT 129$[kW]$ at 75% of max. performance. EM filtered boosting torque during transportation duty cycle.

Downsized ICE Equivalent R	FPT 175 $[kW]$ $0.83 \cdot 0.75$	FPT 151 $[kW]$ $0.77 \cdot 0.75$	FPT 129 $[kW]$ $0.65 \cdot 0.75$
$\mathcal{T}_R\ [Nm]$	120	140	180
$n_R\ [rpm]$	2300	2300	2300
$P_R\ [kW]$	29	34	43
H [%]	14	18	25
Type	Mild-hybrid	Mild-hybrid	Full-hybrid
$\mathcal{T}_{OL}\ [Nm]$	$4 \times \mathcal{T}_R$	$3.5 \times \mathcal{T}_R$	$3.5 \times \mathcal{T}_R$

Table 2.1: EM rated and overload specifications for each hybrid powertrain.

Chapter 3

Electrical machines sizing

The electromagnetic sizing of a liquid cooled radial-flux SPM motor is presented in this chapter.

At the beginning, a description of the significant features of this type of machine and its control system are provided, so that advantages and drawbacks are standing out. Other types of EM that could be implemented in this application will be mentioned in order to give explanations about the choice made for this project.

Three different SPM motors have been designed for one of the three hybrid powertrain under analysis. The EMs differ mainly in the number of poles. The EMs sizing has been performed starting from the performance specifications previously identified and under some realistic volume limits. The limited displacement available for the EM has been a very challenging constrain and a particular sizing method have been implemented to cope with it. All the design choices as well as the method used to find out the main sizes of the machines will be described in detail.

At the end, a material cost estimation and comparison are reported.

3.1 Machine description

The chosen type of electric motor is illustrated in Figure 3.1. It is an inner rotor radial-flux surface permanent magnet (SPM) machine. Such kind of motor is defined as a synchronous machine because its mechanical rotating speed is proportional, namely synchronized, to the electrical frequency of the three-phase alternating current which flows in the armature winding and it is independent of the current amplitude, i.e. of its electrical load [24]. This type of machine has been chosen for its high power density and easy manufacturing process. If compared to an induction motor (IM) with equal rated power, a SPM motor results to be much more compact. Moreover, despite SPM machines are usually more suitable for high speed applications than high torque ones, they have even a higher torque density than IMs, i.e. with equal rated power and equal rated torque a SPM machine occupies less volume. Furthermore, with equal rated power, permanent magnet machines are generally more efficient than induction motors because they are much more less affected by rotor Joule losses. Indeed, the IMs working principle requires that a relevant amount of current is induced in the rotor cage or in the rotor winding, so that additional Joule losses are unavoidable. On the contrary, in permanent magnet machines Joule losses are related to eddy current induced in the PMs; such current is negligible at very low speed and can be severely limited with a proper rotor design even at high speed because it is not involved in the torque generation. Instead, as far as overload requirements are concerned, they could be satisfied in an easier and cheaper way with an IM. Indeed, IMs withstand safer high peak torque values and overload working conditions, while SPM motors could be very limited in terms of overload capability to avoid the permanent magnets' demagnetization, unless very expensive magnets are used. Besides, PMs represent an important constrain also for the allowed working temperatures, while IMs are less sensitive to environmental conditions. For all these reasons, choosing the PM and its sizing is a very challenging key point in the design of a SPM machine. In automotive applications, interior permanent magnet motors are also implemented. With a proper design and control system

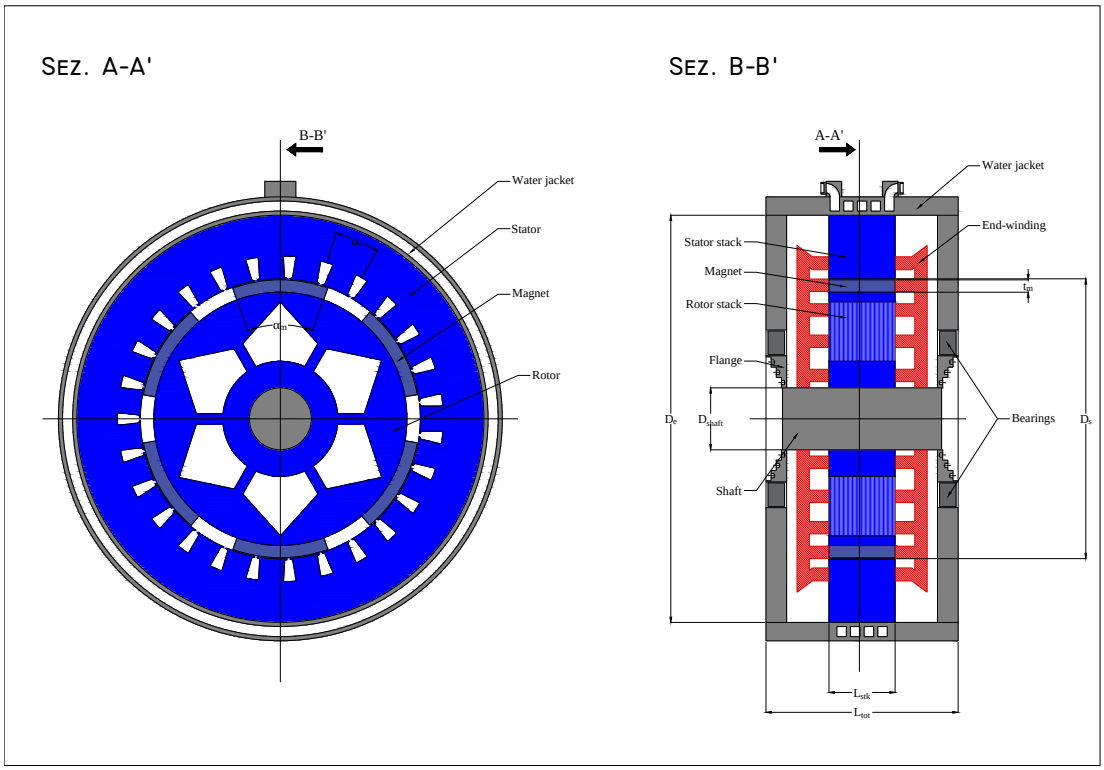

Figure 3.1: Water cooled radial flux SPM motor.

such machines can perform greatly in large speed ranges and the PMs are better shielded against demagnetization. Yet the manufacturing process is more expensive and the design more complex. Hence, these machines could not be worthwhile for the low speed application that concerns this thesis.

The stator core is manufactured stacking a large number of electrical steel laminations with thickness in the range of $0.25 \div 1.00\ [mm]$ until the stack reaches the required length. The electrical steel used in electric motors is a non-oriented grains silicon-iron alloy. A small percentage of silicon (less than 5%) is needed to provide sufficient mechanical strength. Indeed, pure iron is very brittle and it is not able to withstand the cutting process, which is needed to make the slots geometries, without breaking. Whereas most of the alloy (above 95%) is composed by iron in order to fulfill the function for which such material is adopted, i.e. to provide a magnetic circuit path with very low reluctance $\mathcal{R}\ [Aturns/Wb]\ [H^{-1}]$. To do so, the alloy should behave as a so-called soft magnetic material. Generally the magnetic behavior of a material is represented by the constitutive equation:

$$\bar{B} = \mu \bar{H} = \mu_{rel} \mu_0 \bar{H} \tag{3.1}$$

Where $\mu_0 = 4\pi \cdot 10^-7\ [H/m]$ is the absolute permeability of the air, $\mu\ [H/m]$ and μ_{rel} are respectively the absolute and relative permeability of the material, $\bar{B}$ is the magnetic flux density vector and $\bar{H}$ is the magnetic field vector. Non-oriented grains electrical steels are isotropic materials. This means that μ_{rel} assumes the same value regardless of the magnetization direction and Equation 3.1 is still valid in terms of vectors amplitudes B and H. Indeed, anisotropic soft magnetic materials such as oriented grains steels are not suitable for making electrical machines because the stator core is subjected to a rotating field without a preferential magnetization direction. By definition, magnetic reluctance is inversely proportional to permeability:

$$\mathcal{R} \propto \frac{1}{\mu} \propto \frac{1}{\mu_{rel}}$$

Thus an electrical steel should have a high relative permeability μ_{rel} to allow high flux density values $B\,[T]$ with low magnetizing efforts, i.e. low applied magnetic fields $H\,[A/m]$. Unfortunately, such feature is always linked to a magnetic saturation phenomenon in iron alloys which causes a non-linear magnetic behavior. Indeed, Figure 3.2(a) shows that the BH curve of a soft magnetic material is not a straight line. It happens because the relative permeability is not constant, but it depends on the magnetizing effort, so that Equation 3.1 becomes a non-linear relation between B and H:

$$\mu_{rel} = \mu_{rel}(H)$$

The permeability reaches its maximum value near a particular point of the magnetic characteristic called *'knee'*. Beyond the *'knee'*, the permeability rapidly decreases to a value near μ_0, so the gain in the flux density is smaller than the rise in the applied field and consequently it is not worthwhile to apply such high magnetizing efforts. Therefore, a soft magnetic material is exploited conveniently only near the *'knee'*. Moreover, even the material response to an alternating applied field is strongly non-linear, outcoming in the hysteresis loop illustrated in Figure 3.2(a). Such phenomenon produces an energy dissipation into heat that is proportional to the area delimited by the loop curve. Indeed the specific energy loss $w\,[J/m^3]$ is defined as follows:

$$w = \oint BdH$$

So a soft magnetic material should have a very restricted hysteresis loop. The hysteresis losses are added to eddy current Joule losses, which are also triggered by alternating applied fields. It results then in overall iron losses. These losses increase with the frequency of the alternating applied field. Such topic will be investigated later and deeper. The stator core is subjected to an alternating magnetic field both in the time and space domain, i.e. a rotating field. So it is deleterious in terms of efficiency and heat dissipation to build it in a single iron block. Hence the use of a lamination stack. Moreover, laminations are electrically insulated in the axial direction, commonly through very thin oxidation layers or insulating enamels. Such expedient avoids the flow of eddy current induced by the alternating radial magnetic flux and consequently it limits severely the related Joule losses.

The rotor yoke is subjected to a constant magnetic flux in steady state load conditions. Hence it could be manufactured using a single iron block. Yet when a change in the motor load occurs and the feeding current varies rapidly, a magnetic field variation affects the rotor yoke too. Then the resulting losses contribute in worsening the overall efficiency and the reaction field, because the induced eddy current slows down the electromechanical dynamic of the machine. Thus, for this project, a laminated rotor has been adopted. Moreover, thanks to this choice, the inertia of the machine decreases with a further improvement in the electromechanical responsiveness.

The excitation magnetic field is provided by some permanent magnets (PMs) that are pasted on the rotor surface and wrapped with a carbon fiber or fiberglass bandage to prevent runaways at high rotational speed. A permanent magnet is a so-called hard magnetic material. Its BH characteristic is depicted in Figure 3.2(b). It can be observed that a hard magnetic material has a very large hysteresis loop if compared to the one of soft magnetic materials. Therefore, such materials are not suitable to provide low reluctance magnetic paths, but they are used to produce a constant magnetic flux. In order to achieve it, they have to work in the second quadrant of the BH plane, along the so-called recoil line, whose points can be represented by the following equation (namely the recoil line equation):

$$B = B_{rem} - \mu_{rec}\mu_0 H$$

If the working point reaches the so-called *'knee'* the PM is irreversibly demagnetized. The performance of a magnet is measured in terms of remaneance B_{rem}, coercivity H_{cb} and intrinsic field H_{cj}. These parameters will be described thoroughly later, when the magnet choice will be discussed. The PMs are manufactured as arc-shaped blocks that cover the entire stack length. Thus, the number of machine poles is equal to the number of magnets. Sometimes, in critical high speed applications, i.e. above 6000 $[rpm]$, with the objective to limit the Joule losses due

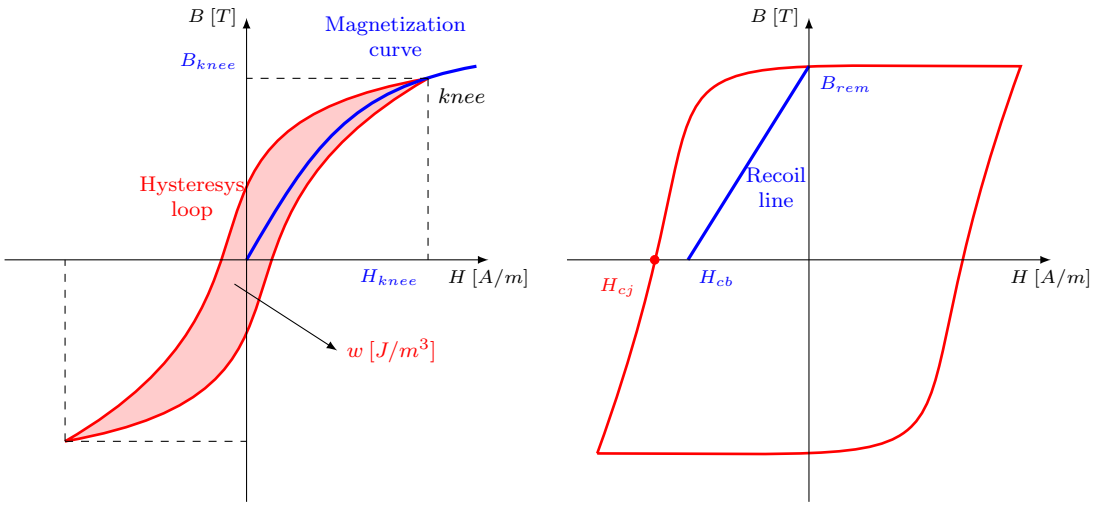

(a) Soft magnetic material

(b) Hard magnetic material

Figure 3.2: Magnetic materials BH characteristics.

to eddy current flowing in the magnets, the machine poles could be composed by many magnet blocks electrically insulated along the axial direction, emulating the expedient used to realize the stator. In other applications, when the motor movement must be very accurate, the PMs are often skewed to minimize the torque ripple. These solutions surely provide better performances but they require more expensive manufacturing techniques. Neither the former case nor the latter concern this project, therefore they have not been adopted. Nevertheless, the magnet losses have been taken into account during the analysis of the motors and the related results will be presented later.

Thanks to the use of permanent magnets, the motor is a brushless machine, as it does not need an excitation winding on the rotor. Hence, brushed contacts are not necessary. A brushless motor has a greater overall efficiency, a better heat dissipation and lower maintenance costs than an equivalent brushed machine. Manufacturing costs are higher because the production of the permanent magnets is much more expensive than a rotor field winding, but the advantages given by the use of PMs justify the costs in an automotive application [32].

The stator laminations are cut to make the slots that house the armature winding coils sides. The motor has a three phase double-layer distributed winding made of copper enameled wires. Such layout has been preferred to a concentrated winding in order to improve the sinusoidal waveform of the back *emf* (*electromotive force*) and reduce the armature reaction, despite a concentrated layout could fit better a compact machine with a low number of slots. Double layer coils has been chosen to allow the creation of fractional-slots winding and to provide an easy implementation of short-pitches, which reduce the torque ripple and the harmonic content of the back *emf* and the armature *mmf* (*magnetomotive force*). Wires have been adopted instead of hair-pins only to reduce the manufacturing costs, even if it has been proven in [33] that hair-pins windings are advantageous in terms of performances and volume reduction for the application under analysis. Photos of the just mentioned windings are given in Figures 3.3-3.4-3.5. In order to provide electrical insulation among different turns and between different coils, the wires are enameled with a polyamide coating and the coils sides are wrapped with Nomex® tapes. Furthermore, the interior surface of the slots is covered with phenolic bakelite paper sheets to guarantee electrical insulation between conductors and mass. Diamagnetic bakelite wedges close the slots to avoid any unwanted movements of the coils sides. Finally, copper conductors have been preferred rather than aluminum wires to allow higher current density.

The motor must have a very high power density to fulfill the displacement constrains. Such purpose can be achieved through the increase of the current density in the armature winding. Therefore, the specific Joule losses increase and liquid cooling systems are needed to avoid excessive overtemperatures that can damage permanently the previous mentioned insulating

Figure 3.3: Concentrated

Figure 3.4: Distributed with wires

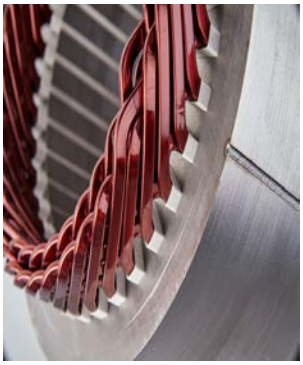

Figure 3.5: Distributed with hair-pins

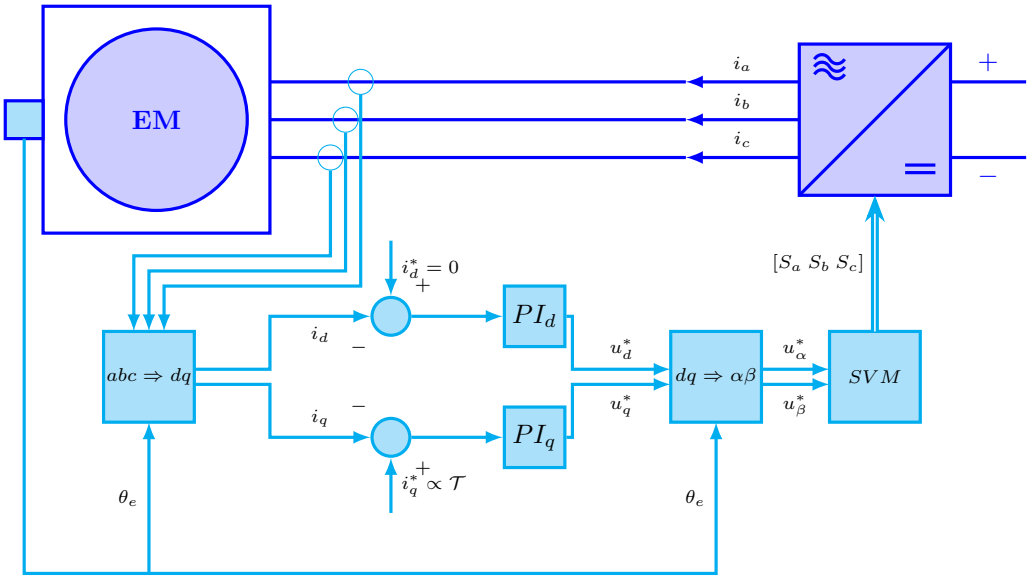

Figure 3.6: Electric drive and control system outline.

materials inside the slots. If the machine would be self-ventilated or air-cooled, it would require a larger outer surface to dissipate the same heat quantity, otherwise the current density would be lower. For this project, an inox steel water-jacket with a circumferential duct has been adopted. An external pump (not shown in Figure 3.1) moves the cooling fluid inside the channel. The water-jacket has to be designed so that it encloses entirely the laminations stack and it provides a proper heat dissipation. The cooling system design will be presented in detail in Chapter 5.

The rotor stack is built around a stainless steel shaft, through which the electromagnetic torque developed by the machine is made available to the powertrain. The shaft is hinged to two bearings inserted inside the front and rear plates that close the machine in axial direction.

3.2 Electric drive and control system

Two main configurations of the control system can be implemented to drive a SPM motor: the machine can be controlled as a BLDC (*brushless DC*) motor, injecting rectangular current waveforms, or it can be fed with sinusoidal current as a BLAC (*brushless AC*) motor. The latter electric drive has been preferred because it provides better torque performance in terms of ripple and harmonic content [31]. The outline of the system is shown in Figure 3.6.

The machine is driven through a torque loop control. The feedback signals are the phase

current, which are instantaneously measured by some current transducers. The three phase signal (i_a, i_b, i_c) are converted into their related dq components, referring to an orthogonal system that rotates at the same speed of the rotor and where the d-axis is aligned with the PM magnetization direction. To perform a synchronous transformation the instantaneous electrical angular position of the rotor $\theta_e[^\circ]$ is needed. So the mechanical angular position θ is measured by an encoder installed on the shaft and consequently the electrical angle is obtained as $\theta_e = p\theta$. The synchronous transformation of a balanced three phase quantity outcomes two constant signals, as represented by the following relations:

$$\begin{array}{ll} i_a = Icos(\theta^e + \theta_i) & \\ i_b = Icos(\theta^e + \theta_i - 120^\circ) & \implies \\ i_c = Icos(\theta^e + \theta_i - 240^\circ) & \end{array} \begin{array}{l} i_d = Icos(\theta_i) \\ \\ i_q = Isin(\theta_i) \end{array} \tag{3.2}$$

To make sure that the phase feeding current have no zero sequence component, the motor winding is star-connected without neutral wire, so that third harmonic current cannot flow. Hence explained why the control system works with quantities defined about a rotating reference. Indeed such signals are constants or step-varying, thus they can be suitably tracked by PI (Proportional-Integral) controllers. The feedback dq quantities are then compared to the reference dq signals (i_d^*, i_q^*). The resulting errors are processed by the PI controllers that produce the dq components of the needed voltage. Such quantities are transformed back to the orthogonal stationary $\alpha\beta$ reference system and then they are given to the SVM (Space Vector Modulation) algorithm that generates the gate signals for the three legs of the inverter.

The machine is always driven in MTPA condition (Maximum Torque Per Ampere). For SPM motors it can be proven that, neglecting any non-linear iron saturation phenomena, the MTPA condition is achieved by the injection of a three phase quadrature current, i.e. with only q axis component in the rotating synchronous system. Thus the i_d^* reference signals is always set to zero so that the phase a starting angle results: $\theta_i = 90^\circ$. Instead the i_q^* reference, which is set by the power management system, defines the average torque value that the motor should develop at any given time. Indeed the instantaneous electromagnetic torque can be expressed in the dq rotating reference by the following well known relation [24, 31]:

$$\tau = \frac{3}{2} p \Im\left[\breve{\lambda}\, \bar{i}\right] + \frac{\partial w^I}{\partial \theta} = \frac{3}{2}\left(\lambda_d i_q - \lambda_q i_d\right) + \frac{\partial w^I}{\partial \theta} \tag{3.3}$$

Where $\breve{\lambda} = \lambda_d - j\lambda_q$ is the space vector of the flux linkage, while $\bar{i} = i_d + j i_q$ is the space vector of the feeding current. The variation coenergy $\partial w^I / \partial \theta$ is not involved in the mean torque development, but it generates only the torque ripple component. SPM motors have an isotropic magnetic circuit. This means that the magnetic reluctances along axis d and q are equal. Indeed the differential permeability of the magnets is quite similar to the relative permeability of air ($\mu_{rec} \cong 1$). Therefore also the inductances of axis d and q are the same: $L_d = L_q$. Under these statements and still neglecting any non-linearity, Equation 3.3 becomes:

$$\mathcal{T} = \frac{3}{2} p \Lambda_0 i_q$$

Where Λ_0 is the peak value of the magnetic flux produced by the PM and linked with the winding in unload condition. The previous expression states that in a SPM machine only the quadrature component of the current generates an average torque. That is why the MTPA condition requires only q component. So, when working in MTPA, Equation 3.3 can be further expressed as follows:

$$\mathcal{T} = \frac{3}{2} p \Lambda_0 I \tag{3.4}$$

Thus the mean torque results proportional to the peak current I.

Figure 3.7 reports the steady-state working regions of a SPM machine in the $i_d - i_q$ plane and the mechanical characteristic of this kind of motor. It can be seen that the rated torque, which in the drawing corresponds to the maximum torque, is available in MTPA condition until the so-called base speed Ω_B. For speed values higher than Ω_B the voltage limit forces the

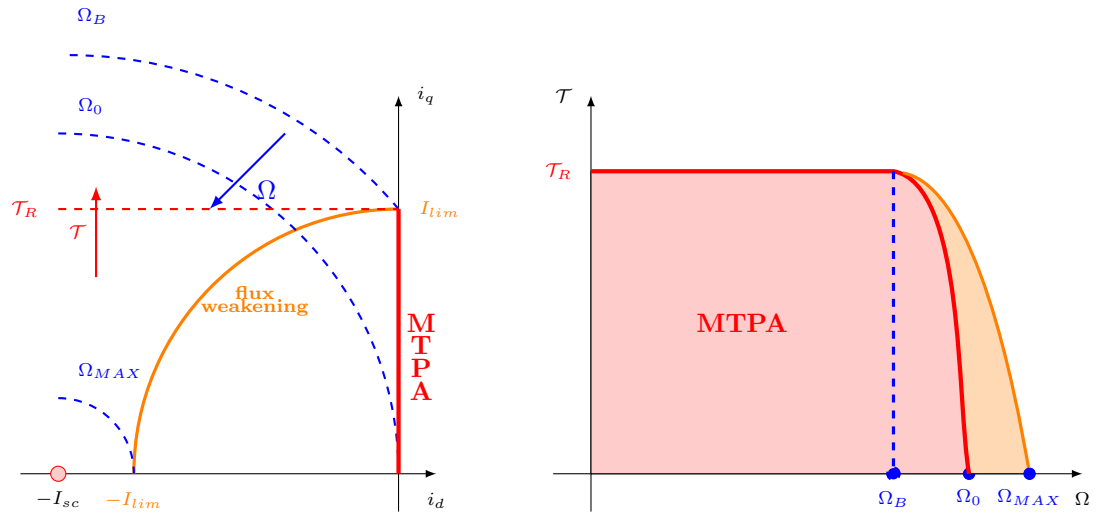

(a) Working regions

(a) Mechanical characteristic

Figure 3.7: Steady-state working regions (a) and mechanical characteristic (b) of a SPM motor.

electric drive to operate in flux-weakening mode, i.e. with an amount of demagnetizing feeding current given by a negative d-axis component. The MTPA region is still available but the torque outcomes lower than the flux-weakening curve at equal speed. However beyond the base speed the maximum torque that can be developed is smaller, as the mechanical characteristic bends down. SPM motors have a limited flux-weakening region because they present very low inductances. So they are commonly designed to work always in MTPA condition, not further of Ω_B. Thus in this project the base speed corresponds to the rated speed. It can be stated that the three motors have been designed according to the base point features. A detailed dissertation about these topics is provided in [24, 31, 34].

3.3 Design specifications and volume constrains

Three SPM motors have been designed for the mild-hybrid powertrain with the downsized ICE FPT N67ENT 175 $[kW]$ (238 $[Hp]$). The main difference between the three motors consists in the number of poles $2p$. The specifications identified after the hybridization tests and reported in Table 2.1 require high rated and overload torque and a relatively low rated speed. Such requirements lead to the design of so-called torque motors, which are characterized by low machine ratios, i.e. larger stator inner diameters compared to the axial stack length, and high numbers of poles. But, with equal rated speed n_R $[rpm]$, synchronous machines with high numbers of pole pairs p require feeding current with high rated frequency f_R $[Hz]$, as stated by the following well known relation [24]:

$$f_R = \frac{p n_R}{60}$$

A three-phase voltage with the same fundamental frequency must be synthesized by the inverter, which should work at a very high switching frequency to produce clean sinusoidal waveforms, otherwise the harmonic content of the feeding current could affect the performances and the efficiency of the entire electric drive. To do so more expensive electronic power switches are needed and even with high-performance components the inverter losses increase with the square of the switching frequency. Moreover the machine unload losses, which are due mainly to iron hysteresis, increase more than linearly with the fundamental electrical frequency. So, for the application that concerns this project is recommended not to overcome the fundamental electrical frequency of 200 $[Hz]$. Thus machines with a number of poles from 6 to 10 have been

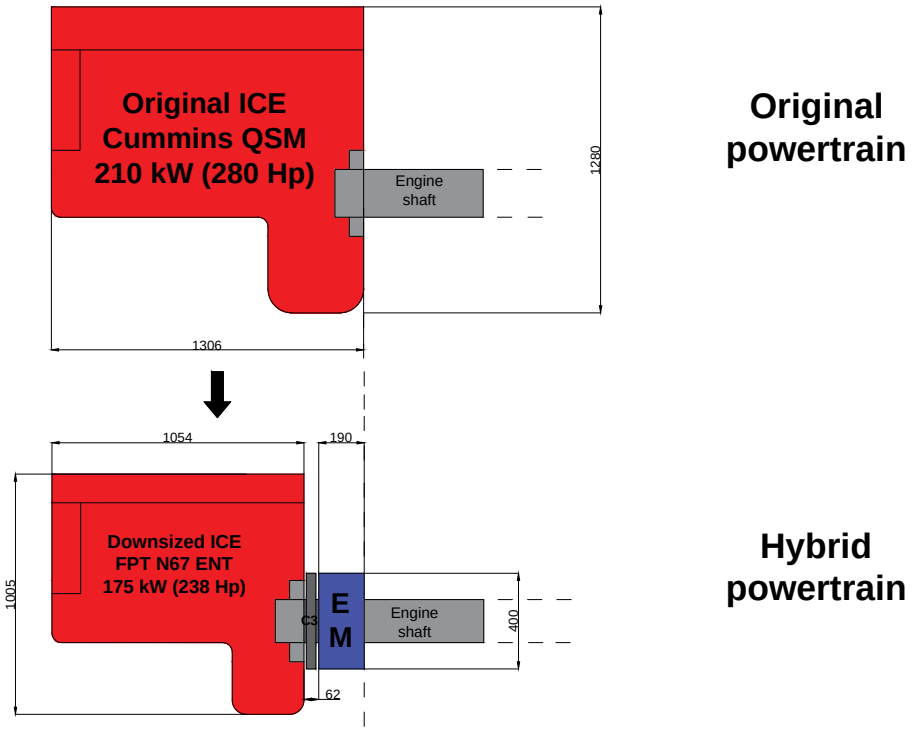

Figure 3.8: Size constrains in the mild-hybrid powertrain.

Specification	Symbol		Value		Unit
Rated torque	$\mathcal{T}_R$		120		$[Nm]$
Rated speed	n_R		2300		$[rpm]$
Rated power	P_R		29		$[kW]$
Max. overload torque	$\mathcal{T}_{OL}$		$4 \times \mathcal{T}_R$		$[Nm]$
Number of poles	$2p$	6	8	10	
Rated frequency	f_R	115	153	192	$[Hz]$
Size constrains					
Max. total axial length	$L_{tot_{MAX}}$		190		$[mm]$
Max. total outer diameter	$D_{tot_{MAX}}$		400		$[mm]$

Table 3.1: Design specifications and size constrains.

designed.

Displacement constrains are also very important in this application. In order to realize a cost-effective hybrid powertrain, the electrical machine must occupy no more than the volume made available by the engine displacement's reduction, otherwise very expensive modifications of the tractor chassis could be required. Then the maximum sizes suitable for the EM have been identified looking at the commercial datasheets of the chosen original engine and downsized ICE [27, 30]. The original engine has a declared length of 1306 $[mm]$ while the downsized ICE is 1054 $[mm]$ long, clearing a space of $1306 - 1054 = 252$ $[mm]$ along the shaft. Considering to allocate 62 $[mm]$ for the optional clutch between the ICE and the EM and for the needed mechanical connections, the total axial length of the electric motor should not overcome $L_{tot_{MAX}} = 190\,[mm]$. The maximum total outer diameter of the machine has been supposed of $D_{tot_{MAX}} = 400\,[mm]$, as the shaft is installed near the lower side of the engine. The reasoning just presented above is illustrated in Figure 3.8. All the design specifications are summarized in Table 3.1.

3.4 Choice of the permanent magnet

Before the preliminary sizing of the machines the permanent magnet type must be chosen. The choice has been based on the behavior of hard magnetic materials and on the well-known sizing torque relation of synchronous radial flux motors, which is derived by a force balance at the air gap of an equivalent ideal machine [24].

$$\mathcal{T}_R = \frac{\pi}{4} D_s^2 L_{stk} \hat{B}_{gR}^{(1)} \hat{K}_{sR} \tag{3.5}$$

D_s and L_{stk} are the main electromagnetic sizes, respectively the inner stator diameter and the stack axial length. $\hat{B}_{gR}^{(1)}$ is the fundamental peak value of the magnetic flux density distribution in the air gap ($[T]$) at rated load, i.e. the amplitude of the first harmonic of the distribution, also called magnetic load. $\hat{K}_{sR}$ is the rated electric load peak value, which is defined as the amplitude of the linear current density ($[A/m]$) that would flow on the inner surface of the ideal machine's stator. The choice and computations of these parameters will be presented in the next section, as the preliminary sizing consists exactly in finding out the main dimensions D_s and L_{stk}. But, to do so, the magnet type must be previously selected.

All the machine parameters depends heavily on this choice, but primarily it affects the flux density distribution in the air gap. The performances of a magnet are measured in terms of remaneance B_{rem}, coercivity H_{cb} and intrinsic field H_{cj}. These parameters are shown in Figure 3.2(b). In particular, $\hat{B}_{gR}^{(1)}$ depends heavily on B_{rem}. PMs with higher remaneance allow higher flux density in the air gap. Hence the machine could have a smaller size and smaller electric load, resulting to be more compact, more efficient and easier to cool. Strong magnets are characterized by high energy density. Usually they have high coercivities and also high remaneances. Other significant key points that must be considered in the magnet choice are the resistance against the demagnetization and the temperature stability, which strongly depend on each other. A PM is all the more difficult to demagnetize as it has a high intrinsic field value. But this feature could not be enough in those applications when the working temperature varies in a large range. Indeed the intrinsic field value as well as the remaneance of a permanent magnet tend to decrease with an increasing working temperature. Consequently the PM becomes more sensitive to demagnetization and its performances drop down. Last but not least, the cost of the magnet material and the manufacturing process must be taken into account as the PMs represent about the 70% of the overall cost of the machine.

Four kinds of permanent magnet materials can be used in an electrical machine. Ferrite magnets, also known as ceramic magnets, are the cheapest PMs available. They are electrical insulating, corrosion free and very resilient against harsh environments [35]. On the other hand they have the lowest performances in terms of remaneance and coercivity. Furthermore their remaneance decreases heavily with a working temperature rise, but, on the contrary, their intrinsic field increases. Thus, the temperature is not a problem in terms of demagnetization for this kind of magnets, but it affects only the performances. AlNiCo magnets (Aluminum-Nickel-Cobalt) are characterized by the highest remaneances (up to 1.4 $[T]$) and the highest thermal stability [36]. Unfortunately their coercivities and intrinsic fields are very low, then these kind of magnets are the weakest against the demagnetization. So they are rarely adopted in electrical machines and, even for those particular applications where they could be usefully exploited, the design results very challenging. As best practice, their use should be avoided when high overload current are involved. Finally rare-earth magnets are commonly used in electrical machines. Two kind of these PMs can be adopted. NdFeB sintered alloys (Neodimium-Iron-Boron) are the cheaper ones, but anyway they are several times more expensive than ferrite magnets. They are the stronger PMs available [37], with coercivities up to 1000 $[kA/m]$ and remaneances up to 1.3 $[T]$, but they suffer a lot when a rise in the working temperature occurs, in terms of both performances and weakening against demagnetization. High-temperature NdFeB PMs withstand demagnetizing reaction fields quite better. Clearly they are more expensive as they require small percentages of the so-called ultra-rare earths, like Disprosium and Gadolinum. NdFeB magnets are always provided with a NiCuNi (Nickel-Copper-Nickel) coating to prevent corrosion. However such kind of PMs are not suitable to work in especially harsh environments.

The other type of rare-earth PMs are the SmCo alloys (Samarium-Cobalt). They exhibits lower remaneance and coercivity values than NdFeB alloys, but they are much more stable with the temperature and stronger against demagnetization [38]. Moreover they are less affected by corrosion and humidity. Unfortunately such magnets are the most expensive due to the presence of cobalt.

In this project AlNiCo PMs are rejected firstly due to the great overload capability specification and the high demagnetizing current involved. When possible, ferrite magnets should be preferred to rare-earth PMs in order to obtain a cost-effective machine. However, for the chosen type of EM, the machine specifications cannot be fulfilled using ferrite magnets. To prove this statement a brief preliminary sizing has been performed adopting unfeasible but conservative hypothesis.

The magnetic parameters of the most high-performance ferrite magnet, namely Y40 grade [35], has been assumed at the working temperature of $100°C$:

- a remaneance $B_{rem} = 0.40\,[T]$;
- an intrinsic magnetic field $H_{cj} = 450\,[kA/m]$;
- a differential permeability of the recoil line $\mu_{rec} = 1$, i.e. the slope of the line.

The intrinsic magnetic field can be approximate with the *'knee'* magnetic field value $H_{knee} = H_{cj}$ in a security-side way. Then the *'knee'* flux density value B_{knee} has been obtained from the recoil line equation as follows:

$$B_{knee} = B_{rem} - \mu_{rec}\mu_0 H_{knee} = -0.17\,[T]$$

The working point of the magnet must not go under the *'knee'*, otherwise the PM outcomes demagnetized.

The thickness of the magnet has been set to $t_m = 12\,[mm]$ to provide a good strength against demagnetization. Considering an air gap thickness of $g = 1\,[mm]$, the equivalent magnetic air gap has been hypothesized as $g^{II} = 1.3\,[mm]$. Hence, the flux density value in the air gap results from the computation of the equivalent magnetic circuit of the machine at rated load:

$$\hat{B}_g = \frac{B_{rem}}{1 + \frac{\mu_{rec} g^{II}}{t_m}} = 0.36\,[T]$$

Supposing a flux density square-wave distribution in the air gap and that the magnet covers an entire pole pitch, the amplitude of the fundamental flux density has been computed as follows:

$$\hat{B}_{gR}^{(1)} = \frac{4}{\pi}\hat{B}_g = 0.46\,[T]$$

The flux density in the air gap can be considered the same value that define the working point of the magnet $B_m = \hat{B}_g = 0.36\,[T]$, because the PMs are placed in front of the air gap. Hence the demagnetization margin in terms of flux density ΔB_{demg} has also been derived:

$$\Delta B_{demg} = B_m - B_{knee} = 0.53\,[T]$$

At rated load a large security coefficient $k_{secR} = 8$ has been adopted to avoid demagnetization even when the maximum overload is applied. So the allowed flux density variation for the PM working point has outcome:

$$\Delta B_R = \frac{\Delta B_{demg}}{k_{secR}} = 0.07\,[T]$$

Considering the maximum total outer diameter of the machine $D_{tot_{MAX}} = 400\,[mm]$, a stator maximum inner diameter $D_s = 300\,[mm]$ has been chosen, leaving a minimum radial length of $100\,[mm]$ for the laminations height and the water jacket thickness. Then the peak rated electric load has been computed through the reaction field relation for the 10 poles machine,

		N27 UH	N35 UH	N42 UH
Remaneance	$B_{rem}^{20^\circ}$ $[T]$	1.03	1.17	1.28
Coercivity	$H_{cb}^{20^\circ}$ $[kA/m]$	764	875	875
Intrinsic field	$H_{cj}^{20^\circ}$	1989	1989	1989
Energy density	BH_{max} $[kJ/m^3]$	199	263	318
Temp.coeff.induction	α_{Brem} $[\%/^\circ C]$	-0.1	-0.1	-0.1
Temp.coeff.intrinsic	α_{Hcj} $[\%/^\circ C]$	-0.55	-0.55	-0.55
Max.temperature	$T_{m_{MAX}}$ $[^\circ C]$	180	180	180

Table 3.2: Selected NdFeB sintered magnets for preliminary sizing.

which withstand better the demagnetization and consequently it allows higher current loads:

$$\hat{K}_{sR} = \frac{2p\Delta B_R(g^I + \frac{t_m}{\mu_{rec}})}{\mu_0 D_s} \cong 24\,[kA/m]$$

The air gap has been raised to $g^I = 1.1\,[mm]$ to consider the magnetic reluctance due to slots openings. Finally, remembering that $\mathcal{T}_R = 120\,[Nm]$ and using the well-known sizing torque equation for synchronous radial flux machines, the stack length has been obtained:

$$L_{stk} = \frac{4\mathcal{T}_R}{\pi D_s^2 \hat{B}_{gR}^{(1)} \hat{K}_{sR}} = 154\,[mm]$$

The resulting axial size does not fulfill the volume constrains because with such stack length the EM would surely becomes longer than $L_{tot_{MAX}} = 190\,[mm]$, considering the space needed for the end-windings and the front and rear plates. Moreover some suppositions made during the sizing are unfeasible and too optimistic. Therefore it has been stated that ferrite magnets are not suitable for this project, as they do not allow to fulfill the volume constrains even in the best scenario.

So rare-earth magnets must be adopted. Among them sintered NdFeB magnets have been preferred rather than SmCo alloys for cost-related reasons. Nevertheless in the application under analysis temperature stability as well as strength against the demagnetization are also required. Indeed the machine will be placed very close to a Diesel engine and power electronic components, which are relevant heat sources. Furthermore the EM should withstand high overload peak torque with consequently high specific Joule losses. For this reasons the high-temperature UH class has been chosen. UH alloys, that are not the top-performance ones, guarantee a declared maximum working temperature of $180^\circ C$, an intrinsic field $H_{cj}^{20^\circ} = 1989\,[kA/m]$ at room temperature and variations of B_{rem} and H_{cj} with the temperature respectively of $\alpha_{Brem} = -0.1\,\%/^\circ C$ and $\alpha_{Hcj} = -0.55\,\%/^\circ C$ [37]. As what concerns the grade, three options has been tried and compared during the preliminary sizing. The parameters of the three magnets at room temperature are reported in Table 3.2. The data have been taken from the minimum values in [37], according to the Chinese standard. Extracts of the datasheet are reported in Appendix 5.3.

3.5 Preliminary sizing

The commonly implemented preliminary sizing methods find out the machine main sizes D_s and L_{stk} through Equation 3.5 and by imposing a security margin against the demagnetization [24], likewise the procedure presented in the previous section that has been followed to exclude ferrite magnets. The air gap thickness must be previously chosen and some feasible hypothesis on the saturation at rated load must be done. Also the magnet parameters must be known and its shape and thickness must be selected. To achieve their goal, these methods require to set at least one size between D_s and L_{stk} or alternatively their ratio L_{stk}/D_s, namely the machine aspect ratio. In order to identify the best choice, many trials are usually performed varying the input parameters such as the air gap thickness, the PM size or the machine aspect ratio, in a

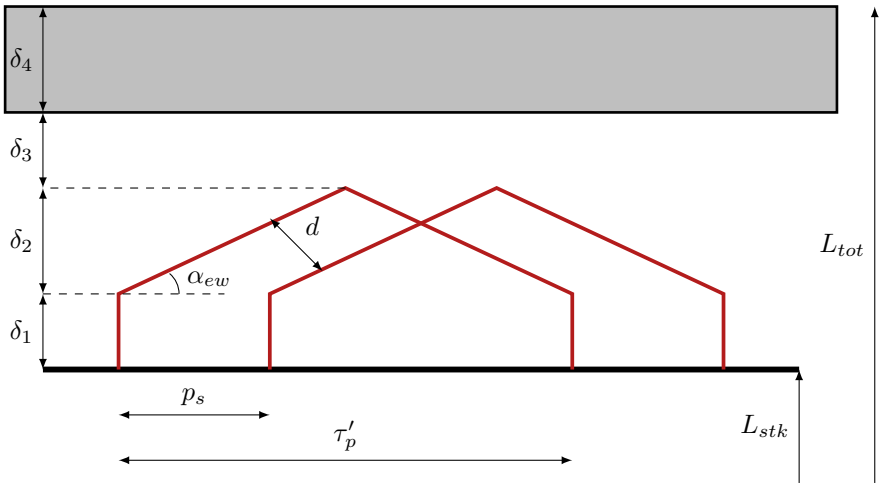

Figure 3.9: End-winding geometry.

range of feasible values. Nevertheless such methods are focused only on the stack length sizing, so the machine total displacement cannot be known until the stator dimensions and the winding features are completely defined. Therefore it is very complicated to fulfill size constrains. Then an alternative procedure has been adopted to exploit wisely the available volume.

The main purpose is to take advantage of the total axial length limit as much as possible, because it represents the major size constrain considering that a radial flux motor has been chosen. Hence the total axial length has been imposed equal to the maximum axial dimension allowed.

$$L_{tot} = L_{tot_{MAX}} = 190\,[mm]$$

The geometry of the end-winding has been studied at the beginning. Figure 3.9 outlines the end-turns of a distributed winding with all the geometrical dimensions used in the sizing procedure. The layout shown in Figure 3.9 can be realized both with wires and hair-pins, so the method can be also adopted to size hair-pins windings. The machine total length is related to the stack length as follows:

$$L_{tot} = L_{stk} + 2(\delta_1 + \delta_2 + \delta_3 + \delta_4) \tag{3.6}$$

The dimensions δ_1, δ_3 and δ_4 are independent parameters that must be set feasibly by the designer. In this project the values chosen for all the EMs are: $\delta_1 = \delta_3 = 10[mm]$, $\delta_4 = 20[mm]$. Instead δ_2 depends on the motor geometry.

$$\delta_2 = \frac{\tau'_p}{2}\tan(\alpha_{ew}) \tag{3.7}$$

Where the end-winding slope angle α_{ew} can be further developed:

$$\alpha_{ew} = \arcsin\left(\frac{d}{p_s}\right)$$

d is a distance fixed by the designer: in this project $d = 10\,[mm]$ has been set to guarantee a sufficient heat dissipation through natural convection in air. The slot pitch p_s is related to D_s and to the number of slots Q_s:

$$p_s = \frac{\pi D_s}{Q_s}$$

The coil span τ'_p cannot be known until the winding layout is completely defined, but it can be approximated with the pole pitch τ_p in a conservative way. Indeed, $\tau'_p = \tau_p$ in case of integer

Table 3.3: Magnets parameters at working temperature.

		N27 UH	**N35 UH**	**N42 UH**
Diff. permeability	μ_{rec} [/]	1.07	1.06	1.16
Working temp.	T_m [°C]	120	120	120
Remaneance	B_{rem} [T]	0.927	1.053	1.152
Coercivity	H_{cb} [kA/m]	688	787	788
'Knee' field	H_{knee} [kA/m]	-895	-895	-895
'Knee' induction	B_{knee} [T]	-0.28	-0.14	-0.16

slot windings, while $\tau'_p < \tau_p$ when a chorded winding is adopted. So if a short-pitch will be implemented the end-turns will outcome a bit shorter than expected, but the axial dimension constrain will be fulfilled anyway. The pole pitch depends on D_s and on the number of poles:

$$\tau_p = \frac{\pi D_s}{2p}$$

Then, Equation 3.7 can be rewritten substituting the previous expressions:

$$\delta_2 = \frac{\pi D_s}{4p} \tan\Big(\arcsin\Big(\frac{dQ_s}{\pi D_s}\Big)\Big) \tag{3.8}$$

The stack length can be obtained from Equation 3.5.

$$L_{stk} = \frac{4\mathcal{T}_R}{\pi D_s^2 \hat{B}_{gR}^{(1)} \hat{K}_{sR}} \tag{3.9}$$

The rated magnetic load $\hat{B}_{gR}^{(1)}$ is computed starting from the PM parameters in the same way presented in the previous section. The remanenance B_{rem} and the *'knee'* flux density value B_{knee} are computed at the supposed working temperature of 120°C using the temperature coefficients and the recoil line equation. The results are reported in Table 3.3 for each PM under analysis. The flux density of the magnet working point at rated load is expressed as follows:

$$B_m = \hat{B}_g = \frac{B_{rem}}{1 + \frac{\mu_{rec} g^{II}}{t_m}} \tag{3.10}$$

As explained in the previous section, the flux density value in the magnet and in the air gap can be supposed equal. The magnetic equivalent air gap g^{II} is given by:

$$g^{II} = g^I k_{satR} = g k_{carter} k_{satR} = 1.32\,[mm] \tag{3.11}$$

The air gap thickness has been chosen of $g = 1\,[mm]$ for all the three machines, including $0.6\,[mm]$ of air and $0.4\,[mm]$ of diamagnetic fiberglass bandage for the magnets. The Carter coefficient, which takes into account the reluctance due to slot openings, has been feasibly supposed $k_{carter} = 1.1$, while the saturation coefficient, which considers the *mmf* needed to magnetize the iron paths at rated load, has been set to $k_{satR} = 1.2$. The thickness of the PM t_m must be chosen by the designer; more than one size has been tried.

A PM covering of 2/3 of the pole pitch has been selected for all the motors, as it can be proven that such choice gives the best ratio between the resulting amplitude of the flux density fundamental distribution $\hat{B}_{gR}^{(1)}$ and the PM volume. Hence, the electrical covering angle of the magnet is $2\alpha_m^e = 120°$. So, supposing a square-wave distribution of the flux density in the air gap, the expression of the rated magnetic load becomes:

$$\hat{B}_{gR}^{(1)} = \frac{4}{\pi} \hat{B}_g \sin(\alpha_m^e) = \frac{2\sqrt{3}}{\pi} \hat{B}_g \tag{3.12}$$

And the substitution of Equation 3.10 yields to:

$$\hat{B}_{gR}^{(1)} = \frac{2\sqrt{3}}{\pi} \frac{B_{rem}}{1 + \frac{\mu_{rec} g^{II}}{t_m}} \tag{3.13}$$

Considering a $\times 4$ overload capability the security factor against demagnetization at rated load has been set to $k_{secR} = 8$, so that the margin at maximum overload should be near $k_{secOL} \cong 2$. Then the allowed variation of flux density is expressed as follows:

$$\Delta B_R = \frac{|B_{knee} - B_m|}{k_{secR}} = \frac{|B_{knee} - \frac{B_{rem}}{1 + \frac{\mu_{rec} g^{II}}{t_m}}|}{k_{secR}} \tag{3.14}$$

So the rated electric load can be derived as:

$$\boxed{\hat{K}_{sR} = \frac{2p\Delta B_R \left(g^I + \frac{t_m}{\mu_{rec}}\right)}{\mu_0 D_s}} \tag{3.15}$$

Now, Equation 3.6 can be written by substituting the Equations 3.8-3.9 and after some manipulations:

$$\boxed{\frac{\pi}{2p} \tan\left(\arcsin\left(\frac{dQ_s}{\pi D_s}\right)\right) D_s^3 + \left[2(\delta_1 + \delta_3 + \delta_4) - L_{tot}\right] D_s^2 + \frac{4\mathcal{T}_R}{\pi \hat{B}_{gR}^{(1)} \hat{K}_{sR}(D_s)} = 0} \tag{3.16}$$

The just found Equation 3.16 appears in the form:

$$f(D_s) = 0$$

Indeed the left hand side is a non-linear function $f(D_s)$ in the variable D_s. It is relevant to notice that in Equation 3.16 is underlined that inside f also the electric load is a function of D_s ($\hat{K}_{sR}(D_s)$), according to what is expressed in Equation 3.15. However, all the other quantities inside f are constant or they depend only on the parameters Q_s, t_m, B_{rem} and B_{knee}. To obtain suitable results, some constrains on the solution of Equation 3.16 have been applied. First of all, looking at the argument of the trigonometric part of f, the function exists in a real domain only if:

$$D_s > \frac{dQ_s}{\pi}$$

Moreover a maximum size of 300 $[mm]$ has been imposed for D_s in order to keep a minimum margin of 100 $[mm]$ for the stator laminations height and for the water-jacket thickness. Thus the solution must lie in the range:

$$\frac{dQ_s}{\pi} < D_s \leq 300$$

Otherwise it is excluded.

Equation 3.16 can be solved with a Newton based root-finding algorithm. If applied to the function f under analysis, these algorithms converges always, provided that proper starting points are given. For simplicity reasons, in this project the secant method has been used, as it does not require the analytical computation of the derivative of $f(D_s)$, although it needs two starting points. The algorithm has been implemented in a Matlab® script. Many trials are computed changing the parameters from which the function f depends on: B_{rem} and B_{knee} are related to the PM grade; values of t_m have been accepted until 12 $[mm]$, above which it has been supposed that the manufacturing of the PM becomes more complex; the number of slots has been selected so that the slots per pole and per phase q_s outcomes integer or integer ± 0.5, i.e. $1 - 1.5 - 2 - 2.5-$ etc..., because it is known that such winding layouts reduce the harmonic content of the *mmf* and the torque ripple. Furthermore machines with rated electric loads out of the range $20 \div 50$ $[kA/m]$ are excluded, as for $\hat{K}_{sR} > 50$ $[kA/m]$ the cooling could become complicated even with a water-jacket, while for $\hat{K}_{sR} < 20$ $[kA/m]$ the machine is too

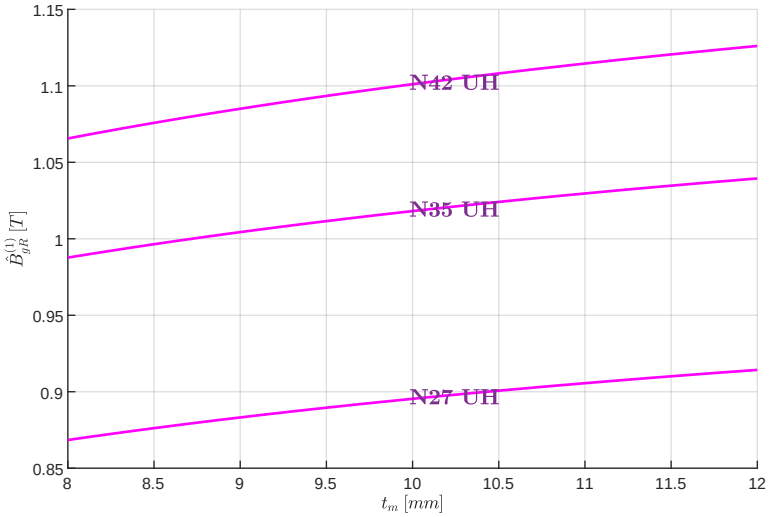

Figure 3.10: Rated magnetic load as a function of magnet thickness on varying the PM grade.

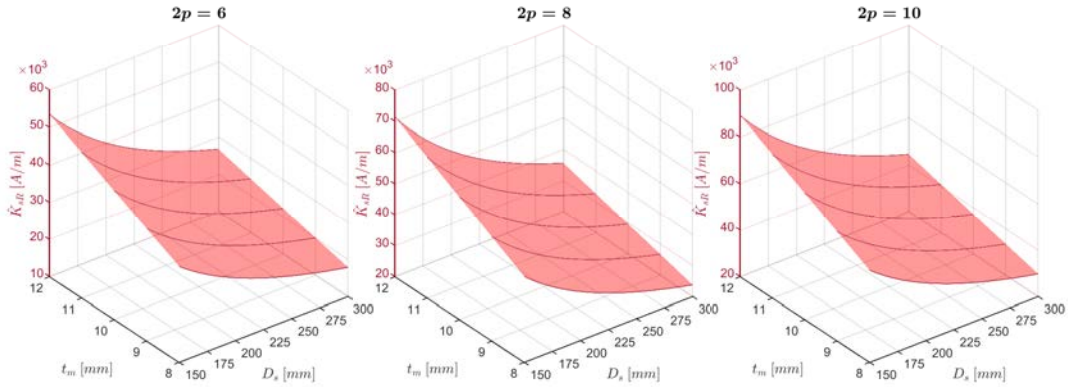

Figure 3.11: Rated electric load as a function of magnet thickness and inner stator diameter on varying the number of poles.

little electrically exploited and consequently not convenient.

According to Equation 3.13 the PM grade, i.e. B_{rem}, affects heavily the magnetic load, which instead depends less on the magnet thickness t_m, as shown in Figure 3.10. On the contrary the PM grade has no effects on the electric load, which depends greatly on t_m, as represented by the parametric surfaces in Figure 3.11. Indeed the chosen NdFeB magnets belong to the same class, so their *'knee'* points are very close, resulting in an equal behavior against demagnetization. Yet an increase in the magnet thickness allows to withstand higher demagnetizing current, outcoming in more compact machines with greater electric loads. Finally, Figure 3.12 shows the behavior of the sizing function f for 8 and 10 poles motors on varying the above mentioned parameters. It can be seen that f does not present a root in the selected range of D_s for all the selections of the parameters. In particular there are never satisfactory solutions if $q_s > 1.5$, for all the three numbers of poles. Besides it is interesting to notice that f has the dimension of a volume ($[dm^3]$). This happens maybe because it is related to displacement constrains.

The admissible outcomes from the secant algorithm within the related electric and magnetic rated loads are reported in Table 2.4. The resulting main sizes have been rounded to the unit of millimeters. All the accepted attempts present low machine ratios ($L_{stk}/D_s = 0.2 \div 0.3$), typical feature of torque motors but a disadvantage for the efficiency. It can be seen that machines with a higher number of poles withstand better the demagnetization, thus they allow higher electric loads at equal PM thickness. Then, the use of high grade magnets makes the motors more compact. Yet the parameter which affects more the inner stator diameter is the PM thickness.

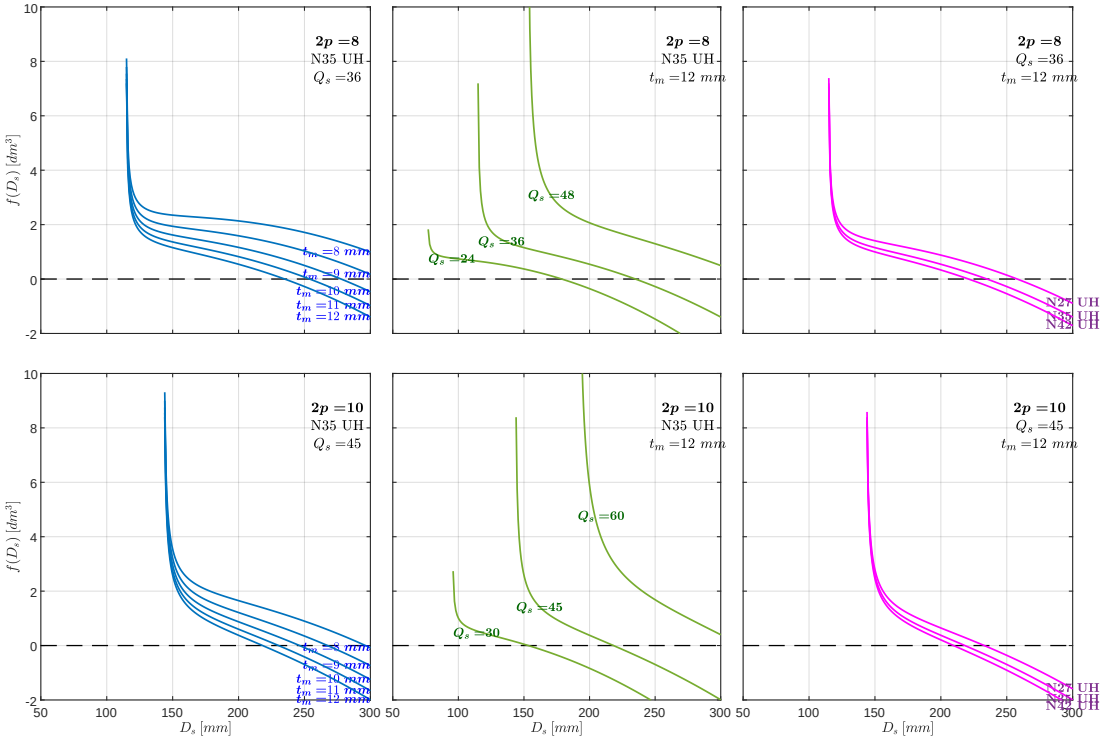

Figure 3.12: Sizing function on varying all the parameters.

Indeed increasing t_m higher electric loads are allowed, so the inner stator diameter decreases.

Table 2.4: Sizing trials.

PM grade	Q_s	t_m $[mm]$	D_s $[mm]$	L_{stk} $[mm]$	$\hat{K}_{sR}$ $[kA/m]$	$\hat{B}_{gR}^{(1)}$ $[T]$	Vol_m $[dm^3]$
(UH class)		≤ 12	≤ 300		$20 \div 50$		
			$2p = 6$				
N27	**18**	11	285	79	26.2	0.91	0.497
		12	260	79	31.3	0.91	0.489
N35	**18**	10	283	79	23.6	1.02	0.450
		11	255	79	28.9	1.03	0.441
		12	232	79	34.6	1.04	0.432
	27	12	292	63	27.6	1.04	0.438
N42	**18**	10	262	79	25.5	1.10	0.415
		11	236	79	31.2	1.11	0.406
		12	215	79	37.4	1.13	0.397
	27	11	296	63	24.8	1.11	0.411
		12	271	63	29.7	1.13	0.403
			$2p = 8$				
N27	**24**	9	270	79	30.3	0.88	0.383
		10	241	78	37.6	0.90	0.375
		11	218	78	45.7	0.91	0.367
	36	11	280	61	35.6	0.91	0.373

		12	258	60	42.0	0.91	0.366
N35	**24**	8	276	79	25.9	0.99	0.350
		9	242	78	33.2	1.00	0.341
		10	217	78	41.3	1.02	0.333
	36	10	278	61	32.1	1.02	0.337
		11	254	60	38.6	1.03	0.331
		12	235	58	45.5	1.04	0.325
N42	**24**	8	256	79	27.8	1.07	0.324
		9	225	78	35.7	1.09	0.315
		10	201	78	44.4	1.10	0.307
	36	9	289	61	27.8	1.09	0.318
		10	261	60	34.3	1.10	0.311
		11	239	59	41.2	1.11	0.304
		12	222	57	48.4	1.13	0.299
$2p = 10$							
N27	**30**	7	289	78	27.6	0.85	0.320
		8	250	78	36.4	0.87	0.312
		9	222	77	46.1	0.88	0.304
	45	9	291	58	35.1	0.88	0.308
		10	267	57	42.5	0.90	0.302
N35	**30**	7	261	78	29.9	0.97	0.287
		8	226	77	39.5	0.99	0.278
	45	8	297	59	30.1	0.99	0.281
		9	268	57	37.5	1.00	0.274
		10	247	55	45.2	1.02	0.268
N42	**30**	6	289	78	23.1	1.01	0.276
		7	244	77	32.1	1.04	0.266
		8	211	76	42.3	1.07	0.257
	45	8	280	58	31.9	1.07	0.260
		9	254	55	39.6	1.09	0.253
		10	235	53	47.5	1.10	0.247

For each motor, the final choice between the different attempts has been based on cost-effectiveness reasons. In a PM motor the magnets represent about the 70% of the overall cost, so the volume of the arc-shaped PMs Vol_m $[dm^3]$ has been computed as follows for every admissible machine:

$$Vol_m = 2\alpha_{m_{[rad]}} \frac{D_s - 2g - t_m}{2} t_m L_{stk} 2p = 2\alpha^e_{m_{[rad]}} (D_s - 2g - t_m) t_m L_{stk} \tag{3.17}$$

Where $\alpha_m = \alpha^e_m / p$ is the mechanical covering angle of the PMs. Table 2.4 reports also these quantities.

The volume of magnets depends heavily on the PM thickness and on the number of poles. Machines with more poles and thicker magnets require less PM material. It can be see that make the magnets thicker has advantages in terms of size, electric load and magnet usage. Therefore, even if it may seem odd, increasing the PM thickness helps a lot in reducing the machine cost. A threshold of 12 $[mm]$ has been set to t_m because it has been supposed that over this value the production of the PM could become more expensive.

However, to assess properly which is the most cost-effective choice for every motor, the specific cost (€$/dm^3$) of each magnet grade should be available, or at least the percentage increment between the specific costs of the three NdFeB grades under analysis must be known.

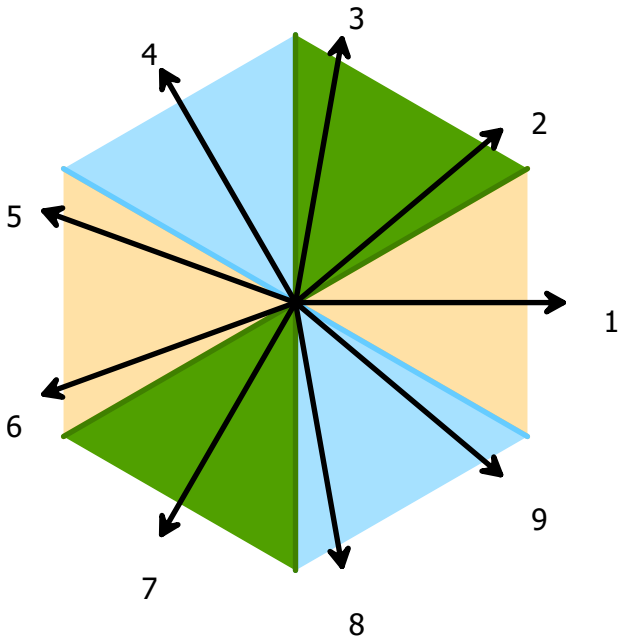

Figure 3.13: Star of slot

Unfortunately NdFeB magnets price changes a lot between different manufacturers and valid cost-related information have not been found for this project. Some reasonings on cost increments in relation to the magnet volume variations between the different attempts have been made. Nevertheless, without reliable price specifications, the final choices have been based on the supposition that the N42 grade leads to the most affordable machines. The selected values after the preliminary sizing are underlined in Table 2.4. It is important to specify that such sizes are not the final ones, but they could be modified a bit during the next steps of the design procedure.

3.6 Winding design

All of the three motors selected after the preliminary sizing have a double-layer fractional-slot winding. Their number of slots per pole and per phase results: $q_s = Q_s/(3 \cdot 2p) = 1.5$. So the star of slot is the same for the three chosen windings, that have only a different periodicity. The star of slot is shown in Figure 3.13.

The same coil span of 4 slots has been chosen too, so that from an electrical point of view the three windings outcome equal, i.e. they have the same fundamental winding coefficient k_w and they generate the same harmonic content in the *emf* and in the *mmf*. Indeed they have a different slot mechanical angle α_s^m but the same slot electrical angle α_s^e, according to the following definitions:

$$\alpha_s^m = \frac{360}{Q_s}\,[^\circ]$$

$$\alpha_s^e = p\frac{360}{Q_s} = 40\,[^\circ]$$

Then the distribution and pitch factors have been obtained as:

$$k_d = \frac{sin\left(q_s \frac{\alpha_s^e}{2}\right)}{q_s \frac{\alpha^e_{s\,[rad]}}{2}} = 0.955$$

$$k_p = cos\left(\frac{\beta_p^e}{2}\right) = 0.985$$

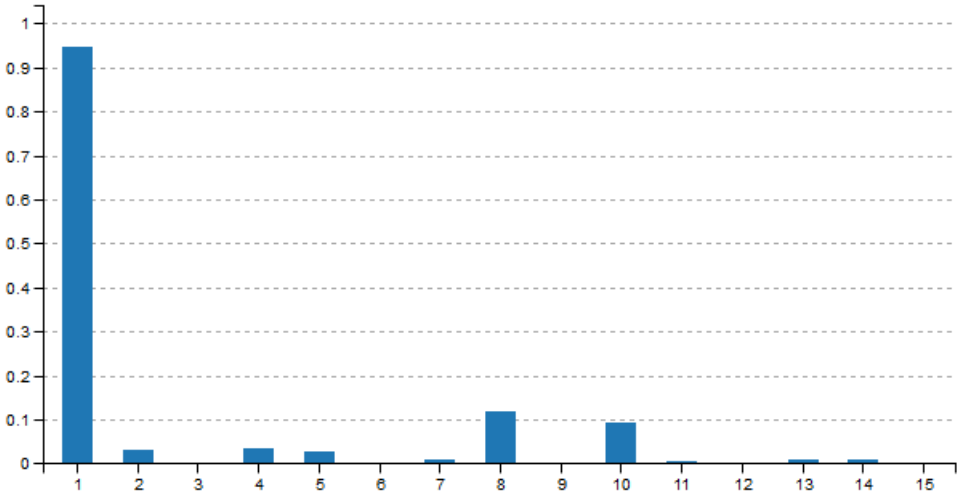

Figure 3.14: MMF harmonic spectrum.

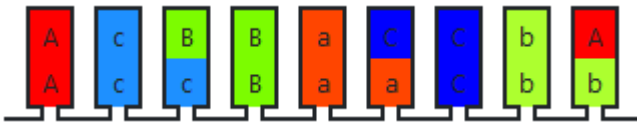

Figure 3.15: Windings layout under a pole pair.

Where β_p^e is the shortening electrical angle, that is half of the slot electrical angle due to the chosen coil span:

$$\beta_p^e = \frac{\alpha_s^e}{2} = 20\,[^\circ]$$

Fractional-slot windings are always short-pitched with a consequent improvement of the sinusoidal waveforms of the back *emf*. Finally the fundamental winding coefficient is defined as:

$$k_w = k_d k_p = 0.94$$

Fractional-slot windings has the advantages to yield to lower cogging torque and lower on-load torque ripple, as compared to machines with integer-slot windings at equal rated specifications. On the other hand, a balanced three-phase current flowing in an integer-slot winding produces a *mmf* with only odd harmonics not multiple of three, while the spectrum of the three-phase *mmf* generated by a fractional-slot winding could exhibits also unwanted even harmonics when some particular combinations of Q_s and p are made, as it happens for all the three selected machines. The harmonic content of the three-phase *mmf* has been computed with the open source software DOLOMITES and it is reported in Figure 3.14, while the actual layout of the windings under a pole pair is outlined in Figure 3.15. The complete schema for each motor can be obtained by repeating the sequence of Figure 3.15 a number of times equal to the periodicity of the winding, i.e. 5 for the 10 pole machine, 4 for the 8 pole winding, 3 for the 6 pole one.

3.6.1 Voltage specifications and number of turns choice

In each winding the maximum feasible number of parallel connections n_{pp} has been adopted. The parallel connections are made between coils under subsequent pole pairs, so that the maximum feasible n_{pp} basically corresponds to the periodicity of the winding. The implementation of parallel connections allows to use conductors with a smaller section at equal current specifications. Despite the copper weight does not change, as the conductor size lowers but the number of actual turns in slots increases proportionally, the coils become easier to wind up and the slot openings needed to insert the conductors can be reduced, with a consequent benefit in

the decrease of the magnetic reluctance of the air gap.

However, in the design and analysis of electrical machines it is more handy to refer to the equivalent series winding, which is the winding that generates the same *mmf* and the same *emf* without parallel connections, i.e. with all the coils in series. The number of series equivalent turns per phase N_s depends on the speed that has to be achieved, i.e. on the feeding frequency, and on the wanted back *emf* amplitude at such speed. SPM machines are designed looking at the base point specifications. The reference speed is the base speed, which should correspond to the rated speed n_R, because these motors commonly are always driven in MTPA region. Thus the rated frequency f_R is taken as reference frequency and the back *emf* should be the one produced at rated load $\hat{E}_R$. But, if the machine is not so saturated at rated load, as it should be expected, the back *emf* is quite similar to the *emf* generated in unload condition $\hat{E}_0$. Hence it can be assumed that $\hat{E}_r \cong \hat{E}_0$. Then, supposing a sinusoidal waveform for the *emf*, the number of equivalent series turns per phase can be computed as follows:

$$N_s = \frac{\sqrt{2}E_0}{\pi k_w \Phi_{pR}^{(1)} f_R} \tag{3.18}$$

Where $E_0\,[V]$ is the rms value of the *emf* and $\Phi_{pR}^{(1)}\,[Wb]$ is the fundamental flux per pole at rated load, which has been obtained with the following relation:

$$\Phi_{pR}^{(1)} = \hat{B}_{gR}^{(1)} \frac{D_s L_{stk}}{p} \tag{3.19}$$

The *emf* rms value is related to the machine voltage. Thus some voltage specifications must be chosen. A DC bus voltage of $V_{dc} = 700\,[V]$ has been assumed. Such value can be achieved by arranging the battery pack with strings of 200 series-connected $3.5\,V$ lithium-ion cells. Assuming that the three-phase inverter synthesizes the sinusoidal waveforms through the SVM (*Space Vector Modulation*) technique, the DC bus voltage is the peak value of the maximum sinusoidal line-to-line voltage obtainable. The motor phases are star-connected without neutral wire to avoid the flow of zero-sequence current. So, the rms value of maximum sinusoidal winding voltage $V_{wind_{MAX}}$ has been derived as follows:

$$V_{wind_{MAX}} = \frac{V_{dc}}{\sqrt{2}\sqrt{3}} = \frac{V_{dc}}{\sqrt{6}} \cong 285\,[V]$$

A margin of $5\,[V]$ has been taken in favor of the control system to consider variation in the DC bus voltage: $V_{wind_{MAX}} = 280\,[V]$. Then, to obtain the *emf* rms value a 5% voltage drop has been supposed due to the winding impedance:

$$E_0 = V_{wind}(1 - 0.05)$$

For the design purposes, the rated winding voltage V_{wind} has been set quite below the maximum value to prevent the inverter to work in overmodulation in overload condition, when a higher voltage drop is expected due to the higher feeding current: $V_{wind} = 204\,[V]$ for the 10 and 8 pole motors and $V_{wind} = 214\,[V]$ for the 6 pole machine.

After that N_s was computed with Equation 3.18, the number of in-slot series equivalent conductors n_{cs} and the number of actual in-slot conductors n_c has been obtained as follows:

$$n_{cs} = \frac{3N_s}{Q_s}$$

$$n_c = n_{cs} n_{pp} = \frac{3N_s}{Q_s} n_{pp}$$

n_c must be an even integer to allow the realization of a symmetric double-layer winding. If this not happens, n_c must be approximate to a close even integer. As a consequence N_s and n_{cs} need to be recomputed through the previous relations as well as the fundamental flux per pole, by inverting Equation 3.18. Then, if needed, some quantities among the stack length L_{stk},

the magnetic rated load $\hat{B}_{gR}^{(1)}$ and inner stator diameter D_s must be also adjusted according to Equation 3.19. In this project slight modifications of the stack length has been chosen to gain on torque capability.

The quantities presented in this section are summarized in Table 3.5 for each motor with all the other winding parameters and relevant sizes. It can be seen that the stack lengths have been slightly increase if compared to the ones in Table 2.4.

3.6.2 Current specification and conductor sizing

To choose a suitable conductor size the current specifications must be imposed. Indeed the conductor section $S_c\,[mm^2]$ is related to the rated current $I_R\,[A]$ and to the rated current density $J_R\,[A/mm^2]$ by the following equation.

$$S_c = \frac{S_{c_{eq}}}{n_{pp}} = \frac{I_R}{J_R n_{pp}} \tag{3.20}$$

Where $S_{c_{eq}}$ is the section of the equivalent series conductor.

The current density $J_R\,[A/mm^2]$ is imposed by the designer. Its choice is made by looking to similar machines and by experience. In particular it depends on the cooling system of the motor and on the thermal class of the adopted insulating materials. According to Equation 3.20, higher current density allow smaller conductor sizes at equal rated current. Thus the slots need less cross section area and the machine results more compact. But to achieve higher current density without compromising the in-slot insulation more complex cooling systems are needed because the specific losses increase a lot. In this project a H thermal class has been chosen for the insulation in order to withstand slot temperatures up to $180°C$ while the cooling system consists in a water-jacket with a circumferential duct. So, following the advice given in [33], the conductors have been sized for a current density $J_R = 9\,[A/mm^2]$.

The rated current instead depends on the chosen winding voltage. Indeed the motor behaves actually as an electric load powered by a current controlled voltage source, i.e. the battery pack and the inverter, although sometimes it could be useful to think the electric drive as a current source. So, assuming three-phase balanced sinusoidal feeding current and symmetric voltages, the power balance applied to the machine relates the rated current to the winding voltage as follows:

$$I_R = \frac{P_R}{3\cos\varphi_R \eta_R V_{wind}} \tag{3.21}$$

Where the fundamental power factor and the efficiency at rated load has been supposed as $\cos\varphi_R = 0.95$ and $\eta_R = 0.90$.

Finally, an effective commercial section close to the one computed with Equation 3.20 has been selected from commercial enameled copper wires. The actual current density has been recomputed inverting Equation 3.20 in the end.

The quantities presented in this section are summarized in Table 3.5 for each motor with all the other winding parameters and relevant sizes. In the table the maximum overload current is $I_{OL} = 4 \times I_R$.

3.7 Stator sizing

The next step in the electromagnetic design consists in deciding how to assembly and cut the stator laminations. Firstly the soft magnetic material type must be chosen. A good compromise between the specific losses ($p\,[W/kg]$) due to the hysteresis and the commercial availability is a M350 lamination. Then $0.5\,[mm]$ gauge electrical steel sheets are more than sufficient to limit the eddy current at the relatively low speed of the application under analysis. So a M350-50A lamination has been adopted for all of the three motors. The DC magnetization curve and the specific losses characteristic at $50\,[Hz]$ are reported respectively in Figures 3.16-3.17.

Parameter	**Symbol**	**Unit**	**Values**		
Number of poles	**2*p***	/	**6**	**8**	**10**
Number of slots	Q_s	/	27	36	45
Slot mechanical angle	α_s^m	[°]	13.3	10	8
Slot electrical angle	α_s^e	[°]	40	40	40
Winding factor	k_w	/	0.94	0.94	0.94
Slot pitch	p_s	$[mm]$	31.5	19.4	16.4
Pole pitch	τ_p	$[mm]$	141.9	87.2	73.8
Coil pitch	τ_p'	$[mm]$	126	77.6	65.6
Parallel connections	n_{pp}	/	3	4	5
Rated frequency	f_R	$[Hz]$	115	153	192
Winding voltage (rms)	V_{wind}	$[V]$	214	204	204
Rated current (rms)	I_R	$[A]$	53	55	55
Overload current (rms)	I_{OL}	$[A]$	212	220	220
Inner stator diameter	D_s	$[mm]$	271	222	235
Stack length	L_{stk}	$[mm]$	64	58	54
Series turns per phase	N_s	/	126	168	174
In-slot series conductors	n_{cs}	/	14	14	11.6
In-slot conductors	n_c	/	42	56	58
Conductor section	S_c	$[mm^2]$	2.011	1.539	1.227
Wire diameter	d_c	$[mm]$	1.60	1.40	1.25
Current density (rms)	J_R	$[A/mm^2]$	8.8	8.9	9.0

Table 3.5: Winding parameters and relevant quantities.

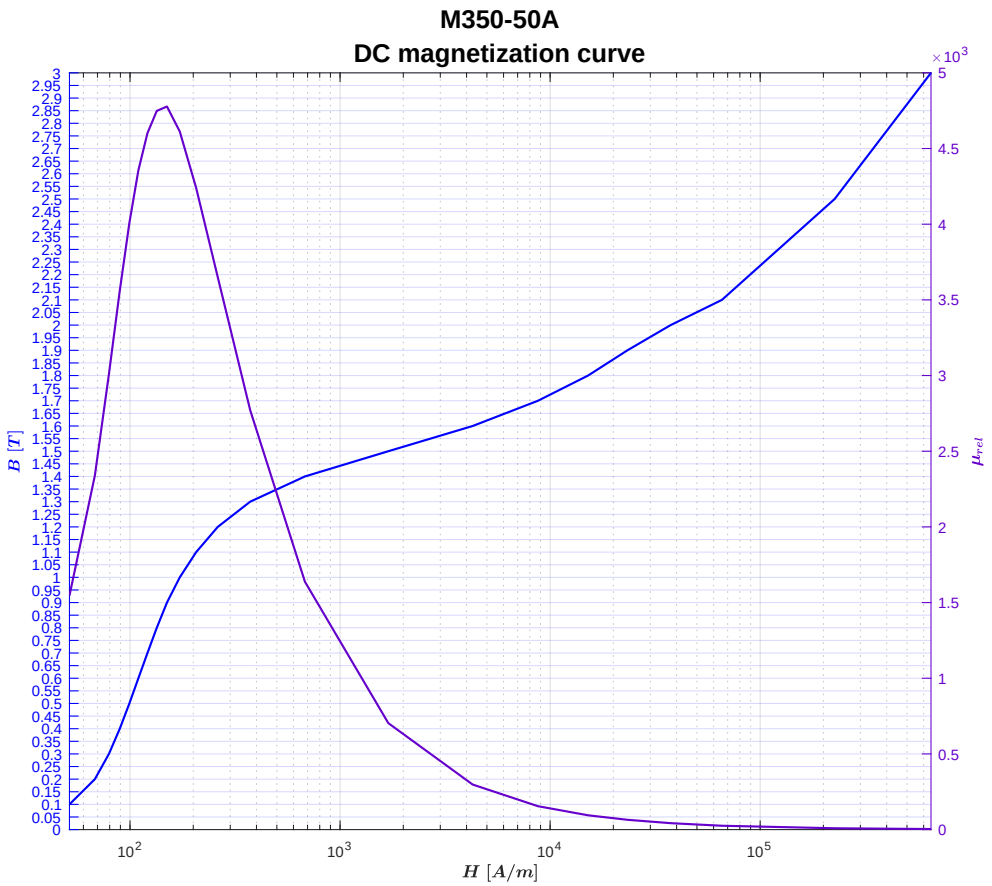

Figure 3.16: Lamination DC magnetization curve.

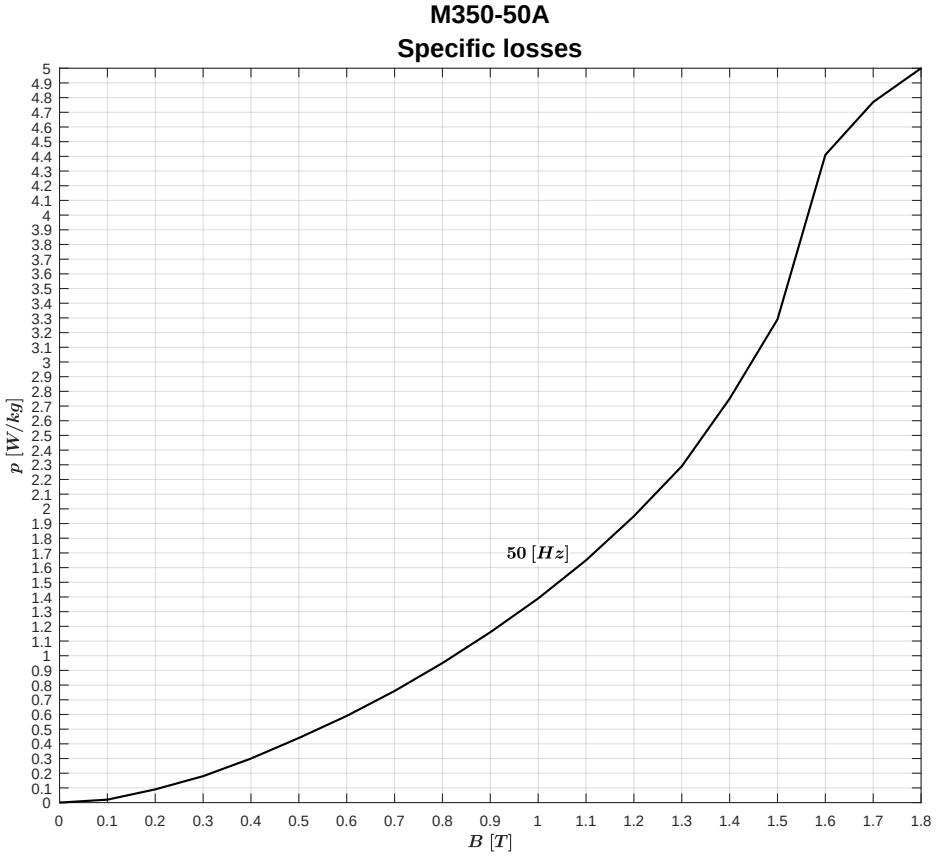

Figure 3.17: Lamination specific losses.

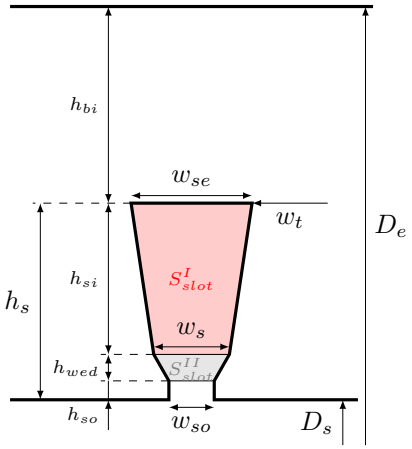

Figure 3.18: Slot geometry outline.

The actual axial length of the magnetic material $L_{fe}\,[mm]$ results a bit lower than the stack length due to the electrical insulation between the laminations:

$$L_{fe} = k_{pack} L_{stk}$$

The packing coefficient has been set to $k_{pack} = 0.96$ considering that the insulating purpose is obtained through the oxidation of the electrical steel sheets surfaces. Hence the number of laminations needed to assemble the stack can be easily found out as $N_{fe} = L_{fe}/0.5$. The laminations must be cut to realize the slots, the teeth and the back iron outline. The chosen geometry is drawn in Figure 3.18 with all the relevant dimensions, some of which have been linearized: it considers trapezoidal-shape slots and rectangular-shape teeth.

The first size to set is the tooth width w_t. To do so the wanted flux density in the tooth $\hat{B}_{tR}$ at rated load must be chosen. It is expected that the teeth will be the iron parts where the flux density will reach the higher value. So, the choice made for this project is $\hat{B}_{tR} = 1.6\,[T]$ for all of the three motors, in order to have a margin of $0.4\,[T]$ to the saturation value, which is about $2\,[T]$, considering that a large overload capability has to be fulfilled. Hence, supposing no flux leakages, the tooth width has been computed using the flux balance between the tooth and the air gap, namely the Gauss law for the magnetic field:

$$w_t = \frac{\hat{B}_{g_{MAX}} p_s}{\hat{B}_{tR} k_{pack}}$$

The maximum flux density value at the air gap $\hat{B}_{g_{MAX}}$ has been obtained as:

$$\hat{B}_{g_{MAX}} = \hat{B}_g + \Delta B_R$$

Where ΔB_R is the flux density variation due to the rated electric load calculated through Equation 3.14 or Equation 3.15. The sizing procedure continues with the definition of the slot geometry dimensions. The slot opening height h_{so} and the wedge height h_{wed} must be set by the designer. The choices made during this project are: $h_{so} = 0.6\,[mm]$ and $h_{wed} = 1\,[mm]$ for all of the three machines. The slot opening width $w_{so}\,[mm]$ is a designer choice too. A wise decision is a size double of the wire diameter $w_{so} = 2d_c$. In this way the insertion of the wires inside the slots becomes easier and consequently the winding manufacturing is simplified and speed up. At the same time the magnetic reluctance increase of the air gap is not so dramatic. At this point the width $w_s\,[mm]$ has been obtained as follows:

$$w_s = \frac{\pi(D_s + 2h_{so} + 2h_{wed})}{Q_s} - w_t$$

Then the slot cross section area $S_{slot}\,[mm^2]$ has been computed from the conductor effective section S_c considering a fill factor $k_{fill} = 0.4$:

$$S_{slot} = S^I_{slot} + S^{II}_{slot} = \frac{S_c n_c}{k_{fill}}$$

S_{slot} is made up by the section occupied by the wedge S^{II}_{slot} and the area earmarked to the conductors S^I_{slot}:

$$S_{slot} = S^I_{slot} + S^{II}_{slot}$$

The section $S^{II}_{slot}\,[mm^2]$ has been calculated as:

$$S^{II}_{slot} = \frac{w_s + w_{so}}{2} h_{wed}$$

So also the area $S^I_{slot}\,[mm^2]$ has been computed:

$$S^I_{slot} = S_{slot} - S^{II}_{slot}$$

Yet such area can be expressed as:

$$S^I_{slot} = \frac{w_s + w_{se}}{2} h_{si} \tag{3.22}$$

Where the width w_{se} can be further written as:

$$w_{se} = \frac{\pi(D_s + 2h_{so} + 2h_{wed} + 2h_{si})}{Q_s} - w_t \tag{3.23}$$

After some manipulations, the substitution of the previous 3.23 into the 3.22 yields to the following quadratic equation in the only unknown h_{si}:

$$\frac{\pi}{Q_s} h^2_{si} + \Big[\frac{w_{se}}{2} + \frac{\pi(D_s + 2h_{so} + 2h_{wed})}{2Q_s} - \frac{w_t}{2}\Big] h_{si} - S^I_{slot} = 0 \tag{3.24}$$

A feasible height $h_{si}\,[mm]$ has been selected solving the Equation 3.24. Finally the width $w_{se}\,[mm]$ has been computed through Equation 3.23 whereas the total height of the slot $h_s\,[mm]$ has been calculated as:

$$h_s = h_{so} + h_{wed} + h_{si}$$

h_s has been oversized a bit to consider the loss of slot area due to corners rounding. The last dimension that has to be find out is the back iron height $h_{bi}\,[mm]$. It is computed using the Gauss law in the same way of the tooth sizing. In this case the flux balance considers the flux in the air gap on the PM surface $\Phi_p\,[Wb]$ and the maximum flux in the back iron $\Phi_{bi}\,[Wb]$:

$$\Phi_{bi} = \frac{\Phi_p}{2} = \frac{1}{3}\hat{B}_g \frac{\pi D_s}{2p} L_{stk}$$

The flux density in the air gap $\hat{B}_g$ has been computed by inverting Equation 3.12, according to the hypothesis of a square-wave distribution. Then h_{bi} has been calculated as follows:

$$h_{bi} = \frac{\Phi_{bi}}{\hat{B}_{bi} L_{fe}}$$

Where the flux density maximum value in the back iron has been set to: $\hat{B}_{bi} = 1.3\,[T]$.

In the end the laminations outer diameter $D_e\,[mm]$ has been obtained as:

$$D_e = D_s + 2h_s + 2h_{bi}$$

The relevant geometric size and materials data are reported in Table 3.6 for all the three

Parameter	Symbol	Unit	Values		
Number of poles	**2p**	/	**6**	**8**	**10**
Inner stator diameter	D_s	$[mm]$	271	222	235
Stack length	L_{stk}	$[mm]$	64	58	54
Air gap thickness	g	$[mm]$	1	1	1
Permanent magnet			**N42 UH**		
PM covering angle	$2\alpha_m^m$	$[^\circ]$	20	30	24
PM thickness	t_m	$[mm]$	12	12	10
Laminations			**M350-50A**		
Laminations number	N_{fe}	/	123	112	104
Outer diamter	D_e	$[mm]$	394	330	332
Teeth width	w_t	$[mm]$	24.3	15.0	12.4
Slot height	h_s	$[mm]$	22.2	30.8	29.6
Slot ext. width	w_{se}	$[mm]$	12.4	9.8	8.2
Slot area	S_{slot}	$[mm^2]$	212	215	178
Wedge height	h_{wed}	$[mm]$	1	1	1
Opening height	h_{so}	$[mm]$	0.6	0.6	0.6
Opening width	w_{so}	$[mm]$	3.2	2.8	2.5

Table 3.6: Relevant geometric size and materials data.

machines.

3.8 Rotor and shaft sizing

For the purposes of the electromagnetic analysis the shaft could be neglected supposing that it should have a small diameter as compared to the rotor yoke or that it could be made by a ferromagnetic material. However, to present a more complete view of the project, a simplified but effective sizing of the shaft has been done. The shaft is very short ($L_{tot_{MAX}} = 190\,[mm]$) and the mechanical load are concentrated near the supports, i.e. the bearings in the front and rear plates. So any flexural strains can be neglected and only the torsional stress can be considered. The maximum torque that must be withstood is equal to the peak value of the mechanical characteristic of the original ICE, which is declared as $\mathcal{T}_{MAX} = 1350\,[Nm]$. Indeed the hybrid powertrain should exhibit the same performances of the traditional vehicle. So the shaft diameter results the same for all the three motors and it has been computed with the following relation.

$$D_{SHAFT} = \sqrt[3]{\frac{5\mathcal{T}_{MAX_{[Nmm]}}}{\tau_m}} \cong 60\,[mm]$$

Where the admissible mechanical strain has been set to $\tau_m = 35\,[N/mm^2]$ considering a solid C40 stainless steel shaft connected to a 6-cylinder 4-stroke Diesel engine.

The rotor yoke is laminated in the same way of the stator in order to limit the eddy current during the electromagnetic transients. The chosen electrical steel is also the same used for the stator: M350-50A. Yet in the rotor yoke it has been decided to shear off some triangular-shaped holes, centered below each magnet. The holes shape has been designed to not obstruct the magnetic flux generated by the PMs. Such choice has three advantages.

1. The weight and the inertia of the rotor decrease with a further improvement of the electromechanical responsiveness of the machine and a lightening of the mechanical load on the bearings. Moreover it is important to remind that the EM behaves as a mechanical load for the ICE even when it does not work. So a reduced inertia improve the kinematics

	J_r $[kg\ m^2]$		
2p	**6**	**8**	**10**
Without holes	0.230	0.096	0.111
With holes	0.182	0.072	0.085

Table 3.7: Rotor inertia.

of the entire powertrain too.

The inertia $J_r\,[kg\,m^2]$ can be expressed as a mass integral or with a corresponding volume integral:

$$J_r = \int_M r^2 dm = \int_M (x^2 + y^2) dm = \int_{Vol} (x^2 + y^2)\gamma dv \tag{3.25}$$

Where $\gamma\,[kg/m^3]$ is the density of the material and $r = \sqrt{x^2 + y^2}$ is the element distance from the rotation axis. In the machines rotor three materials contributes to the inertia: the iron ($\gamma_{fe} = 7800\,kg/m^3$), the PMs ($\gamma_{pm} = 7500\,kg/m^3$) and the magnets fiberglass bandage ($\gamma_{band} = 1800\,kg/m^3$). So Equation 3.25 becomes:

$$J_r = \gamma_{fe} \int_{Vol_{fe}} (x_{fe}^2 + y_{fe}^2) dv + \gamma_{pm} \int_{Volpm} (x_{pm}^2 + y_{pm}^2) dv + \gamma_{band} \int_{Vol_{band}} (x_{band}^2 + y_{band}^2) dv$$

The volume integrals have been automatically computed with FEMM. Table 3.7 reports the rotor inertia of the three motors with and without holes. It can be seen that the introduction of holes decreases the inertia of about $20 \div 25\%$

2. The particular triangular shape produces high flux density regions near the magnets, thus it opposes variation of flux in the PMs and consequently it helps in reducing the eddy current losses, as explained in [39].

3. Despite the machines are not equipped with a fan and they have a horizontal shaft, the holes provide additional cooling inside the rotor yoke through free convection because the laminations stacks are very short and the vortexes generated near the rotating surfaces can expand inside the air ducts.

The technical drawings of the three sized motors are reported in Appendix 5.3.

3.9 Volume limits fulfillment and materials cost computation

At this point the electromechanical structure of the three motors is completely defined. So it can be verified how well the volume constrains are fulfilled, according to the statements made during the preliminary sizing (Section 3.5). As far as the radial dimension limit concerns, looking at Table 3.6, the 8 and 10 pole machines have an external stator diameter quite below $400\,[mm]$, with a margin of about $70\,[mm]$ that is enough for the water-jacket thickness, whereas the 6 pole motor leaves only $6\,[mm]$ for the cooling duct and surely the total outer size will be a bit greater than the limit. Instead the total axial length L_{tot} can be estimated according to Figure 3.9. The dimensions δ_1, δ_3, d and the thickness of the front and rear plates δ_4 remain the same that have been chosen during the preliminary sizing. Thus only the length δ_2 has to be computed through Equation 3.7, where the coil span $\tau_p'\,[mm]$ of all the three machines is expressed as:

$$\tau_p' = 4 \cdot p_s$$

Then L_{tot} can be finally calculated with Equation 3.6. Table 3.8 reports the results and the chosen end-winding sizes for the three motors. It can be seen that the total axial length is lower than $190\,[mm]$. The available volume is wisely exploited and at the same time all the size

$2p$	/	6	8	10
D_e	$[mm]$	**394**	**330**	**332**
L_{stk}	$[mm]$	64	58	54
δ_1	$[mm]$	10	10	10
δ_3	$[mm]$	10	10	10
δ_4	$[mm]$	20	20	20
d	$[mm]$	10	10	10
p_s	$[mm]$	31.5	19.4	16.4
δ_2	$[mm]$	21	23.5	25.2
L_{tot}	$[mm]$	**186**	**185**	**184**

Table 3.8: Radial and axial sizes.

Material	$\gamma\ [Kg/m^3]$	$c\ [€/kg]$
Iron	7800	2
Copper	7900	7
NbFeB	7500	70

Table 3.9: Materials density and specific costs.

constrains are fulfilled. Thus the preliminary sizing method presented in Section 3.5 has been validated.

Furthermore a comparison between the material costs of the three motors has been done. To do so the volumes and weights of the various machines' parts have been estimated with analytical expressions or computed through the software FEMM. The materials density $\gamma\ [kg/m^3]$ and specific costs $[€/kg]$ used for the computations are reported in Table 3.9, where *'iron'* means electrical steel laminations. Slots and winding insulation as well as the PMs fiberglass bandage are neglected.

The iron total volume Vol_{fe}, and so the iron total weight G_{fe}, has been divided into three components:

$$Vol_{fe} = Vol_{fe_t} + Vol_{fe_{bi}} + Vol_{fe_{rot}}$$
$$G_{fe} = G_{fe_t} + G_{fe_{bi}} + G_{fe_{rot}}$$

The three contributions have been obtained as follows:

- Stator teeth:
$$G_{fe_t} = \gamma_{fe} Vol_{fe_t} = \gamma_{fe} Q_s h_s w_t L_{fe}$$
- Stator back iron:
$$G_{fe_{bi}} = \gamma_{fe} Vol_{fe_{bi}} = \gamma_{fe} \pi (D_e - h_{bi}) h_{bi} L_{fe}$$
Where the back iron height can be calculated as
$$h_{bi} = \frac{D_e - (D_s + 2h_s)}{2}$$
- Rotor yoke $G_{fe_{rot}} = \gamma_{fe} Vol_{fe_{rot}}$: the volume has been computed with the FEMM because of the triangular-shape holes. The results have been adjusted with the stacking coefficient $k_{pack} = 0.96$ to consider the insulation between the iron sheets.

The magnets weight $G_{pm} = \gamma_{pm} Vol_{pm}$ has been obtained using the volumes calculated through Equation 3.17 whereas the copper weight has been estimated only analytically with the following expression:

$$G_{Cu} = \gamma_{Cu} Vol_{Cu} = \gamma_{Cu} Q_s n_c S_c l_c$$

Table 3.10: Materials volumes, weights and costs.

2p	/	**6**	**8**	**10**
Vol_{fe_t}	$[dm^3]$	0.89	0.93	0.86
$Vol_{fe_{bi}}$	$[dm^3]$	2.70	1.20	0.96
$Vol_{fe_{rot}}$	$[dm^3]$	1.70	0.96	1.00
Vol_{fe}	$[dm^3]$	5.30	3.10	2.80
G_{fe_t}	$[kg]$	7	7.2	6.7
$G_{fe_{bi}}$	$[kg]$	21	9.7	7.5
$G_{fe_{rot}}$	$[kg]$	13	7.5	7.8
G_{fe}	$[kg]$	41	24.4	22
Iron cost	€	82	48.8	44
Vol_{pm}	$[dm^3]$	0.40	0.30	0.25
G_{pm}	$[kg]$	3.0	2.3	1.9
PMs cost	€	210	161	133
Vol_{Cu}	$[dm^3]$	0.50	0.54	0.52
G_{Cu}	$[kg]$	4.0	4.3	4.1
Copper cost	€	28	30	28.7
Overral cost	€	320	240	206

The half turn length l_c has been computed as follows:

$$l_c = L_{stk} + l_{ew}$$

Where l_{ew} is the length of the end-turns, which can be calculated according to Figure 3.9:

$$l_{ew} = 2\delta_1 + \frac{2\delta_2}{\sin \alpha_{ew}}$$

The outcomes are reported in Table 3.10. The 10 pole machine is the cheapest one and, at a first glance, it may seem the most worthwhile too. But, considering the costs and the performances of the entire electric drive, the things could change. Indeed the 10 and 8 pole motors require higher current and feeding frequency, so that the inverter power switches and the battery pack must withstand more trying working conditions. Efficiency is also a key point for the application under analysis. Therefore a proper comparison between the three designed machines can be done only after a detailed performances and losses analysis. Moreover the cooling system and the thermal behavior should be taken into account too.

Chapter 4

Electromagnetic analysis

In this chapter the electromagnetic analysis of the three designed machines will be presented.

The three EMs have been studied using both analytical relations and finite element analysis (FEA) in order to assess the machine performances and validate the hypothesis made during the sizing process. The machines electromagnetic behavior in unload condition, with the rated current value and with the maximum overload current value, has been analyzed and simulated through magnetostatic FEA. The significant parameters of the machines have been computed too. FEMM and MATLAB® softwares have been used for this purpose. The results of such analysis will be presented and exhaustively discussed so that some relevant comparisons between the computations and the differences with the initial suppositions will arise. The performances between the three designed EMs will also be compared. Finally the machine losses are mapped over the admissible working points in order to provide the necessary information to do a proper thermal design and to analyze the powertrain efficiency.

4.1 Performances analysis in unload condition

The flux linkage and the *emf* generated by the machines while they are rotating with open circuit, i.e. with no feeding current, can be estimated considering the magnetic circuit shown in Figure 4.1 [24].

It is supposed that the *mmf* ($[Aturns]$) produced by the magnet pushes the magnetic flux through three reluctance: the air gap, the tooth and the back iron. The path in the rotor yoke is neglected supposing that its reluctance is much lower if compared to the tooth or the back iron. A further analysis with finite elements will shown that such hypothesis could not be done for these machines, because of the particular geometry of their magnetic circuits. The PM is represented as flux source with a parallel reluctance, which depends on the magnet thickness and differential permeability. So the *mmf* drop on the magnetic reluctances must be balanced entirely by the magnet (there are no feeding current).

The flux density in the air gap $\hat{B}_{g0}$, which corresponds to the flux density value of the PM's working point B_m, has been computed using Equation 3.10. The magnetic equivalent air gap g^{II} is defined as:

$$g^{II} = k_{sat0} g^{I} = k_{sat0} k_{carter} g$$

The saturation coefficient in unload condition k_{sat0} must be supposed. At the end of the magnetic circuit computations the value of k_{sat0} will be verified: if it will be too far from the supposed one the circuit must be solved again trying a different coefficient. Thus, such analytical method consists in an iterative procedure, which has been implemented in a MATLAB® script. The Carter coefficient k_{carter}, that takes into account the reluctance increase due to slots openings, has been estimated with the following simplified expression:

$$k_{carter} = \frac{p_s}{p_s + g - 0.75 \cdot w_{so}}$$

Then the magnetic field value of the PM's working point in unload condition can be also

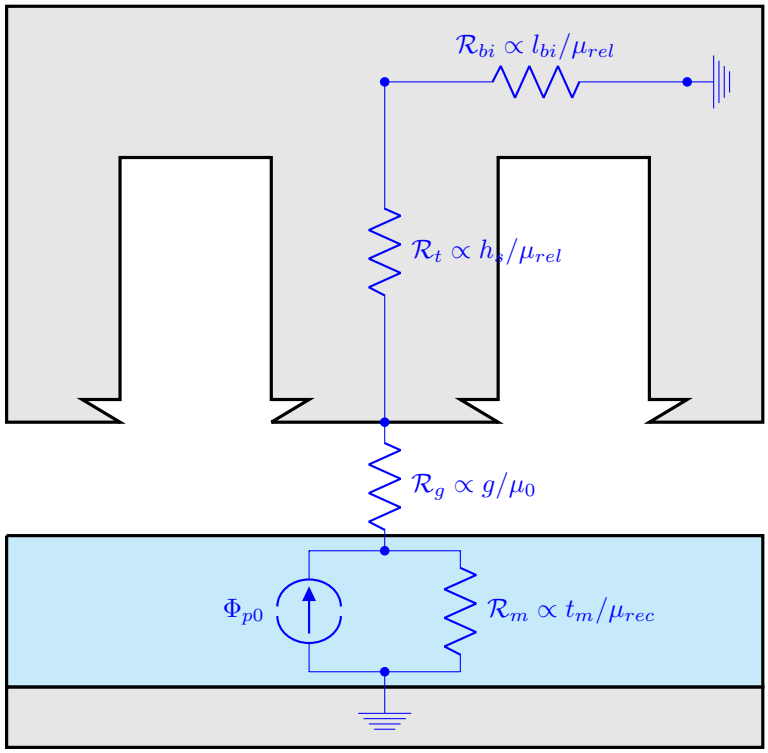

Figure 4.1: Magnetic circuit.

calculated as:

$$H_{m0} = \frac{B_m - B_{rem}}{\mu_{rec}\mu_0}$$

While the magnetic flux under a pole pitch can be estimated as:

$$\Phi_{p0} = \frac{2}{3}\hat{B}_{g0}\frac{\pi D_s}{2p}L_{stk}$$

Considering that the PM cover 2/3 of the pole pitch.

From the flux density value $\hat{B}_{g0}$ the *mmf* drop in the air gap has been computed as follows:

$$\hat{H}_{g0}g^I = \frac{\hat{B}_{g0}}{\mu_0}gk_{carter}$$

Then, from the magnetic flux balance between the air gap and the tooth (Gauss law), the flux density in the tooth has been obtained:

$$\hat{B}_{t0} = \frac{\hat{B}_{g0}p_s}{w_t k_{pack}}$$

So, the corresponding value of magnetic field $\hat{H}_{t0}$ has been found out with the help of the lamination DC magnetization curve in Figure 3.16. As a consequence the *mmf* drop along the tooth can be computed: $\hat{H}_{t0}h_s$.

It can be supposed that the magnetic flux in the air gap slits in half when it reaches the back iron, so that the maximum flux in the back iron is half the flux in the air gap: $\Phi_{bi} = \Phi_{p0}/2$. Thus the maximum flux density in the back iron has been obtained as:

$$\hat{B}_{bi} = \frac{\Phi_{bi}}{h_{bi}L_{fe}}$$

The flux density is not constant along the back iron because each tooth adds up its flux contribution. So a detailed computation would be done by dividing the path in segments. However a fast estimation based on similar machines can be done. The mean flux density in the back iron has been estimate from the maximum value:

$$\hat{B}^*_{bi} = 0.90 \cdot \hat{B}_{bi}$$

Then the corresponding magnetic field value $\hat{H}^*_{bi}$ has been found out using the lamination BH curve and the *mmf* drop on the back iron ha been calculated as: $\hat{H}^*_{bi} l_{bi}$, where the back iron length under a pole has been computed as follows:

$$l_{bi} = \frac{\pi(D_e - h_{bi})}{2 \cdot 2p}$$

In the end the actual saturation coefficient has been obtained using its definition:

$$k_{sat0} = \frac{\sum \hat{H} l}{\hat{H}_{g0} g^I} = \frac{\hat{H}_{g0} g^I + \hat{H}_t h_s + \hat{H}^*_{bi} l_{bi}}{\hat{H}_{g0} g^I}$$

After that k_{sat0} outcomes different no more than $2 \div 5\%$ of the value supposed at the beginning of the procedure, the flux linkage and the *emf* generated by the PM can be computed. At first the fundamental flux density at the air gap, namely the peak of the first harmonic, have been obtained as in Equation 3.12, supposing a square-wave distribution and considering that the PM covers 120 electrical degrees. Then the corresponding fundamental flux has been computed as follows:

$$\Phi^{(1)}_{p0} = \hat{B}^{(1)}_{g0} \frac{D_s L_{stk}}{p}$$

Hence the peak value of the flux linkage $\hat{\Lambda}_0$ and the peak value of the *emf* $\hat{E}_0$ have been derived with the following expressions:

$$\hat{\Lambda}_0 = k_w \frac{N_s}{2} \Phi^{(1)}_{p0}$$

$$\hat{E}_0 = \omega \hat{\Lambda}_0 = 2\pi f \hat{\Lambda}$$

The analytical computations just presented have been compared with an unload magnetostatic FEA performed using the software FEMM for each motor. Only a pole pair has been analyzed for every machine, taking advantage of the periodic boundary conditions (BCs) provided by the software. Furthermore a sliding band has been set inside the air gap in order to simulate rotations without the need of remeshing for every rotor position. Indeed steady-state rotations have been also simulated with a series of magnetostatic FEA, changing the rotor position at each shot. The initial position $\theta_e = 0°$ is achieved when the magnetization direction, namely the d-axis, is aligned with the magnetic axis of the phase a [40].

The preprocessing and mesh layout of the 6 pole machine is reported in Figure 4.2 as example. Relatively coarse meshes have been adopted in order to reduce the computational cost without affect too much the precision. The 6 pole motor, which is the one that has required more mesh elements, has been discretized using a mesh with 7489 nodes. The permanent magnets properties has been set at the supposed working temperature of $120°C$, according to the parameters in Table 3.3, with a parallel magnetization.

The unload flux maps of the three machines are shown in Figures 4.3-4.4-4.5, while, as example, Figure 4.6 reports the 6 pole machine flux density distribution in the air gap with its harmonic content until the 11^{th} order. It can be seen that the square waveform of the flux density distribution is affected by the concentrated reluctances of the slot openings, thus the peak value of the first harmonic, i.e. the magnetic load, results actually a bit smaller than the expected one, which is the quantity obtained through Equation 3.12. Moreover from the flux maps it can be stated that all the three machines present flux density values in the iron paths lower than the ones analytically calculated with the magnetic circuit, but this not necessary means that the they are less saturated. Indeed the contribution of the rotor yoke cannot be

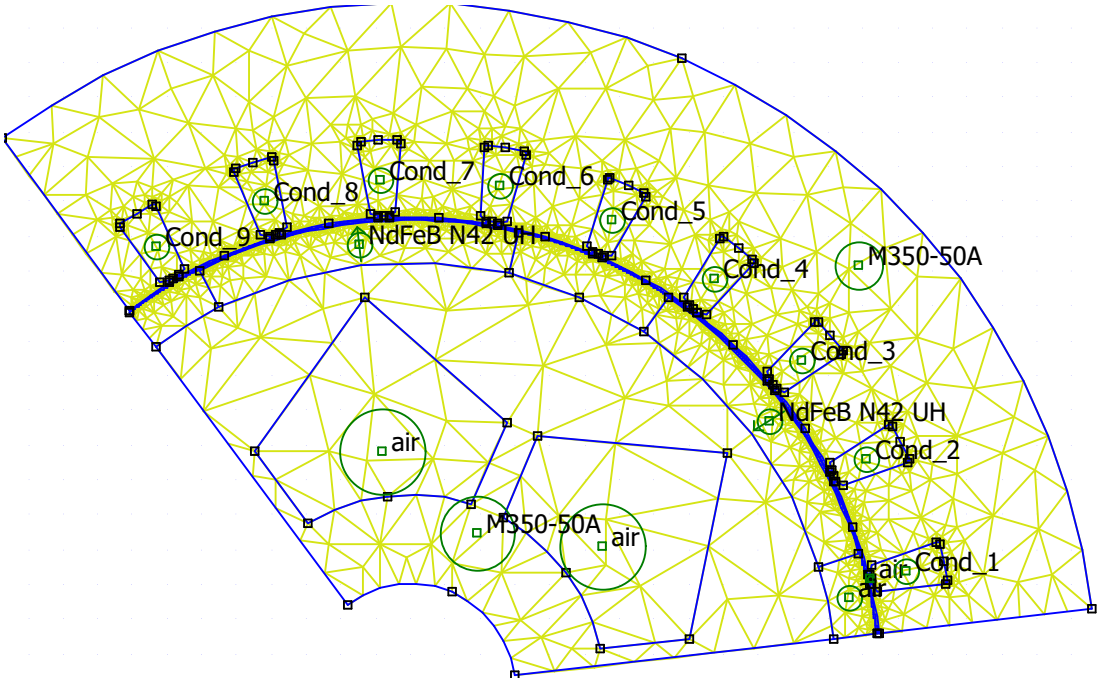

Figure 4.2: 6 poles machine: preprocessing settings and mesh.

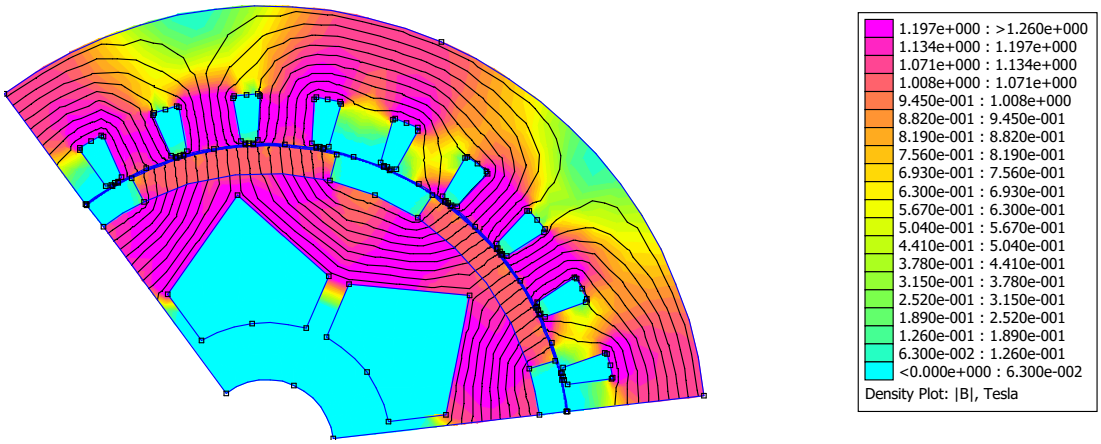

Figure 4.3: 6 pole machine: flux map in unload condition.

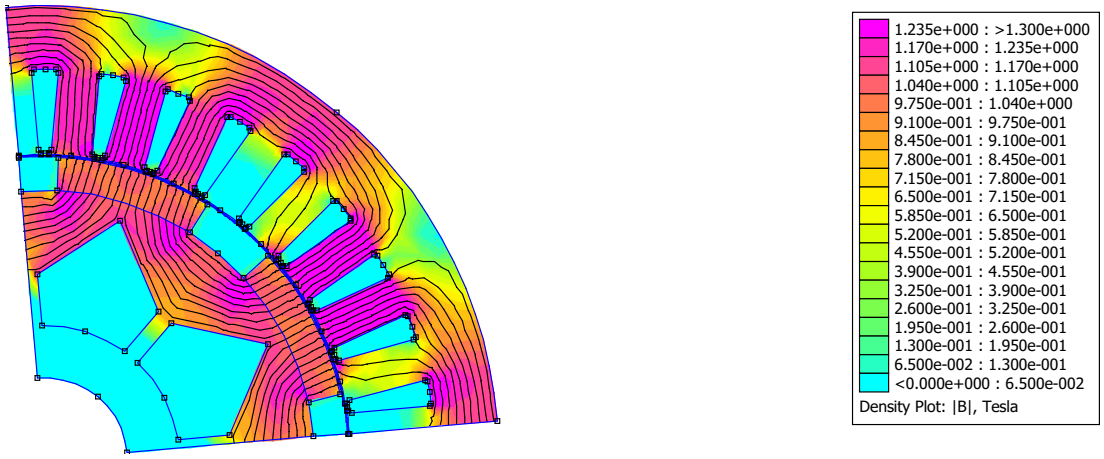

Figure 4.4: 8 pole machine: flux map in unload condition.

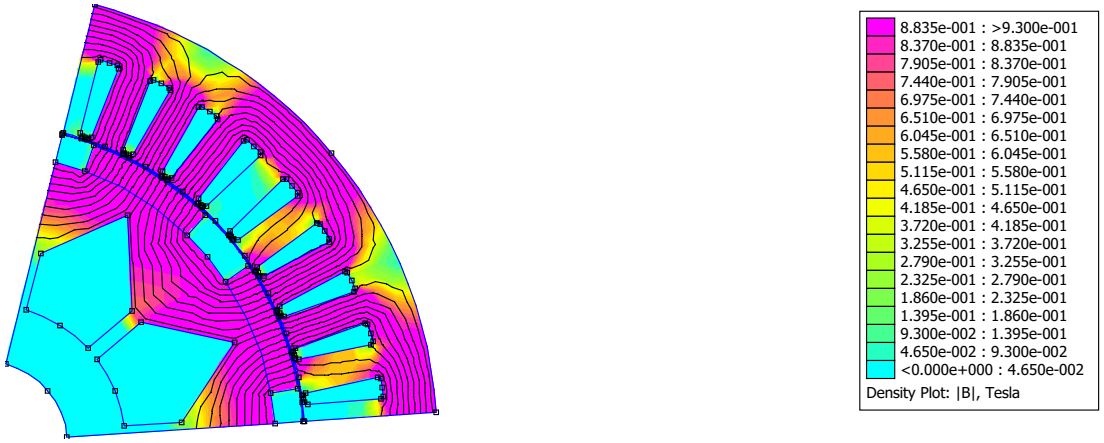

Figure 4.5: 10 pole machine: flux map in unload condition.

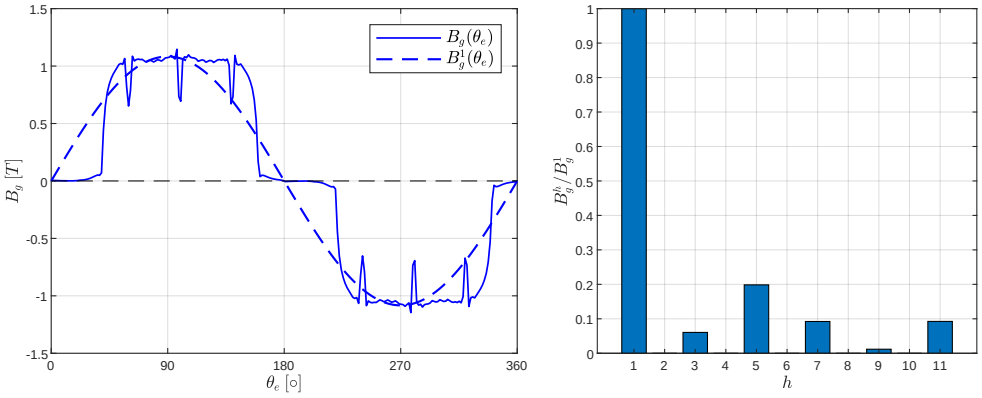

Figure 4.6: 6 pole machine: air gap flux density distribution in unload condition.

neglected because the triangular-shaped holes causes flux density values comparable with the ones in the tooth and in the back iron.

The *mmf* drops in each part of the magnetic circuit, rotor yoke included, have been computed with FEMM along the path of a magnetic flux line using the general definition of *mmf* drop:

$$\int_l \bar{H} \cdot \bar{t}\, dl$$

Also the magnetic flux under a pole pitch has been obtained from the post-processing interface of FEMM with the general definition of magnetic flux through a surface:

$$\Phi = \int_S \bar{B} \cdot \bar{n}\, dS$$

To derive the flux linkage and the *emf* an unload rotation has been simulated. At each rotor position the integral of the vector potential $\bar{A}$ over every slot cross section area has been collected. Then the flux linkage with the generic phase x ($x = a, b, c$) has been computed with the following relation:

$$\lambda_x = p n_{cs} k_x \frac{\bar{A}}{S_{slot}} L_{stk}$$

The expression is multiplied by p because only a pole pair has been analyzed. k_x is the row of the slot matrix corresponding to phase x. The slot matrix, which is the same for all the three motors, is reported below. It represents the winding layout shown in Figure 3.15.

Q_s	1	2	3	4	5	6	7	8	9
k_a	1	0	0	0	-1	-0.5	0	0	$+0.5$
k_b	0	0	$+0.5$	1	0	0	0	-1	-0.5
k_c	0	-1	-0.5	0	0	$+0.5$	1	0	0

The *emf* on phase the generic phase x is defined according to the Faraday-Neumann induction law:

$$e_x = -\frac{\partial \lambda_x}{\partial t} = -\omega \frac{\partial \lambda_x}{\partial \theta_e}$$

The continuum derivative could be easily discretize with its incremental ratio. But, from a computational point of view, this could be a risky operation. Indeed rapidly changing signals with a small incremental step can lead to wrong and noisy outcomes. So, the *emf* signals have been derived from the Fourier series of the flux linkage, whose coefficients have been computed through the FFT function (Fast Fourier Transform) already implemented in MATLAB®. As example, Figures 4.7-4.8 show the 6 pole machine flux linkage and *emfs*, with harmonic spectrum until the 11^{th} order. The results for all the three motors both from the analytical computations and the FEA are reported in Table 4.1.

It can be seen that the fractional slot winding layout produces even harmonics into the *emfs*. Nevertheless the sinusoidal waveforms of both the flux linkage and the *emfs* are satisfying. Furthermore there is a good match between the peak values computed with the analytical method and the FEA. On the contrary the *mmf* drops obtained with FEA outcomes differently distributed along the magnetic flux lines than what is expected from the analytical solution of the magnetic circuit. This is due to the non-negligible rotor yoke contribution. Moreover the flux per pole are also very far from the expected values, maybe because of the actual flux density distribution in the air gap. However the saturation coefficients results very similar, so, from the overall performances point of view, the analytic method can be considered satisfactory.

4.1.1 Cogging torque

In an unload rotation the machines do not develop any mean torque because no current flows into the winding. But variations of magnetic coenergy occur due to the reluctance changes close to the slot openings. Physically, the magnets are subjected to cogging. The resulting cogging torque has zero-mean because it is generated only by a coenergy variation [40]. Nevertheless it

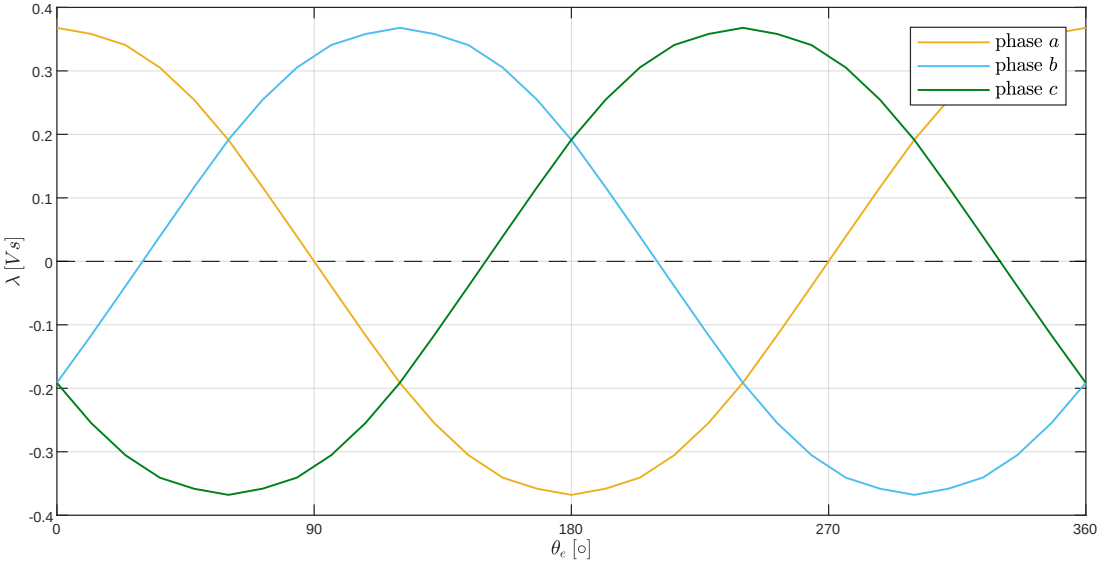

Figure 4.7: 6 poles machine: flux linkage in unload condition.

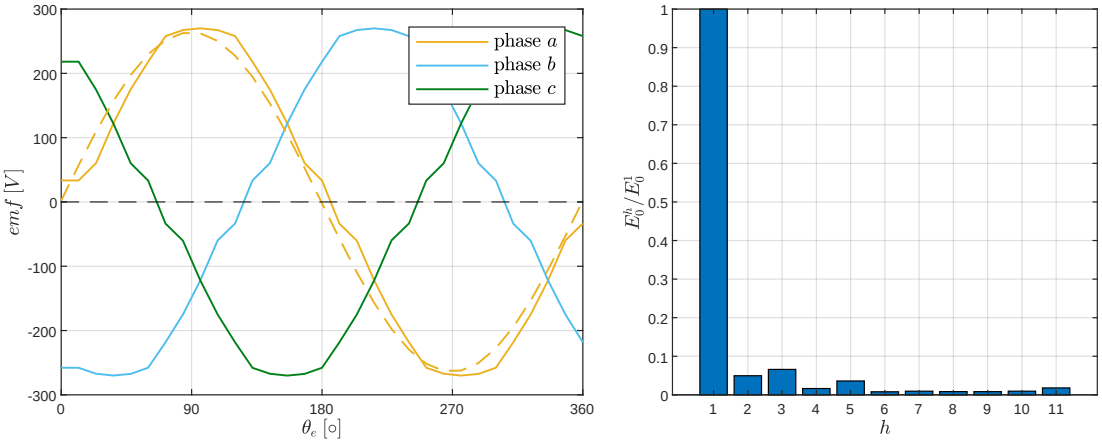

Figure 4.8: 6 poles machine: **emfs** in unload condition.

Table 4.1: Magnetic circuit analysis in unload condition

Quantity	**Symbol**	**Unit**	**6 poles**		**8 poles**		**10 poles**	
			Analytic	FEA	Analytic	FEA	Analytic	FEA
Air gap *mmf* drop	$\hat{H}_{g0}g^I$	$[Aturns]$	869	820	877	792	860	806
Tooth *mmf* drop	$\hat{H}_{t0}h_s$	$[Aturns]$	16	9	21	12	22	13
Back iron *mmf* drop	$\hat{H}^*_{bi}l_{bi}$	$[Aturns]$	22	15	17	10	17	9
Rotor yoke *mmf* drop	$\hat{H}_{r0}l_r$	$[Aturns]$	/	18	/	8	/	6
Saturation coeff.	k_{sat0}	$[/]$	1.04	1.05	1.04	1.04	1.04	1.03
Flux per pole	Φ_{p0}	$[mWb]$	6.3	5.9	3.5	3.3	2.7	2.2
Flux linkage peak	$\hat{\Lambda}_0$	$[Vs]$	0.39	0.37	0.29	0.27	0.23	0.22
Emf peak	$\hat{E}_0$	$[V]$	281	267	279	260	277	267

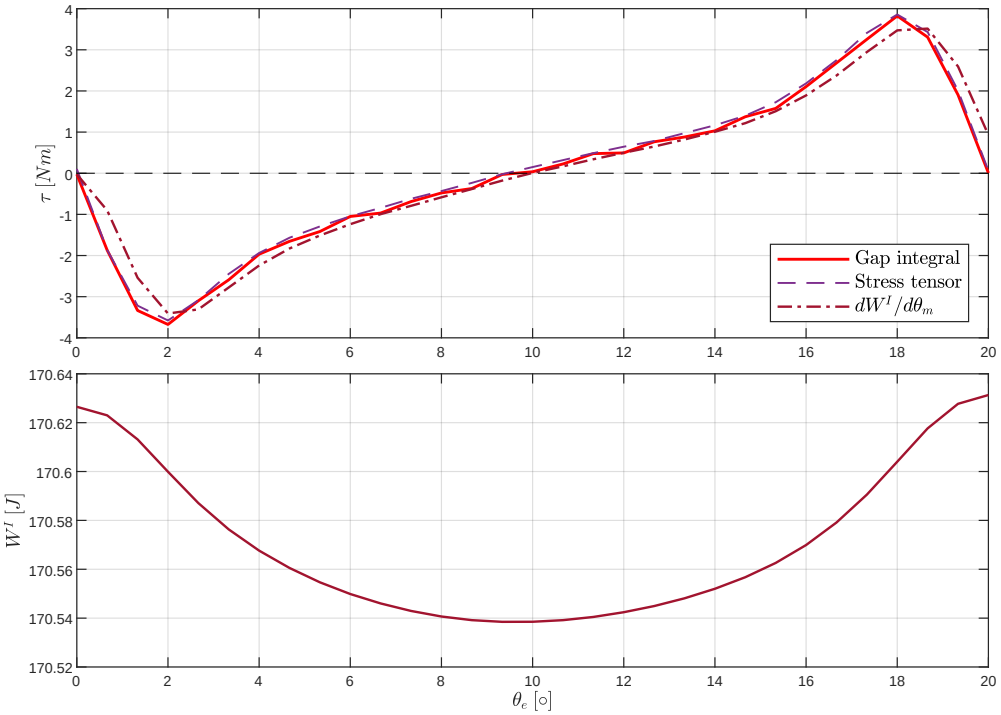

Figure 4.9: 6 pole motor: cogging torque.

is important that its amplitude remains contained, especially in the application under analysis, where the EM is always a mechanical load for an ICE and additional mechanical strains should be avoided to preserve the working life of all the powertrain components.

The trend of the cogging torque has been obtained for all the three designed motors with the software FEMM using three different methods.

1. Gap integral: the software computes the discretized integral formulation of Maxwell stress tensor considering the radial and tangential components of the magnetic fields and flux density vectors along a contour inside the sliding band in the air gap.

2. Weighted stress tensor: the software discretizes the Maxwell stress tensor as a weighted sum over the rotor volume considering the magnetic fields and the flux density vectors along some contours chosen by a particular algorithm implemented inside FEMM.

3. Coenergy variation: according to Equation 3.3, with no feeding current the electromagnetic torque can be computed by discretizing the derivative of the magnetic coenergy with its incremental ratio:

$$\tau_{cog} = \frac{\partial w^I}{\partial \theta} = \frac{\Delta W^I}{\Delta \theta}$$

The simulation of an entire electrical rotation is not needed because the period of the cogging torque Θ_{cog} is much smaller than 360 electrical degrees:

$$\Theta_{cog} = p\frac{360}{lcm(Q_s, 2p)} = 20^\circ$$

The results for the three machines are reported in Figures 4.9-4.10-4.11. It can be seen that the outcomes from method (1) and (2) are the same. So in the next torque computation only the Gap integral has been used. The amplitude of the cogging torque decreases with the increase of the number of poles. The 10 pole machine indeed presents the lower peak value. However for all the three motors the cogging remains under the 3% of the rated torque.

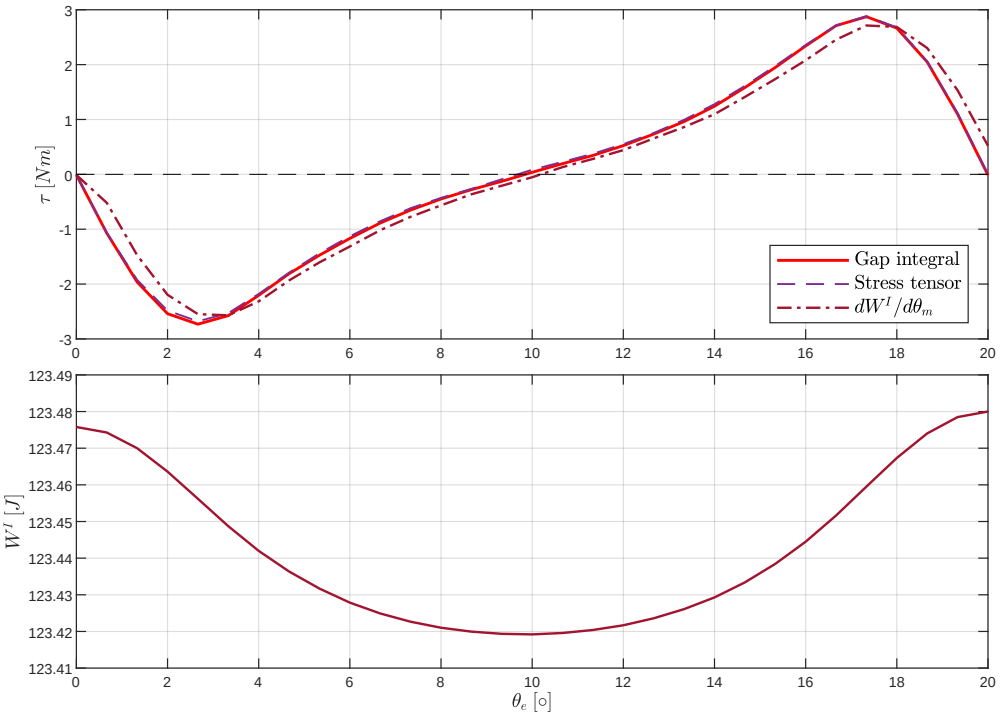

Figure 4.10: 8 pole motor: cogging torque.

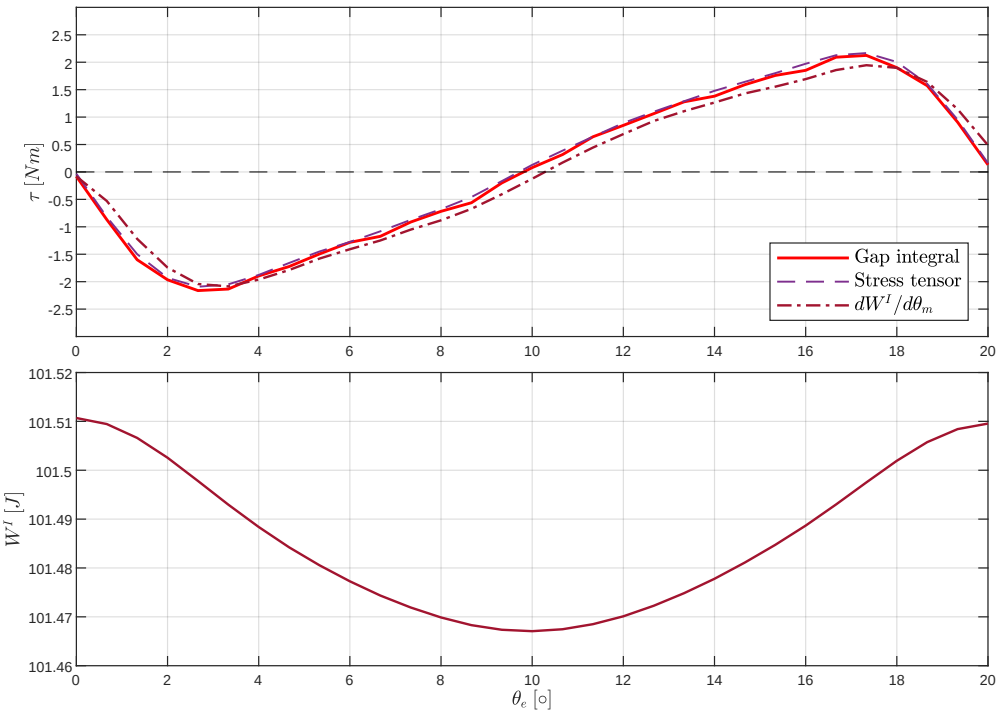

Figure 4.11: 10 pole motor: cogging torque.

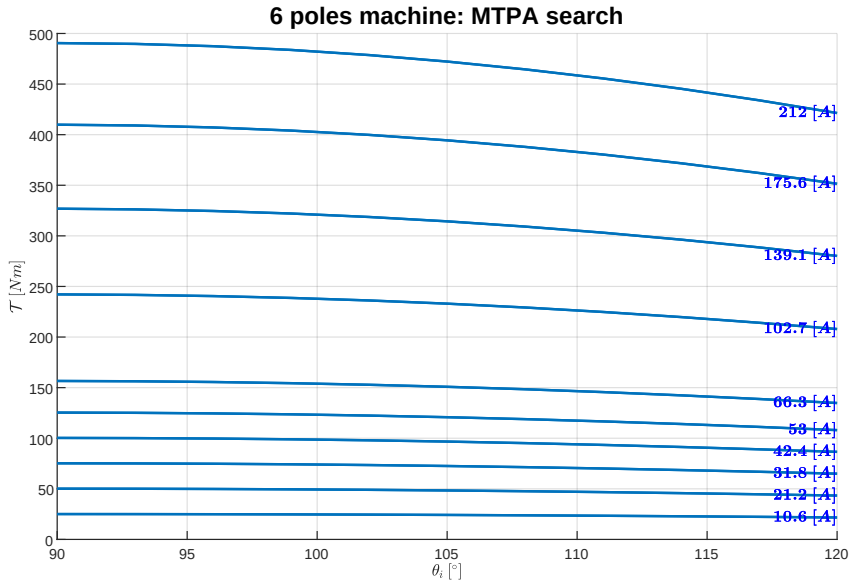

Figure 4.12: 6 pole motor: MTPA search.

4.2 MTPA search

A MTPA search has been done in order to asses properly the on-load torque performances and to provide a lookup table that can be useful to map the reference signals of the control system according to the required average torque. The analysis has been performed varying the current phase angle θ_i in the range $90° \div 120$ for many current amplitudes I $[A]$ until the maximum overload. For every trial the average electromagnetic torque has been computed as the mean of the Maxwell stress tensor, simulating a half electrical rotation. Indeed the torque has a periodicity of 180 electrical degrees. Such analysis is very time consuming and to do it the MATLAB® parallel computation toolbox has been used. The results are very similar between the three motors. As example, Figure 4.12 reports the outcomes of the 6 pole machine MTPA search. It can be seen that the maximum torque is obtained with a quadrature current for every rms value. Thus the statements presented in Section 3.2 have been verified. The MTPA condition is actually achieved by imposing three phase current with $\theta_i = 90°$ even at maximum overload. This means that the motors are never enough saturated to shift the MTPA region in the second quadrant of the $i_d - i_q$ plane.

4.3 Performances analysis at rated load and at maximum overload

The motors are always driven in MTPA condition, so the on-load performances have been assessed by imposing quadrature current: $i_d = 0$, $i_q = \sqrt{2}I_R$ for the rated load and $i_q = \sqrt{2}I_{OL}$ for the maximum overload. The flux maps of the three motors at rated load are shown in Figures 4.13-4.15-4.17, while the maximum overload conditions are reported in Figures 4.14-4.16-4.18. It can be seen the impact of the electric load, that slant the flux lines from the d axis towards the quadrature axis. Such phenomenon can be identified more clearly in the air gap flux density distribution, reported in Figures 4.19-4.20 for the 6 pole machine. The magnetic circuit has been analyzed in the same way adopted for the unload condition, except for the teeth, that now are magnetized differently due to the flux density distorsion. For brevity purpose the results are not reported. However the comments made for the unload condition are still valid.

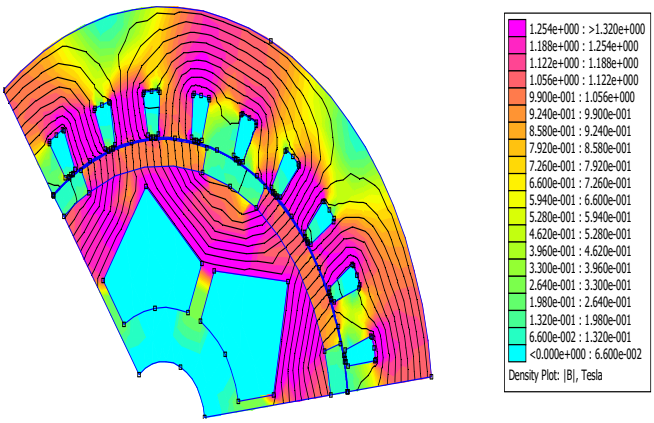

Figure 4.13: 6 pole motor: flux map on rated load.

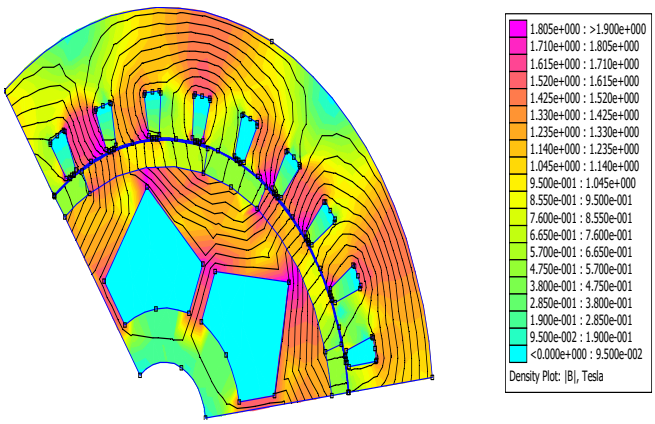

Figure 4.14: 6 pole motor: flux map on maximum overload.

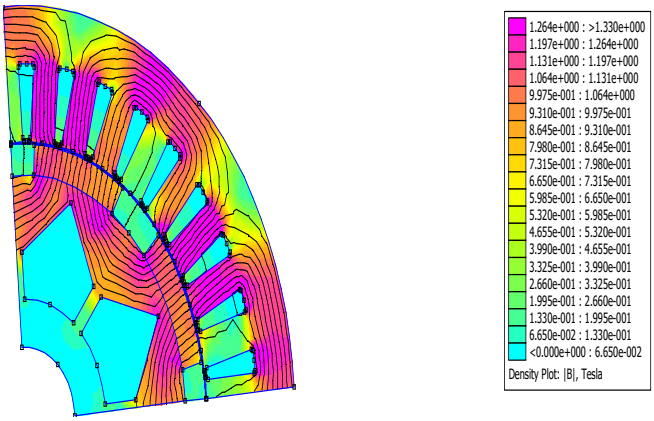

Figure 4.15: 8 pole motor: flux map on rated load.

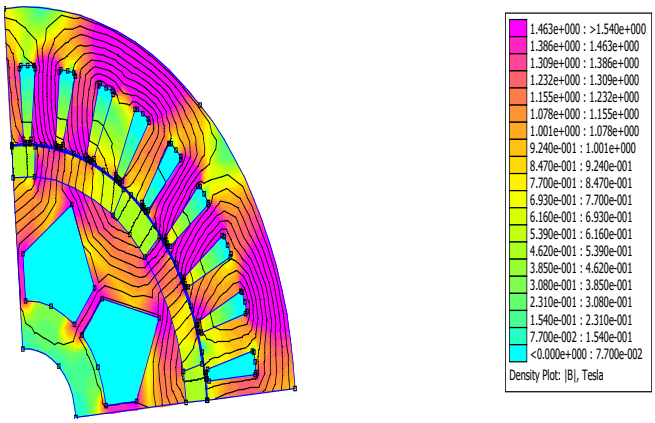

Figure 4.16: 8 pole motor: flux map on maximum overload.

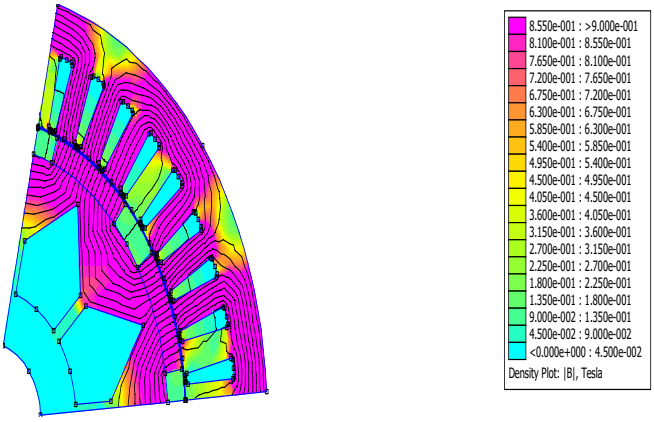

Figure 4.17: 10 pole motor: flux map on rated load.

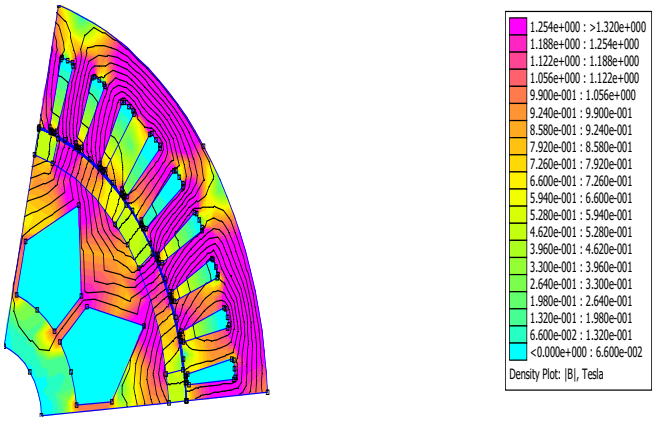

Figure 4.18: 10 pole motor: flux map on maximum overload.

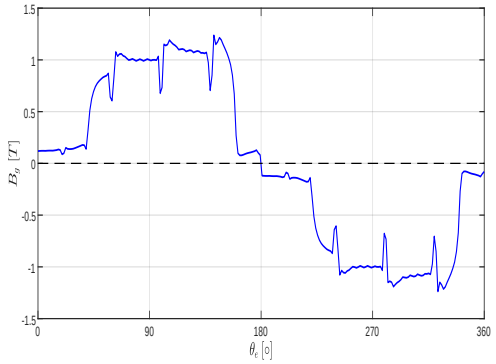

Figure 4.19: 6 pole motor: air gap flux density distribution in rated load.

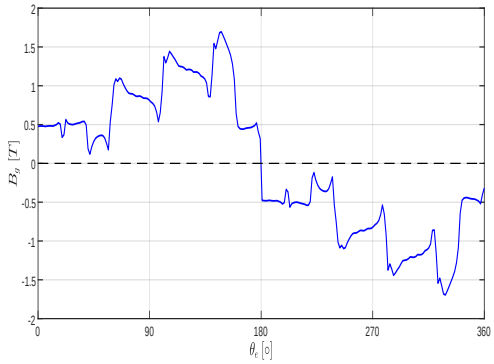

Figure 4.20: 6 pole motor: air gap flux density distribution in maximum overload.

Table 4.2: Rated load and maximum overload torque performances.

	$2p$	6	8	10
Rated load	$\mathcal{T}_R\ [Nm]$	126	127	130
	ripple [%]	12	8.0	7.5
Max. overload	$\mathcal{T}_{OL}\ [Nm]$	492	481	480
	ripple [%]	10	6.2	5.2

In the electromagnetic torque computation the ripple component due to the coenergy variation has been distinguished from the average value generated by $\Im[\check{\bar{\lambda}}\bar{i}]$. The results are reported in Figures 4.21-4.22-4.23 for the rated load and in Figures 4.24-4.25-4.26 for maximum overload. The performances of the three motors are summarized in Table 4.2. The specifications are entirely fulfilled and the ripples are admissible.

4.4 Demagnetization test

The behavior of the PMs against demagnetization has been assessed through a magnetostatic FEA in the most critical working condition, i.e. with a maximum overload direct-axis demagnetizing current: $i_d = -\sqrt{2}I_{OL}$, $i_q = 0$. Such situation should never happen during the normal operations, but it can occurs in the event of an inverter fault or a control system failure.

The magnetic fields and the flux density vectors in the PMs elements, which are referred to $x-y$ cartesian coordinates in the FEMM interface, have been projected onto the magnetization direction. Then the minimum values B_{min}, H_{min} have been compared with the *'knee'* point, whose parameters are taken from Table 3.3 for the N42 UH magnet at the supposed working temperature of 120°. The results are reported in Table 4.3. The PM does not demagnetize even in this extreme condition as its working point stays always above the *'knee'*.

Table 4.3: PM working point in the most critical demagnetizing condition.

$2p$	/	6	8	10
B_{knee}	$[T]$	-0.16	-0.16	-0.16
H_{knee}	$[kA/m]$	-895	-895	-895
B_{min}	$[T]$	-0.04	-0.04	+0.05
H_{min}	$[kA/m]$	-816	-814	-751

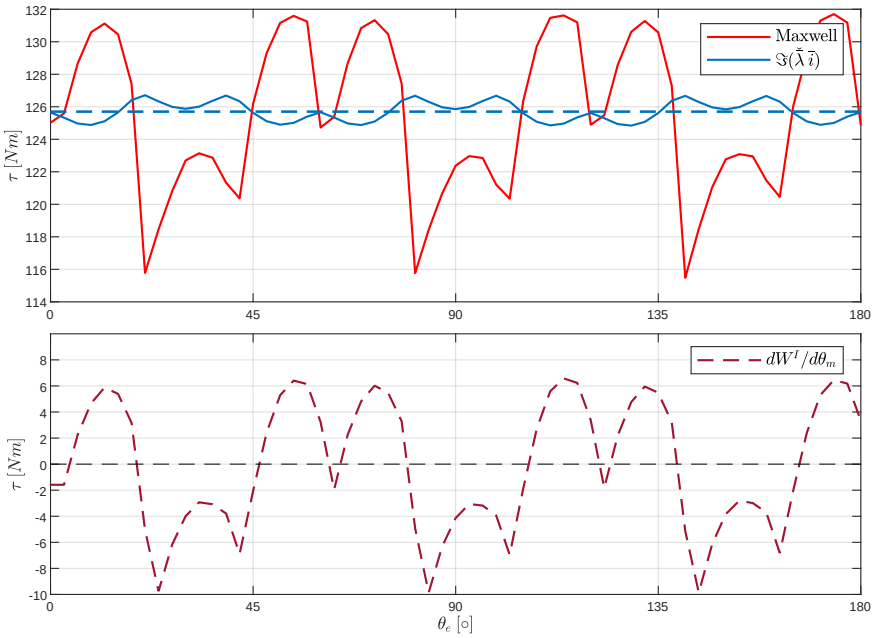

Figure 4.21: 6 pole motor: rated load torque.

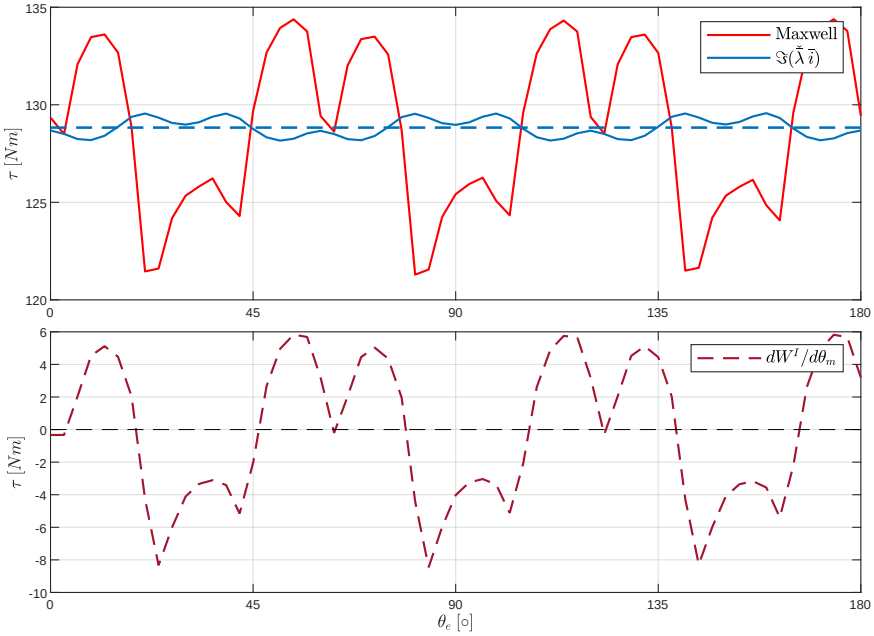

Figure 4.22: 8 pols motor: rated load torque.

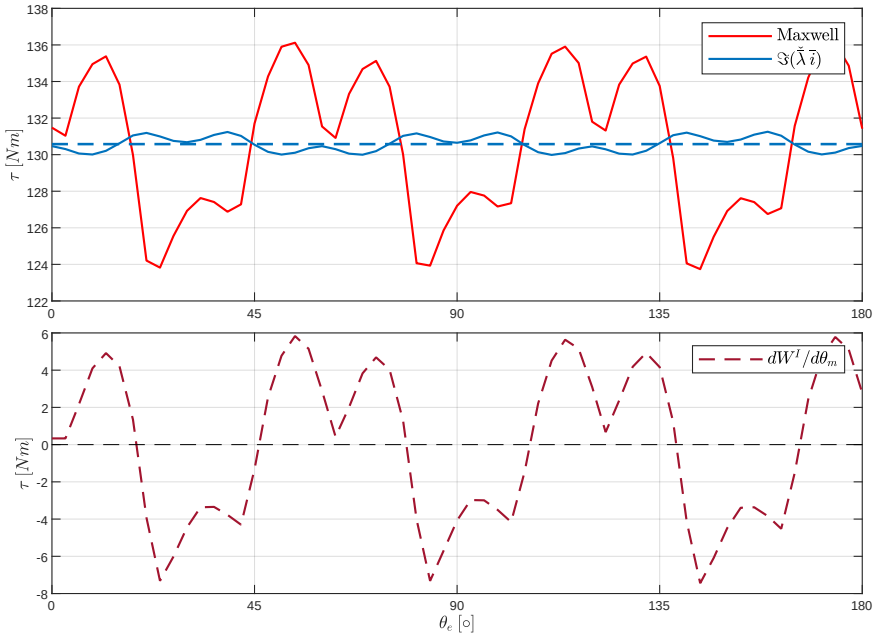

Figure 4.23: 10 pole motor: rated load torque.

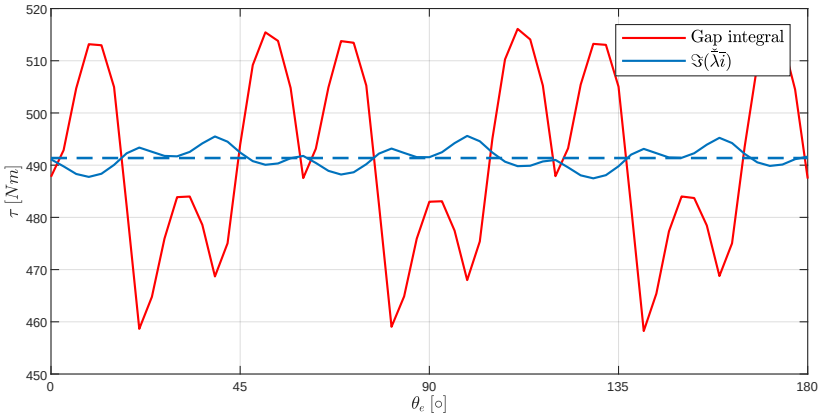

Figure 4.24: 6 pole motor: maximum overload torque.

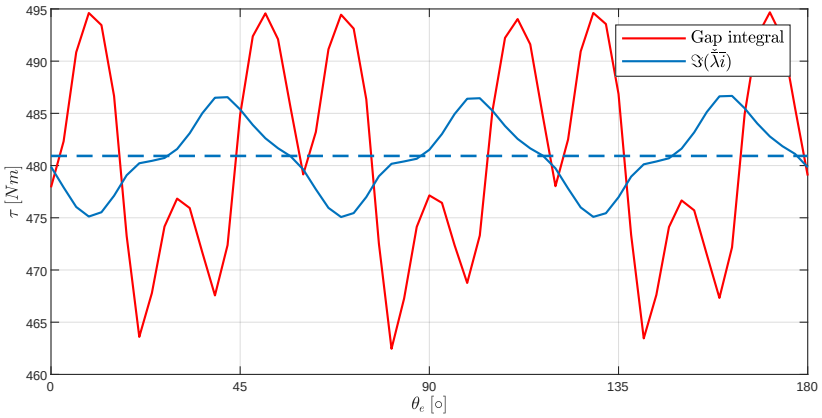

Figure 4.25: 8 pole motor: maximum overload torque.

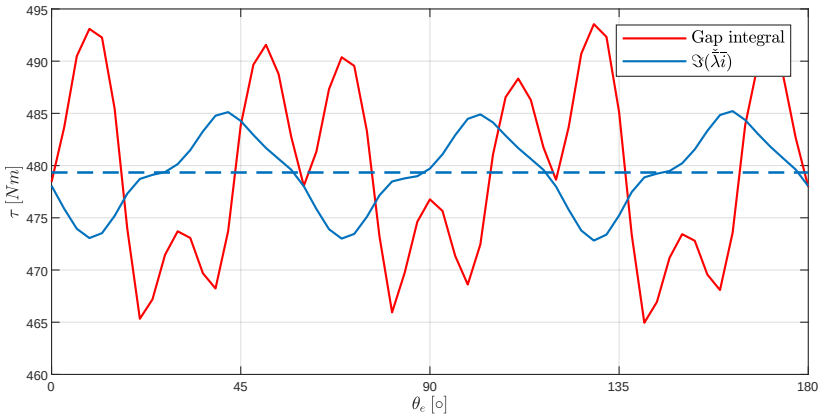

Figure 4.26: 10 pole motor: maximum overload torque.

4.5 Inductance computation

The designed machines have an isotropic magnetic structure, so the inductance on the d axis and the inductance on the q axis are equal and correspond to the so-called synchronous inductance: $L_d = L_q = L$. L is composed by three main contributions: the magnetizing inductance L_m, due to the magnetizing electric load; the slot flux leakage $L_{\sigma_{slot}}$ and the end-winding flux leakage $L_{\sigma_{ew}}$. Leakages due to magnets or teeth skewing do not concern the designed motors, as no skewing has been planned. To compute L through a magnetostatic FEA, a direct-axis rated current is imposed ($i_d = \sqrt{2}I_R$, $i_q = 0$) with the rotor in the $\theta_e = 0$ position and the magnets have been 'turned off', i.e. their coercivities have been set to zero. Then the inductance has been calculated with three different methods to have a comparison on the results.

1. Magnetic energy:
$$L' = \frac{4W}{3i_d}$$

2. Flux linkage:
$$L' = \Lambda_d / i_d$$

3. Fundamental flux density distribution in the air gap:
$$L_m = \frac{B^1_{gd} k_w N_s D_s L_{fe}}{2p i_d}$$
Where B^1_{gd} is the peak value of the first harmonic of the flux density distribution. As an example, the distribution for the 6 pole machine is shown in Figure 4.27, with its harmonic spectrum.

Methods (1) and (2) takes into account both the magnetizing contribution and the slot leakage ($L' = L_m + L_{\sigma_{slot}}$) but they cannot consider the end-winding leakage, because the simulation is bi-dimensional. So the end-turns leakage induction $L_{\sigma_{ew}}$ has been estimated with Someda formula [24]:
$$L_{\sigma_{ew}} = 0.5 \mu_0 \tau_p 2p q_s^2 n_{cs}$$
Method (3) instead considers only the magnetizing inductance, so both leakage contributions must be summed up.

Combining the outcomes from these three computations the synchronous inductance has been separated into its three main components for all the three motors. The results are reported in Table 4.4. The inductances are very small: this is a characteristic feature of SPM motors, that provides a high electromagnetic responsiveness but at the same time limits the speed range of the machine and makes worse the effects of fault in the electric drive. Moreover the filtering action on the high frequency harmonics generated by the inverter PWM technique

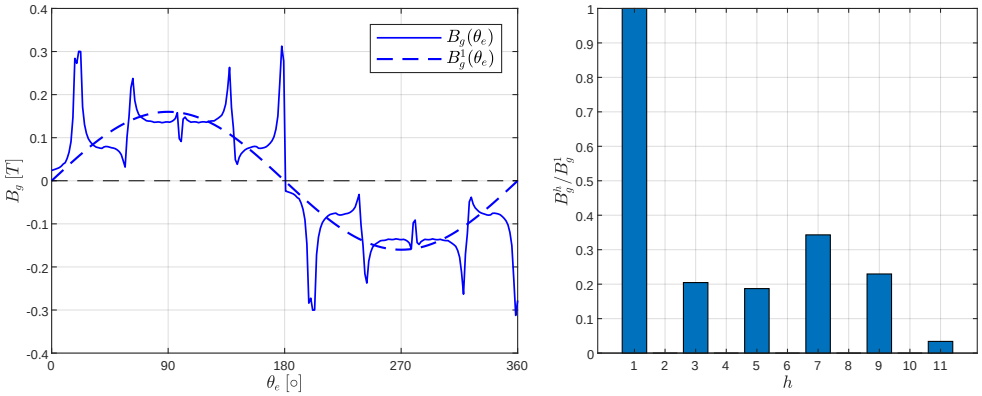

Figure 4.27: 6 pole motor: flux density distribution due only to rated d-axis current.

Table 4.4: Machines inductances in rated load.

2p	/	**6**	**8**	**10**
L_m	$[mH]$	0.70	0.57	0.45
$L_{\sigma_{slot}}$	$[mH]$	0.20	0.38	0.34
$L_{\sigma_{ew}}$	$[mH]$	0.20	0.19	0.14
L	$[mH]$	1.10	1.14	0.93

is very poor. Making a comparison between the three motors, the 8 pole machine has the highest slot leakage because it has the longest slots, whereas the 10 pole machine has the lowest end-winding leakage as it has the shortest end-turns. Then 6 poles motor has the highest magnetizing inductance because it is the less saturated machine and it has the lowest electric load. Finally it is important to underline that the inductance is not completely independent of the load. Indeed the magnetizing contribution depends slightly on the applied current. In this thesis for brevity purpose only the results at rated load are presented and the synchronous inductance is considered independent of the load.

4.6 Winding resistance and Joule losses

The winding resistance and the Joule losses cannot be computed properly with FEMM. So they have been estimated analytically.

The rated in-slot working temperature at steady state has been supposed at $140°C$. An H class has been chosen for the insulating materials, so the maximum in-slot allowable temperature is $180°C$. Considering a safety margin of $15°C$ recommended by the IEC standards, a temperature rise of $25°C$ can be withstand safely during the overloads. The conductor resistivity at the supposed steady-state working temperature has been obtained as follows:

$$\rho = \rho_{20°C}(1 + \alpha(140 - 20)) = 0.0266\ [\Omega\, mm^2/m]$$

Where the parameters of the copper conductor at environmental temperature are: $\rho_{20°C} = 0.018\ [\Omega\, mm^2/m]$, $\alpha = 0.004\ [°C^{-1}]$. Hence the winding phase resistance has been calculated with the following expression:

$$R = \rho \frac{N_s(L_{stk} + l_{ew})}{S_c n_{pp}}$$

Where the end-turns length l_{ew} has been computed as presented in Section 3.9.

Then the Joule losses have been mapped in each working point using the following relation:

$$P_J = 3RI^2$$

Table 4.5: Winding resistance and rated load Joule losses.

Number of poles	**2p**	/	**6**	**8**	**10**
Winding resistance	R	$[\Omega]$	0.121	0.126	0.125
In-slot losses	$P_{J_{slot}}$	$[W]$	300	382	369
End-turns losses	$P_{J_{ew}}$	$[W]$	721	757	739
Total losses	$\boldsymbol{P_J}$	$[\boldsymbol{W}]$	**1021**	**1139**	**1108**

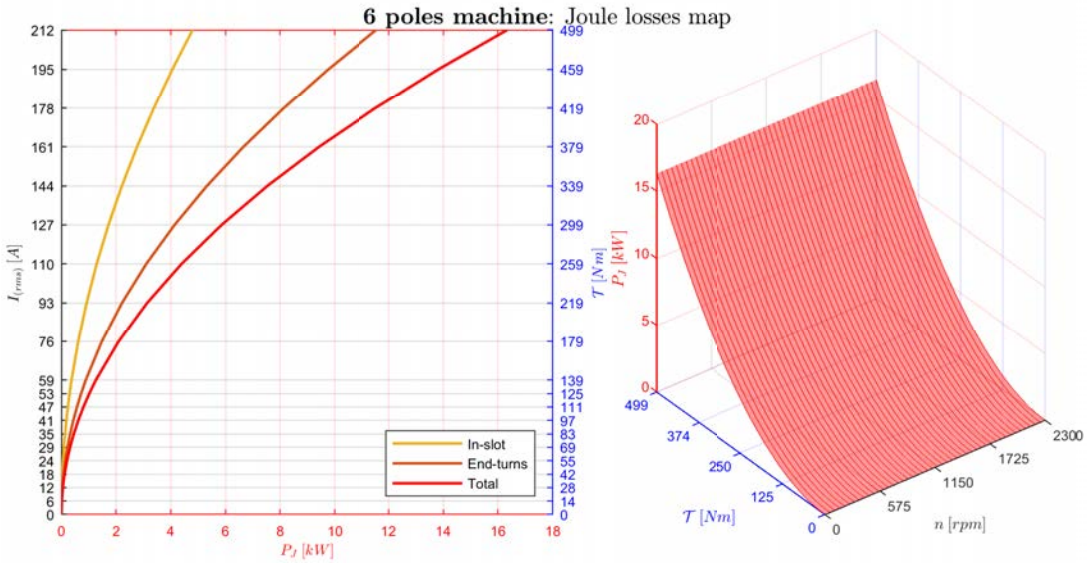

Figure 4.28: 6 pole motor Joule losses map.

That is equivalent to:

$$P_J = \rho J^2 Vol_{Cu}$$

Where I and J are respectively the rms values of the applied current and current density, while $\rho J^2\,[W/m^3]$ are the specific losses. The Joule losses depend on the square of the feeding current, thus they are proportional on the square of the mean torque, according to Equation 3.4. Any losses contribution related to the applied frequency, i.e. the machine speed, due to skin or proximity effects has been neglected because all the chosen wires diameters are much smaller than the copper skin depth at 200 $[Hz]$.

The outcomes of the above presented computations are reported in Figures 4.28-4.29-4.30 and in Table 4.5, where the contributions of the in-slot conductors and end-turns to the rated total Joule losses are distinguished.

4.7 Voltage specifications fulfillment

Once that the winding resistance and the machine inductance are known, the three phase sinusoidal voltage needed to inject a specified current can be found out analyzing the steady-state electrical behavior of the motor when working in MTPA condition, which is graphically represented by the three-phase circuit of Figure 4.31(a) and by the related space vectors diagram in Figure 4.31(b). Thus the needed voltages rms values on rated load and maximum overload have been calculated considering the space vector representation of the three phase quantities or, in an equal way, the phasors of the equivalent one-phase circuit:

$$V_{wind} = \sqrt{\left(E_0 + RI\right)^2 + \left(2\pi f_R L I\right)^2}$$

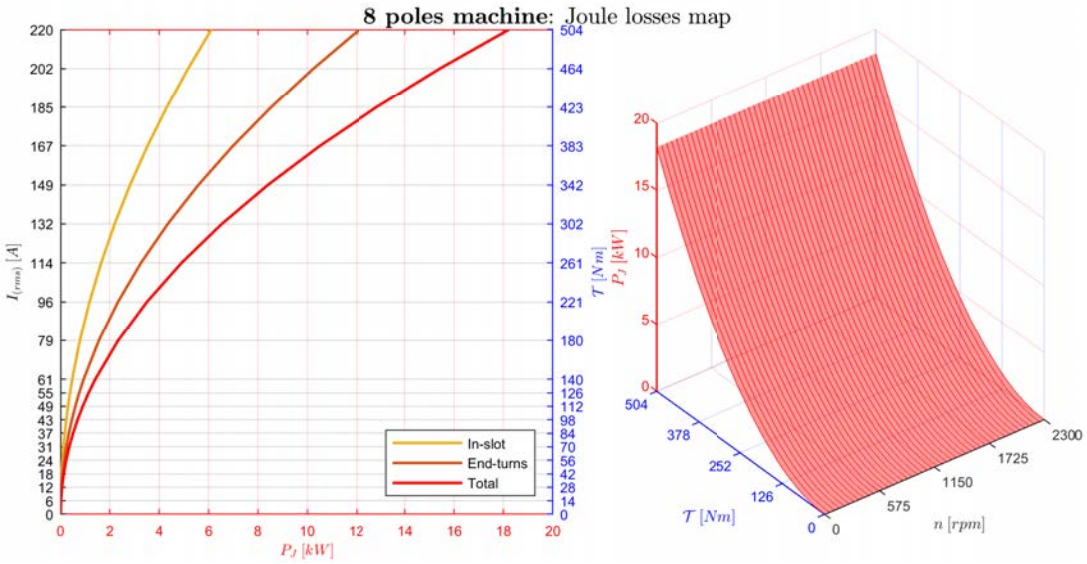

Figure 4.29: 8 pole motor Joule losses map.

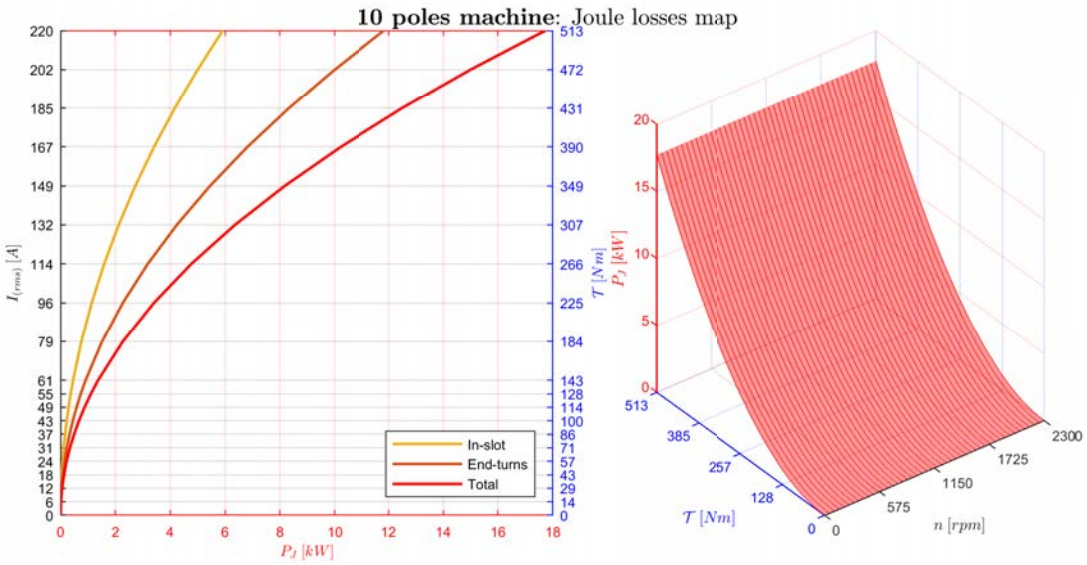

Figure 4.30: 10 pole motor Joule losses map.

Table 4.6: Needed winding voltage on rated load and on maximum overload.

Poles number	**2p**	/	**6**	**8**	**10**
Rated load	V_{wind}	$[V]$	195	191	196
	$\cos\phi$	/	0.99	0.99	0.99
Max. overload	V_{wind}	$[V]$	215	212	217
	$\cos\phi$	/	0.99	0.99	0.98

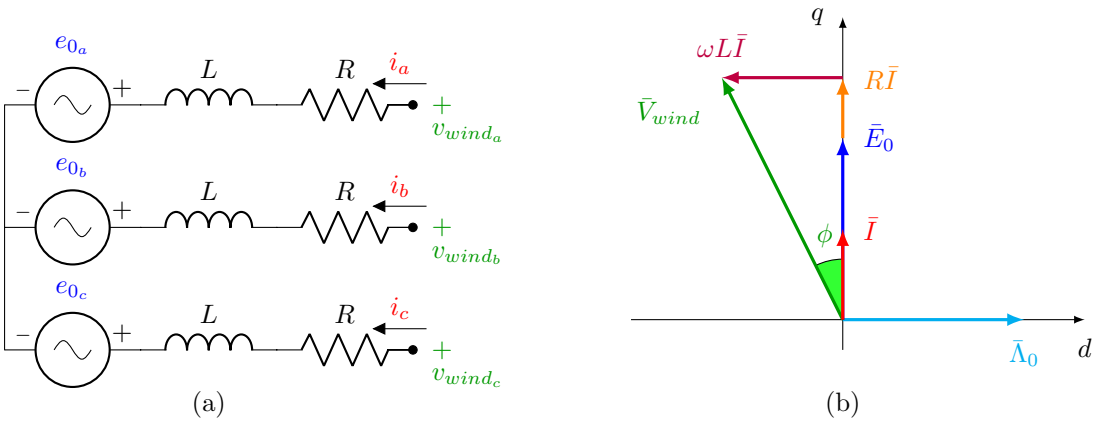

Figure 4.31: SPM motor equivalent circuit (a) and space vectors diagram in MTPA working condition (b).

$$\cos\phi = \frac{E_0 + RI}{V_{wind}}$$

The results are reported in Table 4.6. It can be seen that the inverter works always with a very high power factor and the needed winding voltage are far below the maximum sinusoidal value. So it can be stated that the power electronic components are well exploited in terms of current but not in terms of voltage. Hence a DC bus voltage lower than 700 $[V]$ could be chosen with a benefit in the battery pack sizing.

4.8 Iron and permanent magnets losses

Iron and permanent magnets losses have been mapped through a series of finite elements analysis. The mapping has required several hundreds of FEAs, so the FEMM simulations have been managed using the MATLAB® parallel computation toolbox. To compute the rotating losses the method presented in [41, 42] has been implemented.

Stator iron losses have been obtained considering also the harmonic content due to the non-linear polarization of the flux density vectors. Indeed, looking at the fields pointwise, the vectors do not follow a straight line direction, as it is pointed out in Figures 4.32-4.33, where the ideal linear polarization is compared to the actual behavior of the flux density vector in the middle of the tooth and in the middle of the back iron during a complete electrical rotation of the 6 pole machine. So the iron loss density $p_{fe}\,[W/m^3]$ has been computed in each stator mesh element by applying the well-known Steinmatz formula to every flux density harmonic until the 12^{th} order at the given fundamental frequency $f\,[Hz]$, i.e. at a specified rotating speed $n\,[rpm]$ in the range $0 \div n_n = 2300\,[rpm]$:

$$p_{fe} = \sum_{h=1}^{12} \left[C_{hyst} f_h B_h^2 + C_{eddy} f_h^2 B_h^2 \right]$$

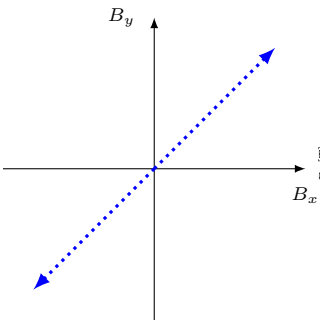

Figure 4.32: Idel linear polarization.

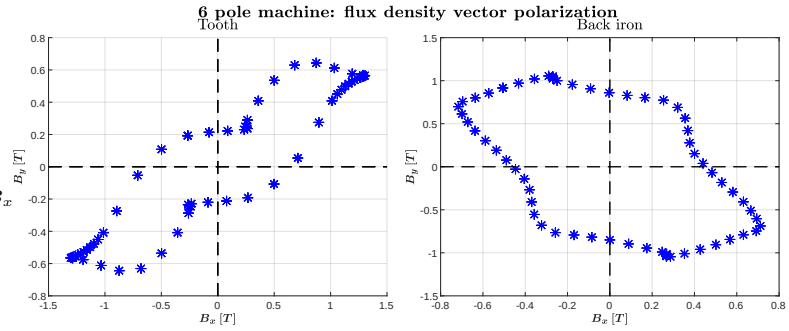

Figure 4.33: 6 poles motor: flux density vector polarization at rated load.

Where $B_h\,[T]$ and $f_h = hf\,[Hz]$ are respectively the flux density magnitude peak value and the frequency of the h^{th} harmonic. The Fourier series coefficients of the flux density magnitude in each mesh element centroid, namely the B_h values, have been computed through the FFT algorithm implemented in MATLAB®. Harmonic orders higher than 12^{th} have not been taken into account because of the relatively coarse mesh used in the simulations, which causes a lot of noise at high frequency. The Steinmatz equation considers both the two contributions to iron losses: the hysteresis effect is taken into account with the coefficient C_{hyst} and changes linearly with the frequency while the eddy current losses are included with the coefficient C_{eddy} and vary with the square of the frequency. The coefficients have been evaluated as follows:

$$C_{hyst} = 0.75\frac{\gamma_{fe} p_{fe_{ref}}}{k_{pack} f_{ref} B_{ref}^2} = \left[W/(Hz\,T^2\,m^3)\right]$$

$$C_{eddy} = 0.25\frac{\gamma_{fe} p_{fe_{ref}}}{k_{pack} f_{ref}^2 B_{ref}^2} = \left[W/(Hz^2\,T^2\,m^3)\right]$$

Where the iron density has been set to $\gamma_{fe} = 7800\,[Kg/m^3]$ while the reference frequency and the reference flux density peak value have been taken respectively as $f_{ref} = 50\,[Hz]$ and $B_{ref} = 1.0\,[T]$, so that the related reference specific loss has been found out from the loss characteristic in Figure 3.17: $p_{ref} = 1.4\,[W/kg]$. As it can be seen the stacking coefficient k_{pack} has been also taken into account. It can be noted that the entire loss density scales by B^2, so it would be expected that the concentration of flux would increase the loss inside the lamination by $1/k_{pack}^2$. Nevertheless, the iron per unit volume also goes down, thus there is less iron per unit volume to generate losses, which gives back a factor of k_{pack}. Overall, the stacking factor can be incorporated in the Steinmatz formulation by dividing the coefficients by the stacking factor. It can be also noted that the main loss contribution is given by the hysteresis effect, whereas eddy current become relevant only at very high frequency thanks to the small laminations thickness and the electrical insulation in axial direction.

The total iron losses have been computed by summing up the loss density elementwise multiplied by the related mesh element volume. The contributions of the teeth and the back iron have been separated to underline their weight in the overall losses and to account for the laminations weakening due to the cutting process. The back iron part is less subjected to cut damages ,then the back iron losses have been increased by 50%, whereas the teeth are affected heavily by the slots shearing off, so the teeth losses have been raised by 100%.

Rotor yoke losses are negligible in steady-state working condition and, thanks to the laminations, they are limited also during the electromechanical transients. Instead permanent magnets are not laminated and their electrical resistivity is not high enough to avoid the flow of eddy current. As a consequence they produce non negligible Joule losses. PMs *'see'* a changing flux even during steady-state rotations, thus they are always affected by eddy current. Indeed the slots openings and the *mmf* generated by the electric load causes a magnetic reluctance variation in the air gap and a distortion of the flux density distribution, which lead to a varying flux on the PMs. The low frequency magnets losses due to slotting and *mmf* have been calculated

as presented in [42]. The low frequency loss density in each PM mesh element $p_{pm_{lf}}$ $[W/m^3]$ can be expressed by the following relation.

$$p_{pm_{lf}} = \frac{1}{2}\rho_{pm}\hat{J}_{pm}^2 \tag{4.1}$$

The NdFeB resistivity at the supposed working temperature of $120°C$ has been set to $\rho_{PM} = 1.5[\Omega mm^2/m]$ while the peak value of the induced current density $\hat{J}_{pm}$ can be further expressed as the time variation of the magnetic vector potential, ignoring the reaction field produced by the eddy current:

$$\hat{J}_{pm} = -\sigma_{pm}\frac{\partial \hat{A}_{pm}}{\partial t} = -\frac{2\pi f}{\rho_{pm}}\frac{\partial \hat{A}_{pm}}{\partial \theta_e}$$

The magnetic vector potential taken at the centroid of each PM mesh element has been decomposed in Fourier series in the same way adopted for the stator flux density vectors. Each harmonic is a sine wave, hence it can be represented in the phasors domain. So the h^{th} harmonic of the induced current density can be written as:

$$\hat{J}_h = -j\frac{2\pi f}{\rho_{pm}}\hat{A}_h$$

And consequently Equation 4.1 becomes:

$$p_{pm_{lf}} = \frac{1}{2}\frac{4\pi^2}{\rho_{pm}}\sum_{h=1}^{12} f_h^2 \hat{A}_h^2$$

Then the magnets low frequency losses have been obtained by summing up the loss density elementwise multiplied by the related mesh element volume.

Another non-negligible contribution to permanent magnets losses is given by the inverter PWM (Pulse Width Modulation). Indeed the synthesized feeding voltage is only approximately a sine wave because a high frequency harmonic content due to switching is always present. Therefore also the feeding current waveform is affected by high order harmonics close to the switching frequency. The amplitude of such noisy high frequency current is heavily related to the filtering action provided by the series inductances in the electric circuit. SPM motors have very low inductances, so the harmonic filtering action is very poor. Thus a noisy signal amplitude of 10% of the load fundamental current has been supposed. For what concerns the inverter, the current specifications of the power switches are relatively trying (rated current above $50\,[A]$ with overloads up to $220\,[A]$), therefore the working frequency should not be high considering standard components. Indeed power switches with high current specifications usually allow relatively low working frequency. So a switching frequency of $10\,[kHz]$ has been hypothesized. High frequency PMs losses cannot be computed neither with magnetostatic FEA, as they do not consider any eddy current, nor with pure harmonic analysis, as they do not account for the constant field offset given by the magnets. Therefore the computation has been performed thanks to the incremental permeability procedure available in FEMM software, which allows the steady-state solution of a harmonic problem at a given frequency starting from a DC offset. The harmonic solution can be calculated steady-state because the switching frequency is always several hundreds of times higher than the fundamental frequency, which can be included in the DC offset together with the flux generated by the PMs. The high frequency loss density in each PM element $p_{pm_{hf}}$ $[W/m^3]$ has been computed as in Equation 4.1, where the current density is the one induced by the noisy feeding current at switching frequency. Then again the total losses have been obtained summing up the loss density elementwise multiplied by the related mesh element volume.

The iron and permanent magnets losses maps are reported in Figures 4.34-4.36-4.38 for all the three designed motors. It can be noted that the PM losses cannot be neglected as they are about the 50% of the overall iron losses. All components depend more on the feeding frequency, i.e. the speed, than on the applied electric load, except for the high frequency PM losses, which vary with the feeding current and they are independent on the speed. Such contribution

Table 4.7: Iron and PM losses on rated working condition.

Poles number	**2p**	/	**6**	**8**	**10**
Back iron	$P_{fe_{bi}}$	$[W]$	270	214	254
Teeth	P_{fe_t}	$[W]$	215	284	374
Overall iron	$\boldsymbol{P_{fe}}$	$[\boldsymbol{W}]$	**485**	**498**	**628**
PM low freq.	$P_{pm_{lf}}$	$[W]$	70	191	217
PM high freq.	$P_{pm_{hf}}$	$[W]$	136	210	189
Overall PM	$\boldsymbol{P_{pm}}$	$[\boldsymbol{W}]$	**206**	**401**	**406**

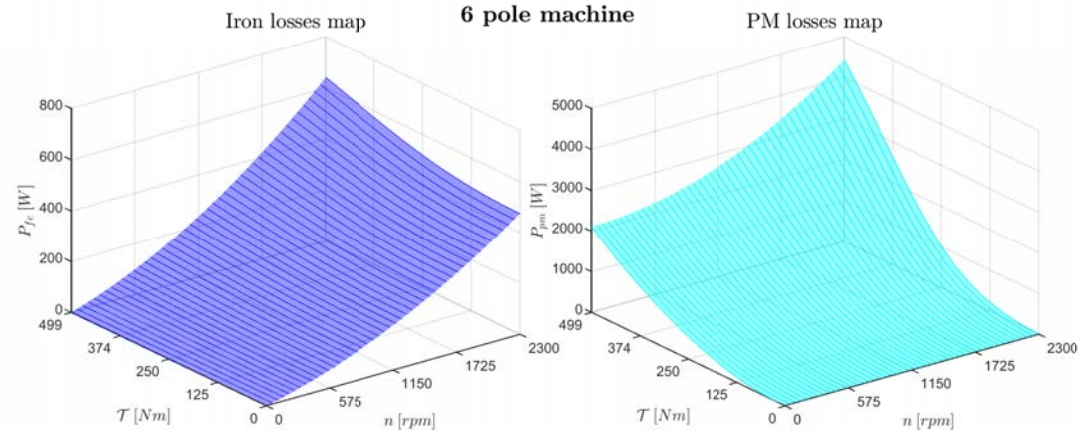

Figure 4.34: 6 pole machine: iron an PM losses maps.

becomes very relevant at high electric loads. Figures 4.35-4.37-4.39 highlight the weights of all the rotating losses components as well as the contribution of the polarization harmonic content in the overall iron losses.

The results on rated working condition, i.e. at the base point, are summarized in Table 4.7 for all the three machines.

4.9 Efficiency

The efficiency map of each machine has been obtained from the losses characterizations presented in the previous sections.

The electrical machines are also affected by mechanical losses caused by frictions in bearings and ventilation in the air gap and around the shaft. This losses contribution has been estimated through the following empirical formulation, that is based on statistical investigations on similar motors in the same speed range [24]:

$$P_{mec} = 0.7 \cdot P_{[kW]}\sqrt{n_{[rpm]}}$$

In every working point, $P_{[kW]}$ is the useful mechanical power generated at the shaft while $n_{[rpm]}$ is the rotating speed. Hence the efficiency has been computed with a 10% increase of the overall losses to consider also additional non evaluable contributions:

$$\eta = \frac{P}{P + 1.1(P_J + P_{fe} + P_{pm} + P_{mec})}$$

The resulting efficiency maps are shown in Figures 4.40-4.41-4.42, where the rated torque (red line) and the maximum overload capability (blue line) are underlined. The losses and efficiency at rated load are summarized in Table 4.8. It can be seen that the efficiency is quite similar

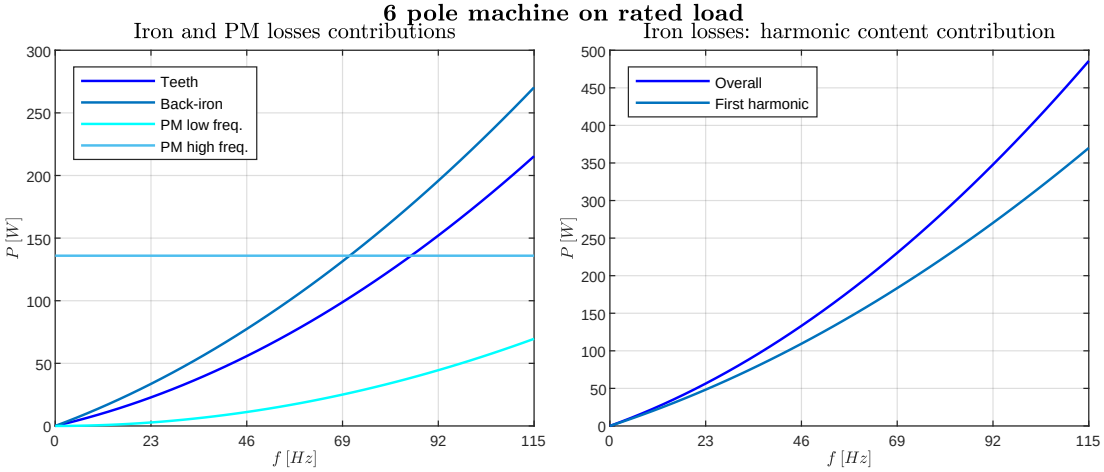

Figure 4.35: 6 pole machine: iron an PM losses contributions at rated load and varying frequency.

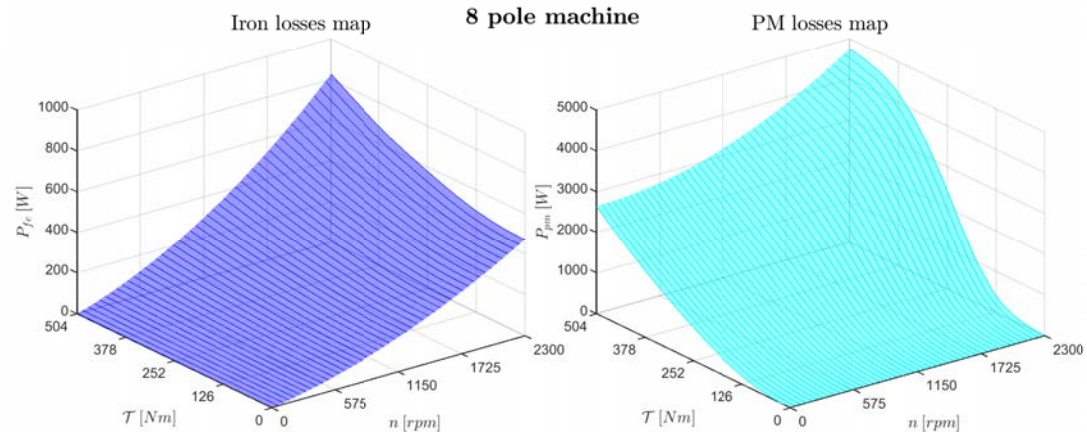

Figure 4.36: 8 pole machine: iron an PM losses maps.

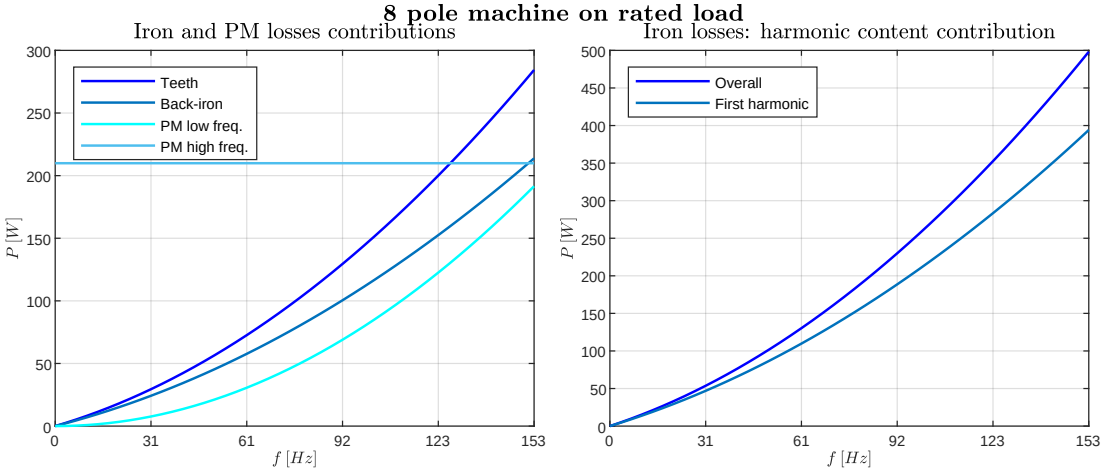

Figure 4.37: 8 pole machine: iron an PM losses contributions at rated load and varying frequency.

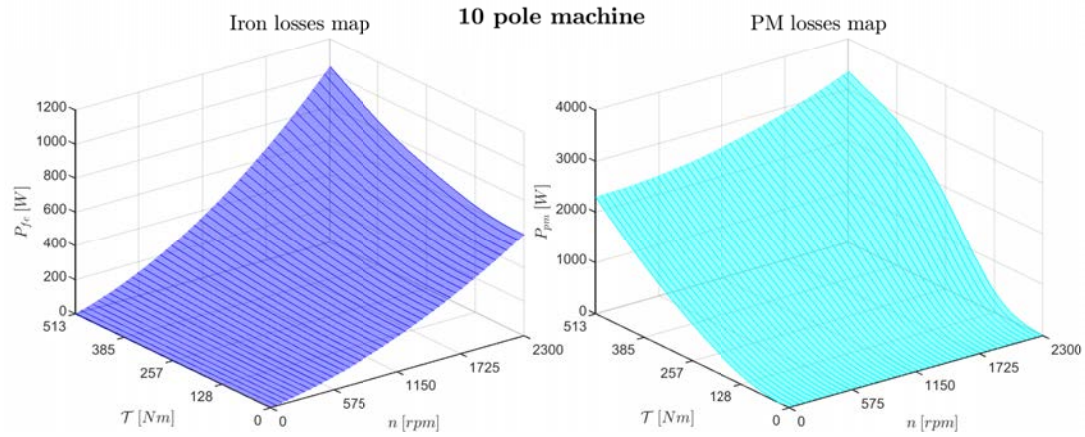

Figure 4.38: 10 pole machine: iron an PM losses maps.

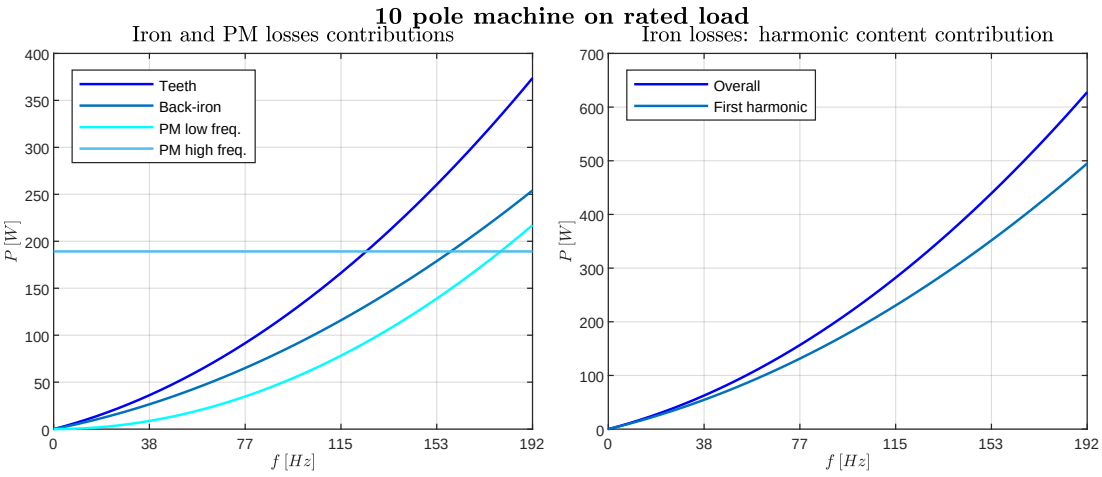

Figure 4.39: 10 pole machine: iron an PM losses contributions at rated load and varying frequency.

Table 4.8: Losses and efficiency at rated load.

Number of poles	**2p**	/	**6**	**8**	**10**
Joule losses	P_J	$[W]$	1021	1139	1108
Iron losses	P_{fe}	$[W]$	485	498	628
PM losses	P_{pm}	$[W]$	206	401	406
Mechanical losses	P_{mec}	$[W]$	1000	1019	1038
Efficiency	η	$[/]$	0.909	0.900	0.898

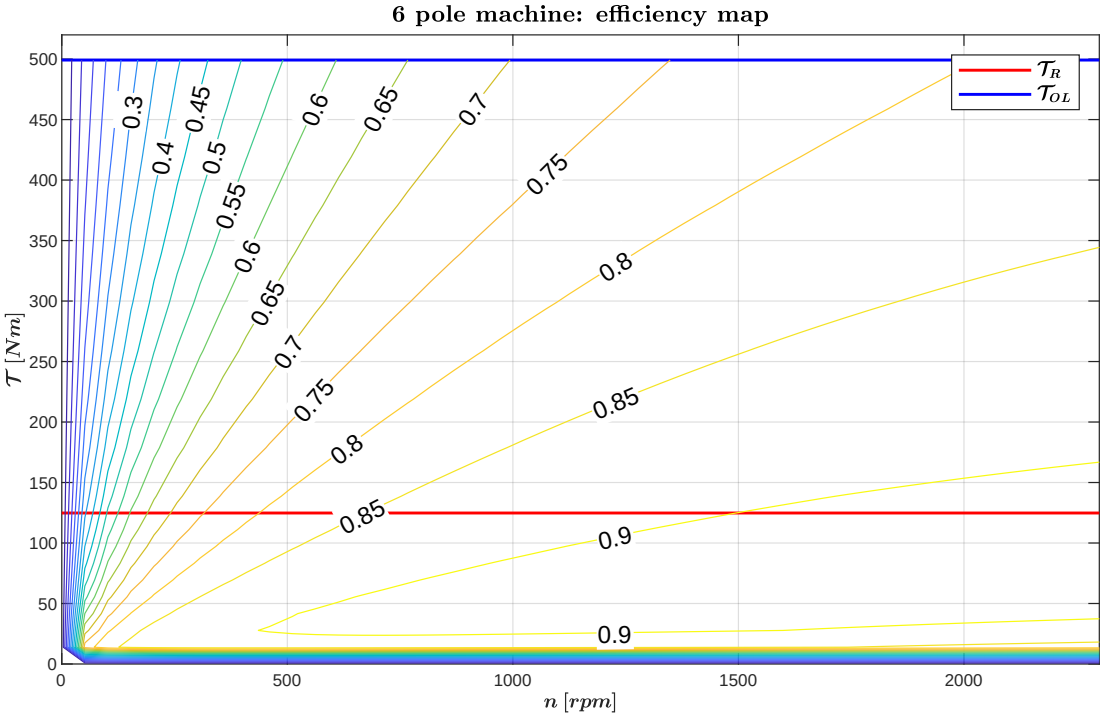

Figure 4.40: 6 pole machine: efficiency map.

between the three motors. The 10 pole machine suffers a bit more the iron and permanent magnet losses due to its higher feeding frequency.

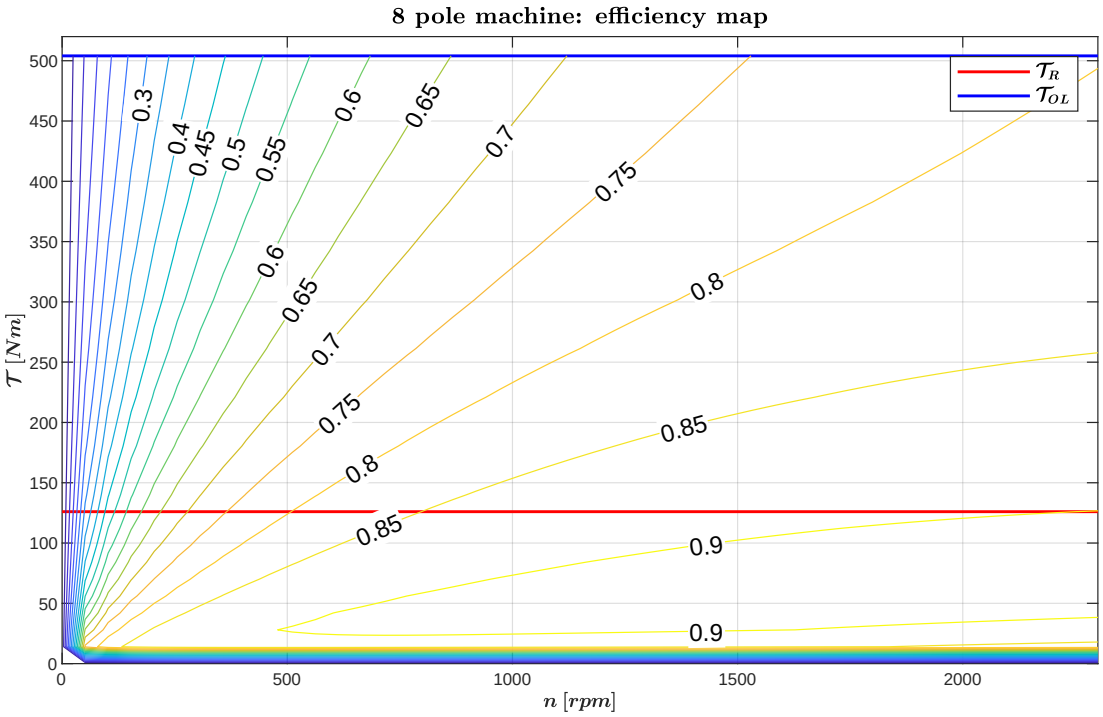

Figure 4.41: 8 pole machine: efficiency map.

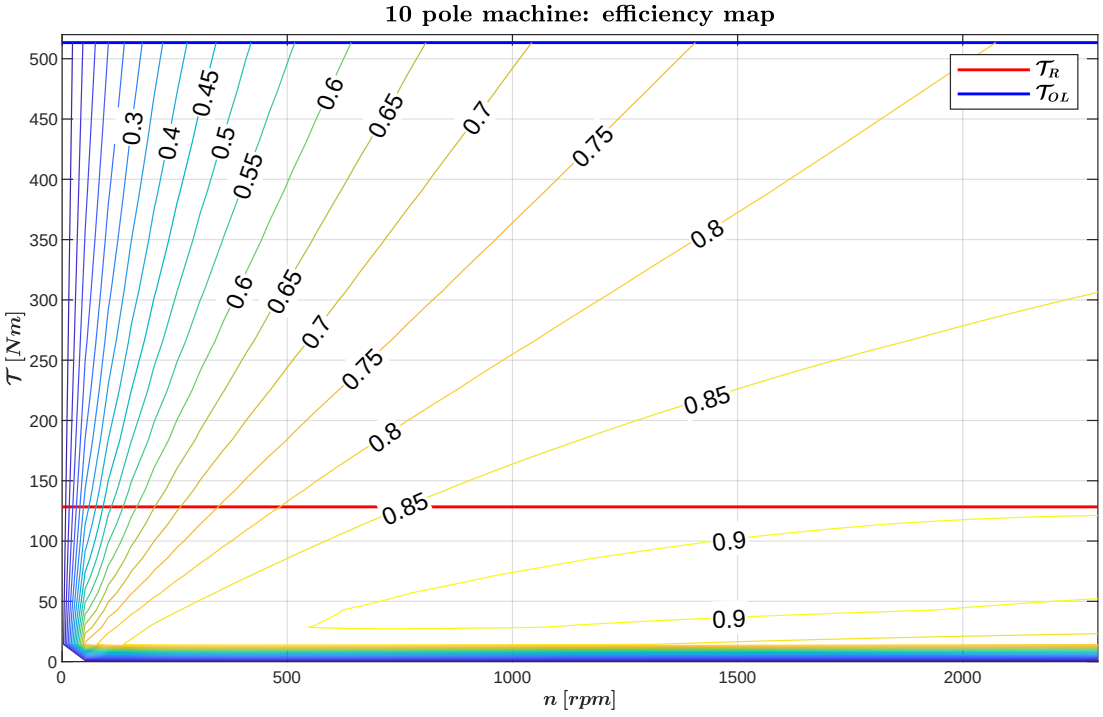

Figure 4.42: 10 pole machine: efficiency map.

Chapter 5

Cooling system design and thermal analysis

In this chapter the design of the cooling system and consequent thermal analysis on the machines will be presented.

At the beginning the choice of the cooling device will be briefly discussed and justified. The chosen system has been designed following an analytical method based on a semi-empirical fluid-dynamics model of the convective heat exchange with a coolant. The model makes extensive use of the dimensionless numbers that characterize fluids motion and the convection heat transfer.

After that the cooling system has been completely defined, some significant thermal analysis on the three designed motors have been done. The temperature maps of the three machines have been obtained firstly at steady state on rated load, i.e. when the machine works at the base point, with finite element analysis accomplished thanks to the thermal solver (FEH: *Finite Element Heating*) of the FEMM software. Then the thermal step response to rated load has been analyzed by solving a linear lumped-parameters equivalent network (LPN) in Simulink® in order to compute the actual thermal time constants of the motors and make a comparison with the values supposed before the machines design (Section 2.6). A comparison between the thermal steady state obtained with FEMM and with the LPN has also been done, looking especially at the slot and magnet temperature, which are the most thermal-sensitive parts of the motors. In the end the transient thermal behavior of the three designed machines has been analyzed using the LPN during the most critical duty cycle available, i.e. the transportation test, in order to assess how much the motors are able to withstand a real working condition without suffer damaging overtemperatures.

5.1 Water jacket design

For this project the cooling system of the three designed motors consists in an inox steel water jacket with a spiral channel which in the coolant is kept in motion by a pump.

The denomination '*water jacket*' could mislead. Indeed in the application under analysis pure water cannot be use as in cold seasons it can easily freeze with consequent damages to the entire system. So the coolant is a solution of propylene glycol: a concentration of $20 \div 30\%$ is enough to lower the freezing point under $-10°C$. Propylene glycol has quite the same thermo-physics properties of ethylene glycol, another fluid commonly used in cooling systems, but it is far less toxic and easier to synthesized. Therefore, when possible, propylene glycol is preferable.

The water jacket is made of inox steel. Such material has been preferred to aluminum because it is more suitable for a hydraulic system thanks to its greater resistance against oxidation and corrosion, despite its weight and production cost are higher. A layout with a single spiral duct has been chosen instead of a single axial channel because the aspect ratio of all the designed motors is very low. As a consequence, in axial direction there is less available surface to heat exchange and an axial duct should be manufactured with a lot of tight pipe-bends, so that the friction losses increase a lot and more power from the pump is needed to

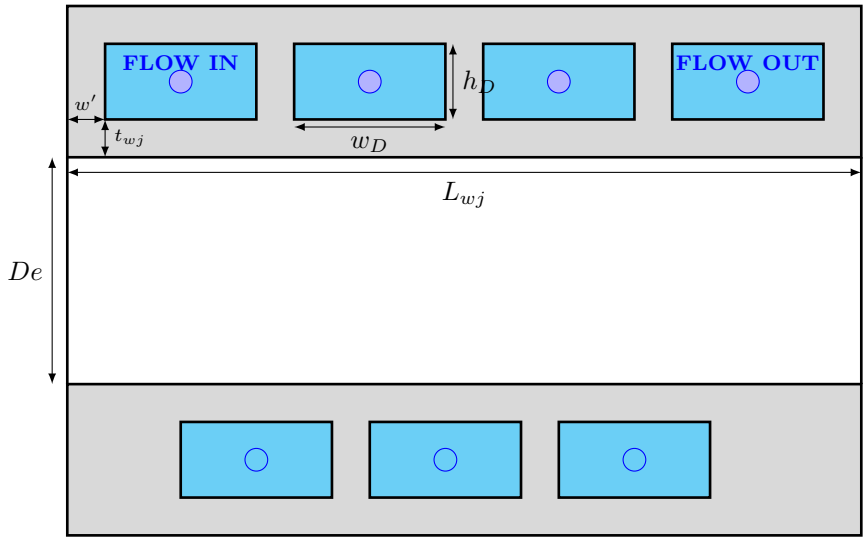

Figure 5.1: Layout of the water jacket.

overcome the pressure drop and keep the coolant in motion at the wanted velocity.

The water jacket designed has been carried out referring to the geometry drawn in Figure 5.1. As it can be seen the spiral pitch is developed along an entire turn, i.e. along all the external circumference. In this way the heat dissipation is more uniformly distributed along the stack length avoiding localized hot spots. Moreover the inflow and the outflow sections of the cooling channel are situated in the same side of the machine. Such trick is worthwhile to shorten the pipe length that does not take part into the heat exchange with the machine in order to reduce unwanted hydraulic losses and require less power from the pump. The total axial length of the water jacket has been set to $L_{wj} = 70[mm]$, a bit more than the stack lengths of the three machines in order to cover properly all the stacks and at the same time to have enough space to try different number of turns for the spiral duct N_{D_t}. The halfway widths w' as well as the inox steel thickness t_{wj} have been set to 4 $[mm]$ to allow an easy manufacturing without subtract too much volume to the cooling channel. The width of the duct w_D has been computed for each attempt of spiral turns as follows:

$$w_D = \frac{L_{wj} - (N_{D_t} + 2)w'}{N_{D_t} + 1}$$

To obtained the height h_D, the half-perimeter of the duct rectangular cross section $p_D = h_D + w_D$ has been compute for each machine using the following analytical procedure [33].

The heat dissipation capacity of the coolant can be expressed as follows:

$$q_{loss} = \dot{m} c_{p_f} \Delta T_f = \gamma_f \dot{Q} c_{p_f} \Delta T_f = \gamma_f v_f S_D c_{p_f} \Delta T_f \tag{5.1}$$

The coolant temperature raise has been set to $\Delta T_f = T_{out} - T_{in} = 4°C$, a difference that has been considered small enough to provide a heat exchange uniformly distributed along the cooling channel without requiring an excessive effort to pump the needed flow rate. So supposing an inflow temperature $T_{in} = 40°C$, as suggested by the IEC standards for the thermal study of the electrical machine [24], the fluid leaves the circumferential duct at the temperature of $T_{out} = 44°C$. Thus, to evaluate the convective heat transfer, the thermo-physics properties of the coolant has been taken at the average temperature of $T_f = 42°C$. The data are reported in Table 5.1.

From Equation 5.1 it can be noted that setting the temperature raise ΔT_f means to define also the coolant flow rate at equal heat power q_{loss} $[W]$, both in terms of mass $\dot{m}$ $[kg/s]$ and volume $\dot{Q} =$ $[l/s]$. The heat power q_{loss} considered in the water jacket design is the sum of the total Joule losses, the stator iron losses and the permanent magnet losses at rated torque

Table 5.1: Coolant thermo physics properties at average working temperature.

Coolant	**30% solution of propylene glycol**		
Parameter	**Symbol**	**Unit**	**Value**
Mean working temperature	T_f	$[°C]$	42
Density	γ_f	$[kg/m^3]$	1026
Dynamic viscosity	μ_f	$[kg/m\ s]$	$1.213 \cdot 10^{-3}$
Kynematic vicosity	ν_f	$[m^2/s]$	$1.183 \cdot 10^{-6}$
Specific heat capacity	c_{p_f}	$[J/kg°K]$	3782
Thermal conductivity	λ_f	$[W/m°K]$	0.496
Prandtl number	Pr	$[/]$	9.246

and rated speed, namely when the motor works at the base point. The design has been done on the rated load. Indeed the overload losses cannot be dissipated through the coolant because the thermal time constant of the heat exchange between duct wall and fluid, which determine how quickly the temperature difference increase at every applied heat flux, is much greater than the thermal time constant of the heat exchange between the slots and the stator iron [33]. Mechanical losses have not been taken into account as it has been supposed that they are entirely dissipated near the bearings.

The fluid average velocity is related to the dimensionless Reynolds number Re, which is defined as:

$$Re = \frac{\gamma_f v_f d_D}{\mu_f} = \frac{v_f d_D}{\nu_f} \tag{5.2}$$

Where the hydraulic diameter of the duct d_D is defined as the ratio between 4 times the cross section area S_D and the perimeter touched by the fluid:

$$d_D = \frac{4S_D}{2(h_D + w_D)} = \frac{2S_D}{p_D} \tag{5.3}$$

So, making explicit the fluid velocity, Equation 5.2 becomes:

$$v_f = \frac{Re\mu_f p_D}{2\gamma_f S_D} \tag{5.4}$$

And the substitution of the previous expression in Equation 5.1 yields to:

$$q_{loss} = \frac{Re\mu_f p_D c_{p_f} \Delta T_f}{2} \tag{5.5}$$

The Reynolds number is very relevant in fluid-dynamics studies as it defines the type ot flow: $Re < 2300$ is assumed as pure laminar flow; $Re > 10000$ is considered fully developed turbulent flow; values in the range $2300 \div 10000$ means the presence at the same time of both laminar and turbulent flow. In electrical machines cooling devices a fully developed turbulent flow is preferred because it improves the convective heat exchange [33]. But too high Reynolds numbers leads to very high fluid speed that could require too much power from the pumping system (or the fans system in case of air cooled machines). So in this project Reynolds number has been set to $Re = 10000$, as suggested also in [33] for the same type of motors. Thus, making explicit p_D in Equation 5.5, the duct half-perimeter has been computed as follows for each sizing attempts:

$$p_D = \frac{2q_{loss}}{Re\mu_f} c_{p_f} \Delta T_f$$

And the height h_D has been consequently obtained as:

$$h_D = p_D - w_D$$

At this point the coolant average speed v_f can be also computed with Equation 5.4.

Then the convective coefficient α_{wj} has been calculated. α_{wj} represents the heat exchange between the water jacket walls and the coolant so it is fundamental for further thermal analysis of the machines, as it will be described later on. The convective coefficient can be expressed as follows:

$$\alpha_{wj} = \frac{\lambda_f Nu}{d_D} \tag{5.6}$$

Where Nu is the Nusselt dimensionless number. A lot of experimental correlations have been proposed to evaluate Nu. Among them the Gnielinsky equation has been adopted in this project, because it is one of the latest proposal and it is affected by the lowest errors in a wide range of different flows, as reported by the validity constrains below:

$$Nu = \frac{\left(\frac{\xi}{8}\right)(Re - 1000) \cdot Pr}{1 + 12.7 \cdot \left(\frac{\xi}{8}\right)^{0.5} \cdot \left(Pr^{2/3} - 1\right)}$$

$$\begin{cases} 0.5 \leq Pr \leq 2000 \\ 3 \times 10^3 \leq Re \leq 50 \times 10^6 \end{cases}$$

Pr is the dimensionless Prandtl number. It depends only on the fluid properties, according to its definition:

$$Pr = \frac{\mu_f c_{p_f}}{\lambda_f}$$

The Prandtl number of the coolant at the average working temperature is reported in Table 5.1 among the other thermo-physics parameters [43].

ξ is the Darcy-Weisbach friction factor [44], which takes into account the improvement in the convective heat exchange due to the asperities in the duct walls surfaces. Also to evaluate this dimensionless coefficient a lot of empirical correlations have been proposed in the technical literature. Furthermore ξ can be quickly estimated using the well-known Moody diagram. In this project the friction factor has been evaluated by solving the Colebrook-White equation with a Newton-based root-finding method [44]. The secant algorithm has been implemented again, as it was done during the preliminary sizing of the motors.

$$\frac{1}{\sqrt{\xi}} = 1.74 - 2\log\left(\frac{2e}{d_D} + \frac{18.7}{Re\sqrt{\xi}}\right)$$

The inox steel sharpness has been set to $e = 0.1\ [mm]$. Colebrook-White correlation is not one of the most recent proposal but it guarantees satisfying results in a wide range of different flows.

Several attempts have been made to size the water jacket. The final choice for each motor has been based on the power performances required to the pump. The power needed to keep the coolant flowing has been computed as follows:

$$P_{pump} = \gamma_f \dot{Q} g H$$

Where $g = 9.81\ [m/s^2]$ is the gravitational acceleration while $H\ [m]$ is the head of the pump. The friction losses causes the main pressure drop along the channel, so H has been estimated with the Darcy-Weisbach equation, supposing that the duct curvature can be neglected because of the high external diameter of the machines as well as the localized losses in the inflow and outflow joints.

$$H = \xi \frac{v_f^2 L_D}{2 d_D g}$$

The total lenght of the duct has been evaluated as:

$$L_D = N_{D_t} \pi (D_e + 2t_{wj} + h_D)$$

The outcomes from the sizing attempts are reported in Table 5.2, where the definitive choices

Table 5.2: Water jacket design attempts.

$2p$ [/]	q_{loss} $[W]$	N_{D_t} [/]	w_D $[mm]$	h_D $[mm]$	v_f $[m/s]$	α_{wj} $[W/m^2\,°C]$	$\dot{Q}$ $[l/s]$	H $[m]$	P_{pump} $[W]$
6	1712	3	12.5	6.5	1.38	3112	0.11	0.65	0.73
		4	9.2	9.8	1.25	2754	0.11	0.62	0.70
		5	7.0	12	1.34	2992	0.11	0.98	1.10
8	2038	2	18.0	5.0	1.51	3457	0.14	0.48	0.66
		3	12.5	10.5	1.04	2223	0.14	0.22	0.30
		4	9.2	13.8	1.07	2310	0.14	0.32	0.44
		5	7.0	16	1.21	2672	0.14	0.61	0.84
10	2142	2	18.0	6.0	1.31	2930	0.14	0.31	0.44
		3	12.5	11.5	0.99	2103	0.14	0.19	0.27
		4	9.2	14.8	1.04	2238	0.14	0.30	0.45
		5	7.0	17	1.19	2616	0.14	0.58	0.83

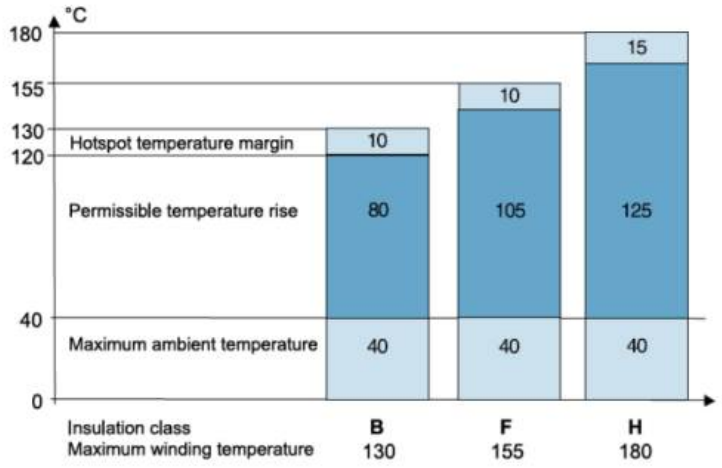

Figure 5.2: Insulating thermal class.

for each machine are underlined.

5.2 Steady state thermal analysis at rated load

Some relevant thermal analysis have been done to assess the actual working temperatures of the most critical parts of the machines, i.e. the slot and the permanent magnets. Both the in-slot insulating materials and the permanent magnets belong to the H thermal class, so they can withstand a maximum temperature of $180°C$ without damaging, as reported in Figure 5.2. However the IEC standard for the electrical machines design suggests a safety margin of $15°C$ and fix the reference environmental temperature to $40°C$. Thus, an overtemperature below the limit of $125°C$ is recommended. The motors thermal behavior has been studied both at steady-state and during a duty cycle transient. The steady state temperature maps at rated load have been obtained through FEA using the thermal solver implemented in FEMM software. The outcomes are reported in Figures 5.3-5.45.5. The great quantity of points scattered in the stator lamination and in the PMs has been needed in the pre-processing phase to represent concentrated heat generation spots. Indeed, while the total Joule losses produced by the rated current have been uniformly allocated in the slots cross sections, the iron and PM losses have been imposed according to the loss density distribution computed in Section 4.8 at rated

speed and rated torque. It is important to specify that the Joule loss density set in the slots takes into account also the end-winding contribution, as it has been likely supposed that the heat dissipation coefficient, which represents the free convection in the end-turns, is too low if compared to the copper thermal conductance, so the heat flux can be considered originated entirely from the in-slot conductors.

Inside the slots are placed enameled copper wires electrically insulated with Nomex® tapes and impregnated in epoxy resin. To properly model the thermal behavior of such cluttered assembly, an equivalent thermal conductivity λ_{slot} has been evaluated with Milton formula [33, 45].

$$\lambda_{slot} = \lambda_{res} \frac{(1 + k_{fill})\lambda_{Cu} + (1 - k_{fill})\lambda_{res}}{(1 - k_{fill})\lambda_{Cu} + (1 + k_{fill})\lambda_{res}} \tag{5.7}$$

Where $k_{fill} = 0.40$ is the slot fill factor, λ_{Cu} is the copper thermal conductivity and $\lambda_{res} = 0.20\,[W/m°C]$ is the thermal conductivity assumed for all the insulating materials (enamel, resin and Nomex®). The thermal resistance of the insulating layer between slot and iron as well as the wedge are also considered, but using a conductivity of $\lambda_{ins} = 0.18\,[W/m°C]$.

The water jacket cooling has been represented with an external convective boundary whose coefficient is the one reported in Table 5.2 for each motor. The conductive heat transfer provided by the inox steel thickness t_{wj} has also been considered as well as an additional layer of $2\,[mm]$ with a thermal conductivity of $2.47\,[W/m°C]$, which represents the thermal resistance due to the non-ideal contact between the stator laminations and the water jacket [33]. To include the permanent magnets losses into the simulation the heat exchange in the air gap must be modeled. To consider the impact of the rotational flow on the convection phenomenon in an air gap, various experimental correlations have been proposed in the technical literature. In this project the traditional empirical formulation based on the dimensionless Taylor number Ta has been adopted [45]. The Taylor number is defined as:

$$Ta = \frac{v_{rot}}{\mu_{air}} \sqrt{\frac{(g - t_{band})^3}{R_{rot}}} \tag{5.8}$$

Where:

- $g - t_{band} = 0.6\,[mm]$ is the actual air gap radial thickness; it is useful to remember that the dimension $g = 1\,[mm]$ includes $0.6\,[mm]$ of air and the permanent magnets bandage thickness $t_{band} = 0.4\,[mm]$, which can be neglected in electromagnetic studies but it must be distinguished in thermal analysis;
- $R_{rot} = (D_s - 2(g - t_{band}))/2$ is the outer rotor radius;
- $v_{rot} = R_{rot}\omega = R_{rot}\pi n/30\,[m/s]$ is the rotor peripheral velocity; in this case the rotor angular speed is the rated speed $n = n_R = 2300\,[rpm]$;
- μ_{air} is the dynamic viscosity of air at the environmental temperature of $40°C$ and at atmospheric pressure.

The Nusselt number has been computed with one of the following correlations, depending on the Taylor number, which defines the type of rotational flow:

$$Nu = \begin{cases} 2 & Ta < 41 \quad laminar \\ 0.212 Ta^{0.63} Pr^{0.27} & 41 \leq Ta \leq 100 \quad vortex \\ 0.386 Ta^{0.5} Pr^{0.27} & Ta > 100 \quad turbulent \end{cases} \tag{5.9}$$

Where Pr_{air} is the Prandtl number of air at $40°C$ and atmospheric pressure. The thermophysics properties of air are reported in Table 5.3, among the other materials parameter used to set up the thermal simulations [44, 45]. It is important to underline that all the materials have been considered isotropic, which means that their thermal conductivities are equal along every direction. Finally the convective coefficient has been calculated as:

$$\alpha_{gap} = \frac{\lambda_{air} Nu}{(g - t_{band})} \tag{5.10}$$

The rotor holes behave as additional cooling ducts. The motors have horizontal shafts and are not equipped with fans, so neither a free convection nor an air forced convection can take place. Nevertheless, the machines' aspect ratios are very low, thus the vortex flow generated on the external rotating surfaces can easily expand inside the short stack length through the rotor holes. Again, to model this phenomenon a wide variety of empirical correlations have been proposed. In this study the traditional Morris formulation has been used [45]. Such theory considers the case of a forced flow inside rotating ducts about a parallel axis, where a parallel straight flow combines with a vortex flow. Indeed the Nusselt number is derived as follows:

$$Nu = 0.012 Re_{axi}^{0.78} Re_{rot}^{0.18} \tag{5.11}$$

Where Re_{axi} and Re_{rot} are the Reynolds numbers correlated respectively to the axial flow and to the rotating flow. R_{axi} has been evaluated with Equation 5.2 supposing a very low axial average velocity ($0.2\,[m/s]$), as the motors under analysis are not equipped with fans. Re_{rot} instead is defined by the following expression:

$$Re_{rot} = \frac{\omega d_{rot}^2}{8\nu_{air}} \tag{5.12}$$

For steady-state FEA the speed has been set to rated speed $\omega = \omega_R = \pi n_R/30\,[rad/s]$ while the hydraulic diameter of the rotor holes d_{rot} has been obtained as in Equation 5.3, where the cross section areas and the perimeters have been calculated with the tools implemented in FEMM post-processing interface. Then the convective coefficient has been computed with Equation 5.6. In the end a zero heat flux boundary condition has been imposed on the shaft diameter.

It is important o underline that the reference temperature in the FEA simulations has been set to $0°C$, so that the results must be red in terms of overtemperatures. Looking at Figures 5.3-5.45.5 it can be seen that the slot overtemperatures remain far below the limit of $125°C$ in each motor. This is due to the prudent design of the water jacket, when also the magnets losses have been included into the amount of heat that should be dissipated by the coolant. But the temperatures maps shows that the major part of the PMs losses are actually dissipated in the air gap and in the rotor holes. Thus, while the slot insulating material are thermally safeguarded, the PMs are a bit hotter ($130°C$) than the threshold prescribed by the IEC standard in the 8 and 10 pole machines. Indeed these motors requires higher feeding frequency, so they present higher PM losses than the 6 pole machine, as reported in Table 4.7 (Section 4.8). Moreover the PM loss density is higher because of the smaller magnets and even the rotor holes have a tighter cross section causing a reduced cooling effect. However the thermal analysis have been done under severe hypothesis: the Joule losses have been concentrated inside the slots and any cooling end effect has been neglected. Therefore all the three machines can be considered thermally safeguarded in steady state operation.

5.3 Lumped parameter thermal network: transient thermal analysis

A lumped parameter equivalent thermal network (LPTN) [45] has been implemented in Simulink® to analyze the step response to rated load and the transient thermal behavior during the transportation duty cycle. The equivalent thermal circuit is shown in Figure 5.6. All the lumped parameters have been evaluated with analytical expressions. A detailed description is listed below. The material thermo-physics properties used in the computations are reported in Table 5.3. It is important to underline that the model has been referred only to a slot pitch, thus some parameters have been divided or multiplied by the number of slots Q_S.

- **Slot resistance**

$$R_{slot} = \frac{h_{si}}{2\lambda_{slot}(h_{si} + w_{se})L_{stk}}$$

The equivalent thermal conductivity λ_{slot} is the same computed with Equation 5.7.

Table 5.3: Thermo-physics properties of the materials used in the simualtions.

Parameter	**Symbol**	**Unit**	**Value**
Air at 40°C and atm. pressure			
Density	γ_{air}	$[kg/m^3]$	1.128
Dynamic viscosity	μ_{air}	$[kg/m\,s]$	$1.91 \cdot 10^{-5}$
Kinematic viscosity	ν_{air}	$[m^2/s]$	$1.70 \cdot 10^{-5}$
Specific heat capacity	$c_{p_{air}}$	$[J/kg°C]$	1007
Thermal conductivity	λ_{air}	$[W/m°C]$	0.027
Prandtl number	Pr_{air}	[/]	0.712
Copper			
Density	γ_{Cu}	$[kg/m^3]$	8900
Specific heat capacity	c_{Cu}	$[J/kg°C]$	382
Thermal conductivity	λ_{Cu}	$[W/m°C]$	386
Enamel and epoxy resin			
Density	γ_{res}	$[kg/m^3]$	1100
Specific heat capacity	c_{res}	$[J/kg°C]$	1000
Thermal conductivity	λ_{res}	$[W/m°C]$	0.20
Slot insulation			
Thermal conductivity	λ_{ins}	$[W/m°C]$	0.18
Iron			
Density	γ_{fe}	$[kg/m^3]$	7900
Specific heat capacity	c_{fe}	$[J/kg°C]$	460
Thermal conductivity	λ_{fe}	$[W/m°C]$	58
Inox steel			
Thermal conductivity	λ_{inox}	$[W/m°C]$	17
Fiberglass bandage			
Thermal conductivity	λ_{band}	$[W/m°C]$	0.045
Permanent magnet			
Density	γ_{pm}	$[kg/m^3]$	7500
Specific heat capacity	c_{pm}	$[J/kg°C]$	502
Thermal conductivity	λ_{pm}	$[W/m°C]$	8.96

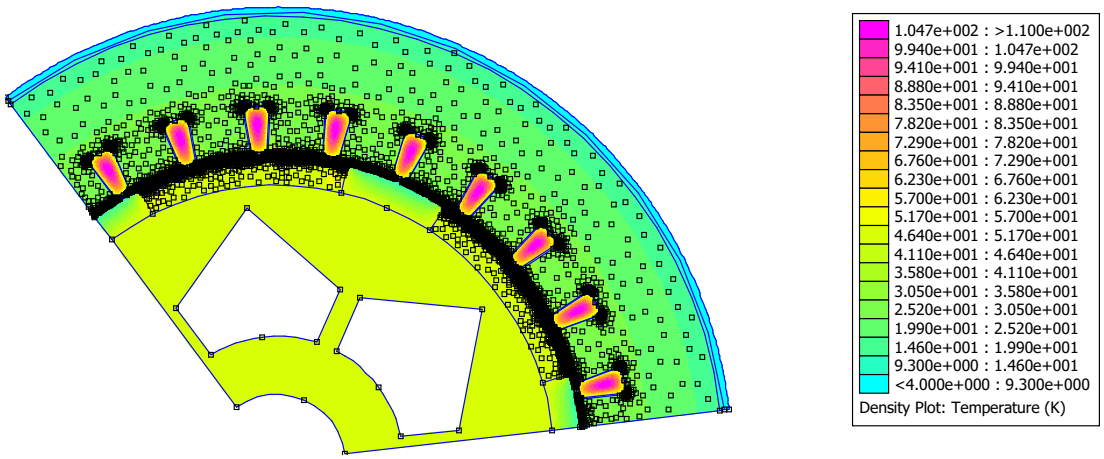

Figure 5.3: 6 pole machine: temperature map on rated load.

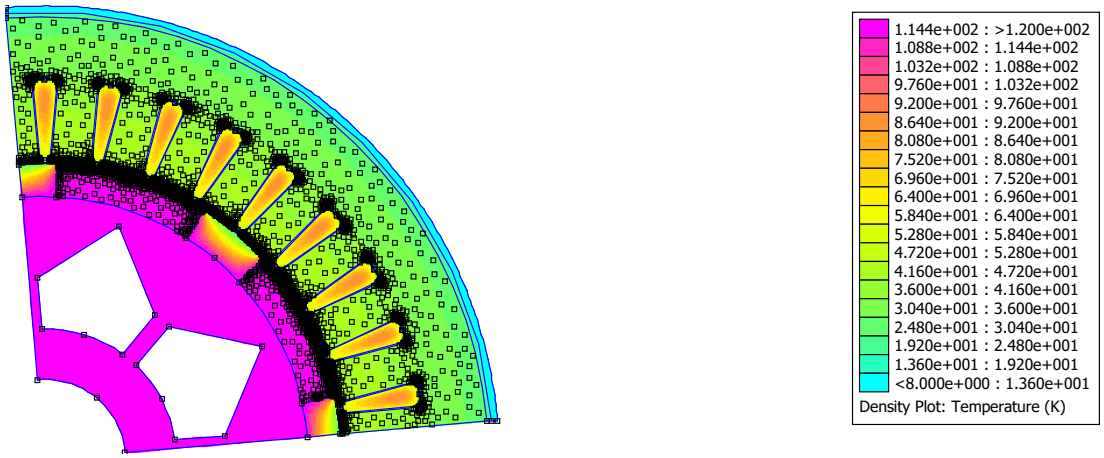

Figure 5.4: 8 pole machine: temperature map on rated load.

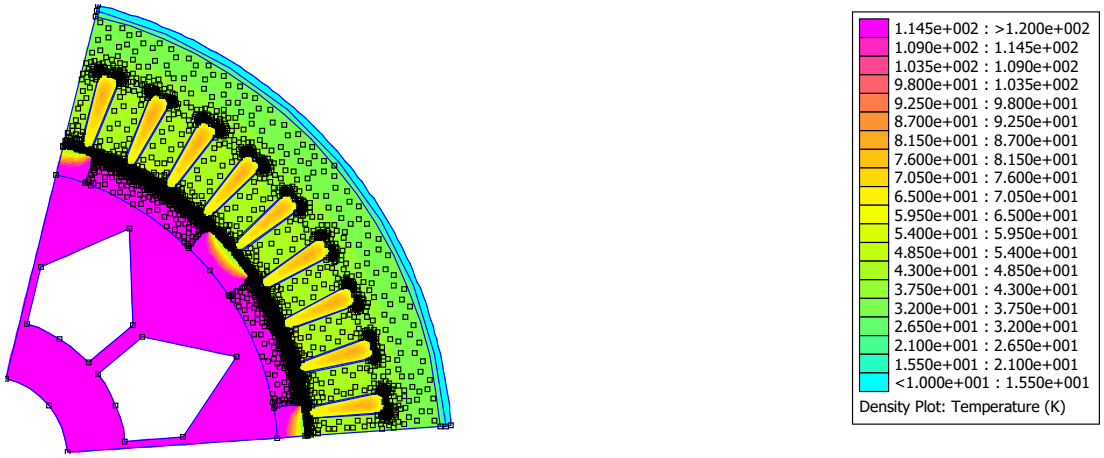

Figure 5.5: 10 pole machine: temperature map on rated load.

- **Slot capacity**

$$C_{slot} = \frac{c_{Cu} G_{Cu}}{Q_s} + \gamma_{res} c_{res} S_{slot} L_{stk} (1 - k_{fill})$$

It can be seen that the capacity of the end-winding, which is very relevant, has been included too. Indeed G_{Cu} is the overall copper weight (Table 3.10, Section 3.9).

- **Slot insulating layers**

$$R_{ins_{lat}} = \frac{t_{ins}}{\lambda_{ins} h_{si} L_{stk}}$$

$$R_{ins_{up}} = \frac{t_{ins}}{\lambda_{ins} w_{se} L_{stk}}$$

$$R_{wed} = \frac{h_{wed}}{\lambda_{ins} w_s L_{stk}}$$

- **Tooth resistance**

$$R_t = \frac{h_s}{\lambda_{fe} w_t L_{fe}}$$

- **Tooth capacity**

$$C_{fe_t} = \frac{c_{fe} G_{fe_t}}{Q_s}$$

- **Back iron resistance**

$$R_{bi} = \frac{Q_s h_{bi}}{\lambda_{fe} \pi (D_e - h_{bi}) L_{fe}}$$

- **Back iron capacity**

$$C_{fe_{bi}} = \frac{c_{bi} G_{fe_{bi}}}{Q_s}$$

- **Contact resistance**

$$R_{cont} = \frac{Q_s t_{cont}}{\lambda_{cont} \pi D_e L_{stk}}$$

Where $t_{cont} = 2\,[mm]$ and $\lambda_{cont} = 2.47\,[W/m^{\circ}C]$.

- **Water jacket resistance**

$$R_{wj} = \frac{Q_s t_{wj}}{\lambda_{inox} \pi (D_e + t_{wj}) L_{wj}}$$

Where the inox steel thickness has been chosen $t_{wj} = 4\,[mm]$ and the water jacket length is $L_{wj} = 70\,[mm]$.

- **Coolant equivalent convective resistance**

$$R_{cool} = \frac{Q_s}{\alpha_{wj} \pi (D_e + 2 t_{wj}) L_{wj}}$$

Where the coolant convection coefficient α_{wj} is reported in Table 5.2 for each motor.

- **Air gap equivalent resistance**

$$R_{gap} = \frac{Q_s}{\alpha_{gap} \pi (D_s - g + t_{band}) L_{stk}}$$

Where the convective coefficient α_{gap} has been computed using Equation 5.10. This resistance varies with the machine speed because the heat exchange depends on the rotor peripheral velocity, as stated by Equations 5.8-5.9.

- **Fiberglass bandage resistance**

$$R_{band} = \frac{Q_s t_{band}}{\lambda_{band}\pi(D_s - 2g + t_{band})L_{stk}}$$

- **Permanent magnet resistance**

$$R_{pm} = \frac{Q_s t_m}{\lambda_{pm}\pi(D_s - 2g - t_m)L_{stk}}$$

- **Permanent magnet capacity**

$$C_{pm} = \frac{c_{pm}G_{pm}}{Q_s}$$

- **Rotor yoke resistance**

$$R_{rot} = \frac{Q_s(D_s - 2g - 2t_m)}{4\lambda_{fe}\pi(D_e - 2g - 2t_m)L_{fe}}$$

  At the nominator a mean thickness has been assumed, so the previous expression is only an estimation of the actual rotor yoke resistance.

- **Rotor yoke capacity**

$$C_{rot} = \frac{c_{fe}G_{fe_{rot}}}{Q_s}$$

- **Rotor hole equivalent convective resistance**

$$R_{duct} = \frac{1}{\alpha_{rot}d_{rot}L_{stk}}$$

  Also this resistance varies with the rotor speed, as expressed by Equations 5.11-5.12.

The heat sources depend on the machine working point, i.e. on the motor torque and speed, according to the losses maps presented in Sections 4.6-4.8. The circuit is linear: any relation between temperature and Joule losses and any thermal effect on the PMs performances has been neglected.

The step responses of the slot and PM overtemperatures have been obtained by imposing the rated current and the rated speed. The results are reported in Figures 5.7-5.8-5.9 for each motor. It can be seen that the temperature maps computed with FEMM match well the steady state values calculated with the LPN for the slot overtemperatures, but they differ a lot in the PM outputs, especially for the 8 and 10 pole machines. Such difference could be caused by the rough estimation of the rotor yoke resistance and rotor hole cooling phenomenon. Furthermore the PM losses are considered concentrated in the middle of the magnet in the LPN, while the actual distribution of the loss density may be far from being uniform. From the step responses the thermal time constant τ_{th} of the three machines has been derived by looking at the time instant when the slot overtemperatue reach the 63.2% of the steady state value. The time constant results about 300 $[s]$ for all the motors (a bit higher for the 6 pole machine). This value is much lower than the range chosen to define the torque specification for the machines preliminary sizing, i.e. $800 \div 1000$ $[s]$. This is due mainly to the compactness of the designed motors, which have a volume and a weight that lead to reduced heat capacity and do not allow high thermal time constants. It can be also noted that the step responses of the PM overtemperatures have a higher time constant.

The slot and PM overtemperatures during the transportation duty cycle have been obtained by imposing the torque and speed trends of this operation. The outcomes are reported in Figures 5.10-5.11-5.12. Despite the thermal time constant is much lower than the expected one, the slot overtemperature reach a peak value below $140°C$, which can be considered the maximum limit that the H class insulating materials can withstand. Nevertheless the safety

margin suggested by The IEC standard is overcome. So, adopting a conservative way, the machine overload capability should be limited or insulating materials that belong to a superior thermal class should be used. On the other hand, in the former case the vehicle performances in terms of power and acceleration will be reduced, while in the latter case the motor will be more expensive. The first solution may be the best compromise because in farming tractors high torque values are needed more often in steady state operations (e.g. to drive some high power tools through the PTO or to drag plowing implements) than to achieve high acceleration.

In the end, after the presented results from the thermal analysis and the related consideration, it can be stated that the designed motors are not able to provide the same performances of the traditional powertrain without the risk of overtemperature damages. Nevertheless, if a small reduction in the torque performances can be accepted, all the three machines can safely work in the hybrid powertrain. The temperature trends during the other duty cycles are reported in Figures from 5.13 to 5.21. Plowing duty cycles and power harrowing do not present any thermal problem.

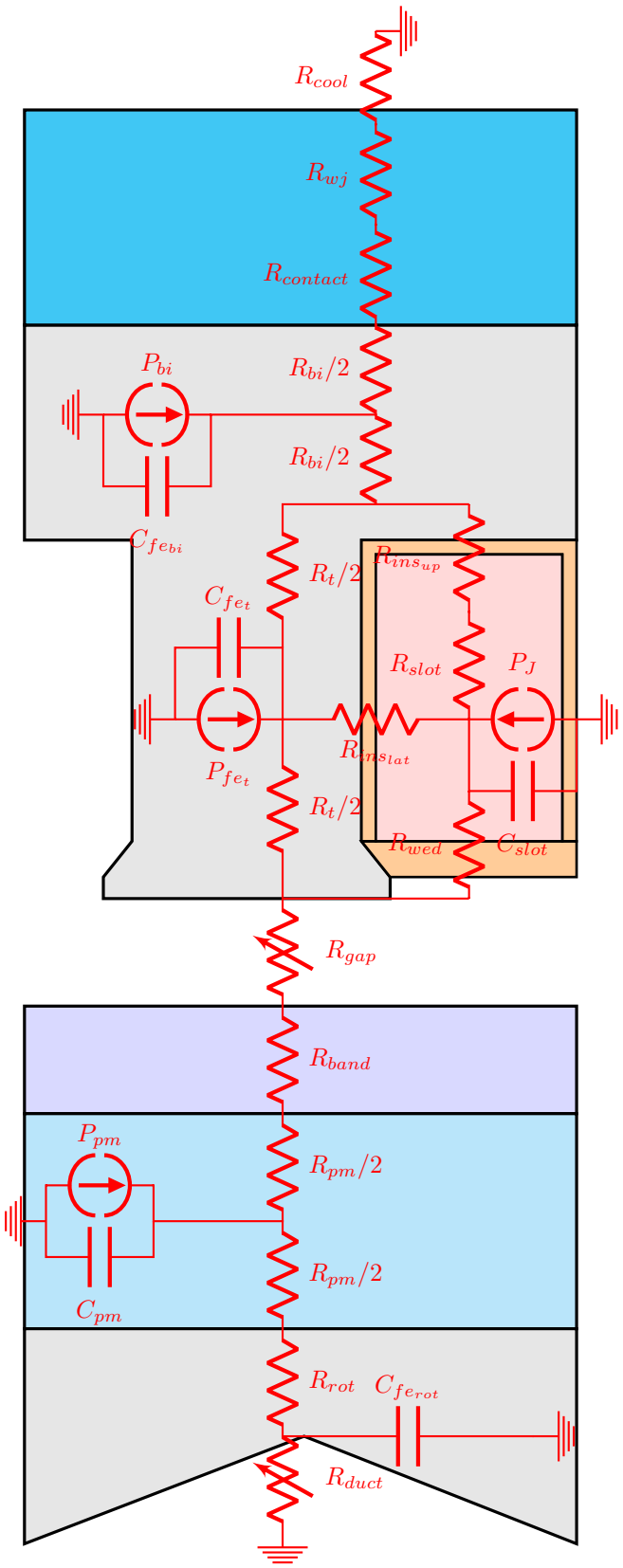

Figure 5.6: Thermal equivalent network.

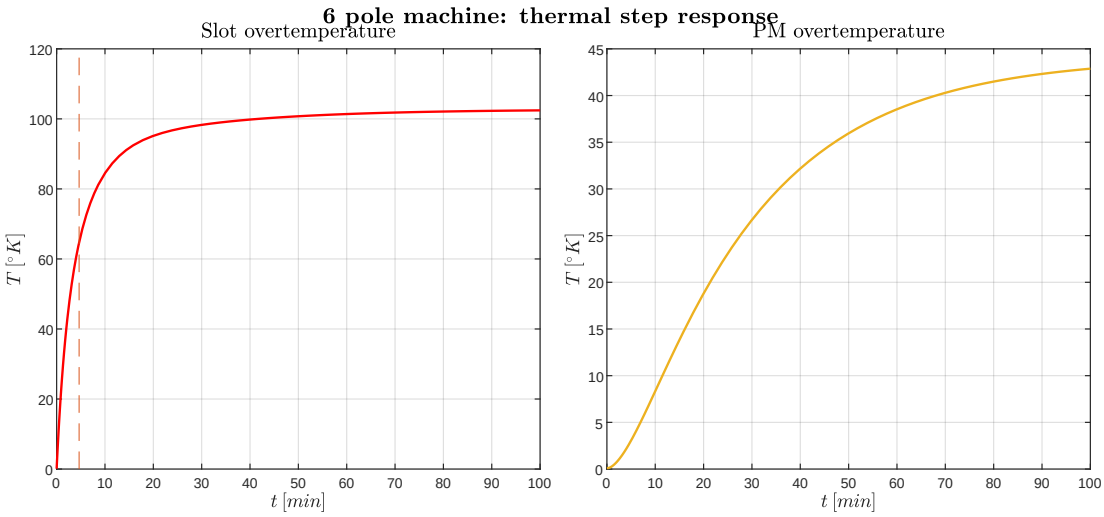

Figure 5.7: 6 pole machine: thermal step response.

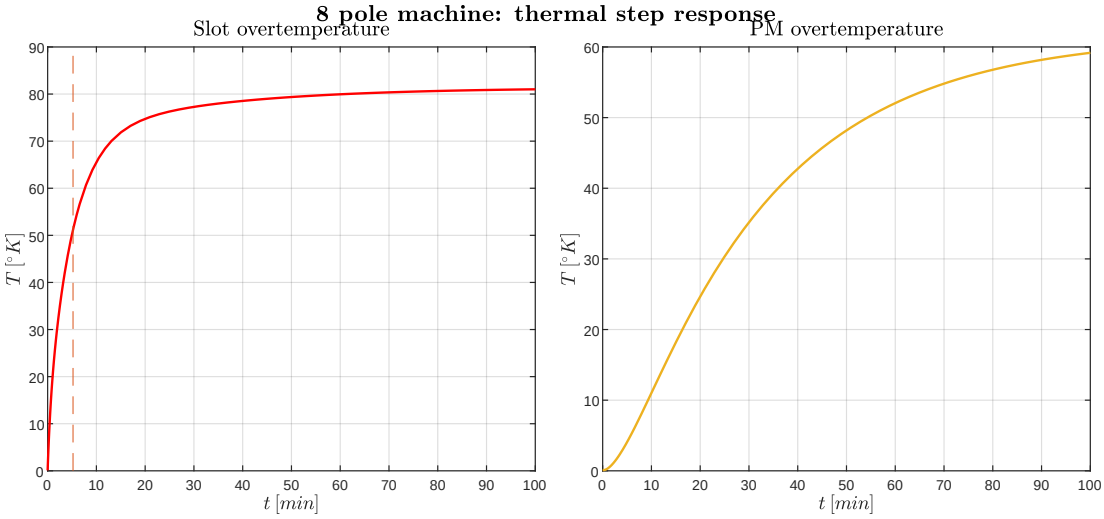

Figure 5.8: 8 pole machine: thermal step response.

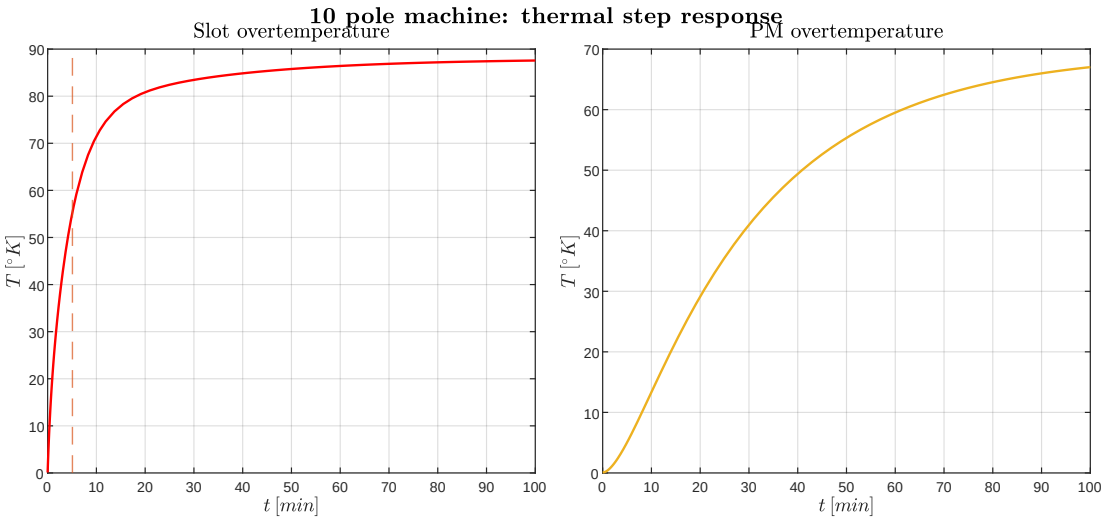

Figure 5.9: 10 pole machine: thermal step response.

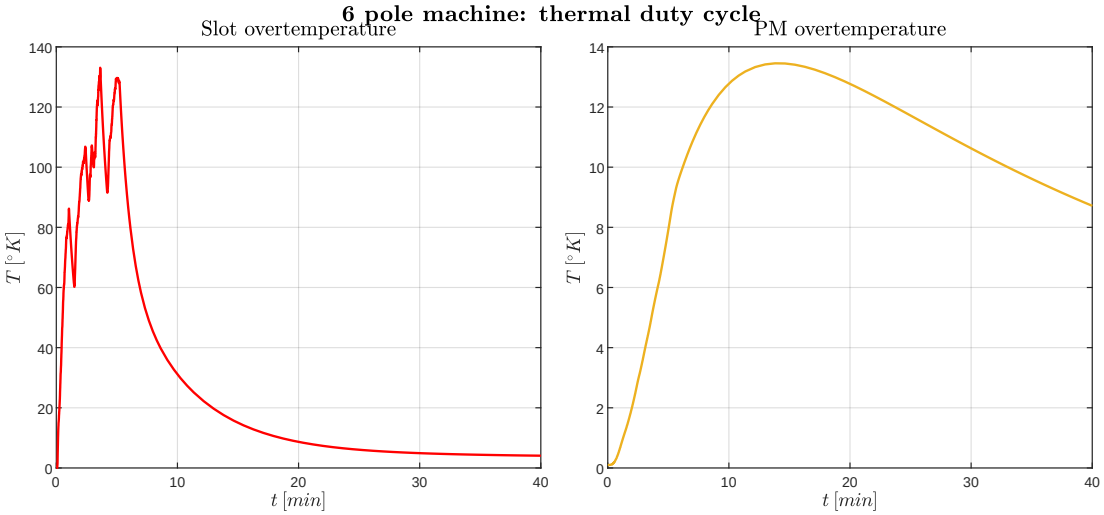

Figure 5.10: 6 pole machine: temperature trend during the **transportation** duty cycle.

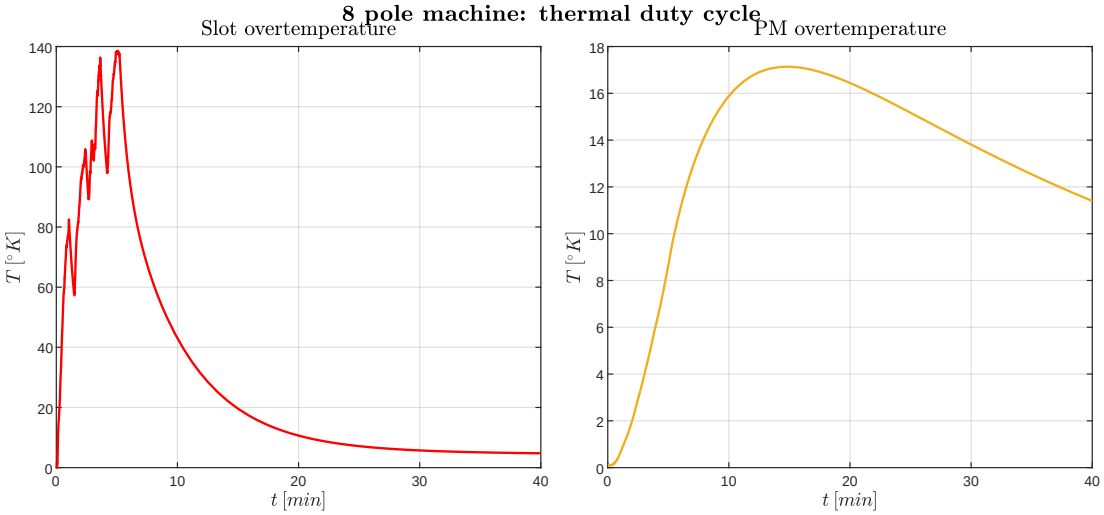

Figure 5.11: 8 pole machine: temperature trend during the **transportation** duty cycle.

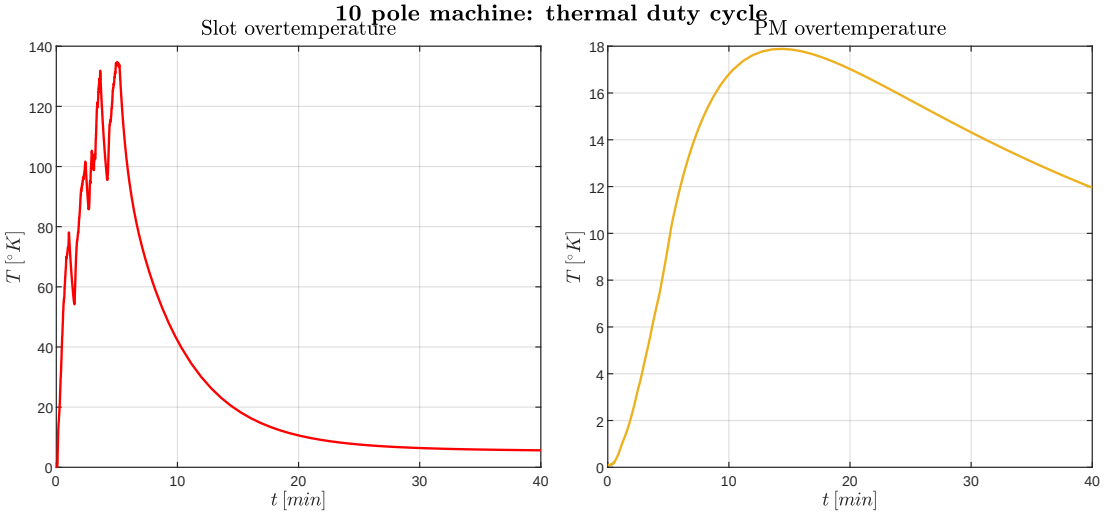

Figure 5.12: 10 pole machine: temperature trend during the **transportation** duty cycle.

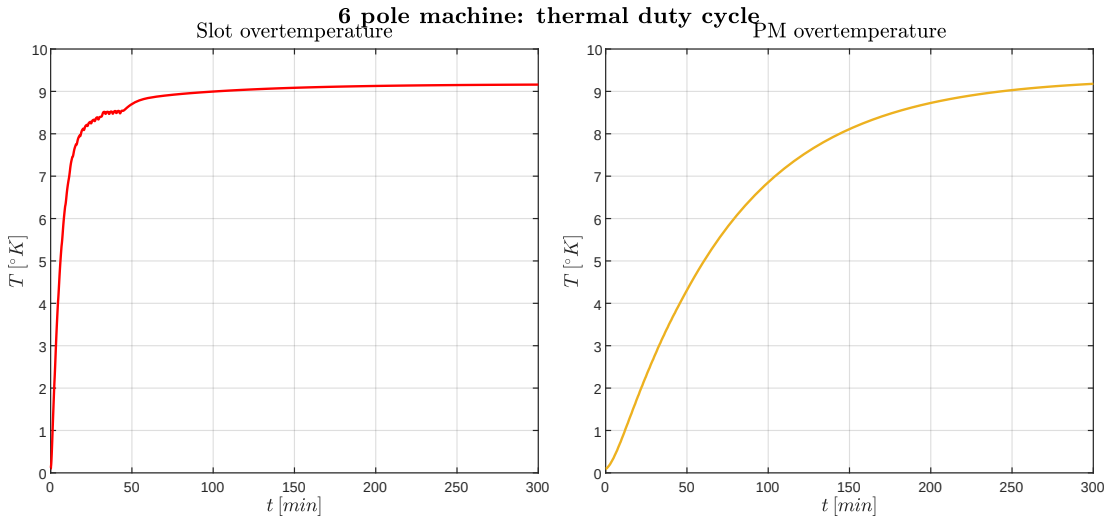

Figure 5.13: 6 pole machine: temperature trend during the **plough 60** duty cycle.

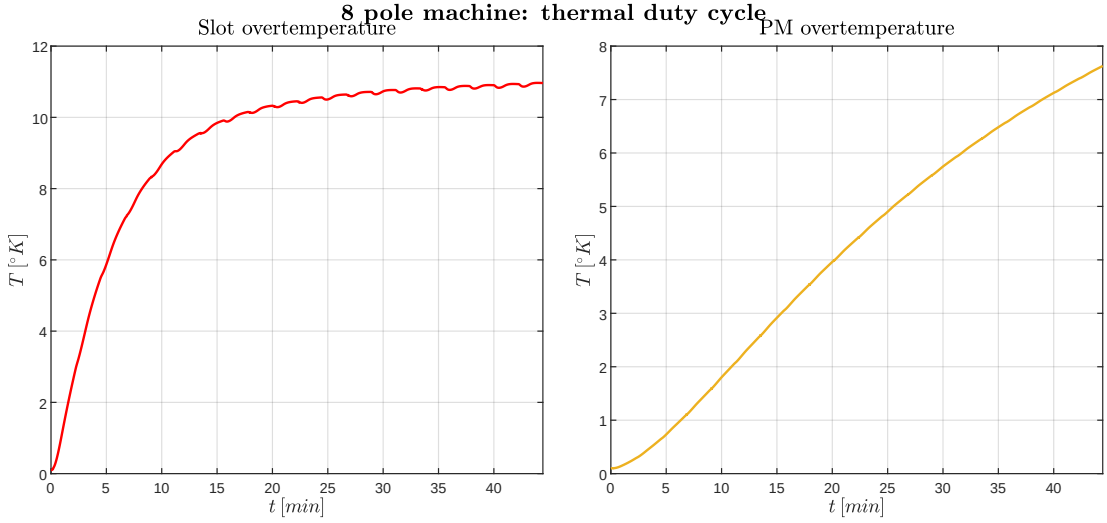

Figure 5.14: 8 pole machine: temperature trend during the **plough 60** duty cycle.

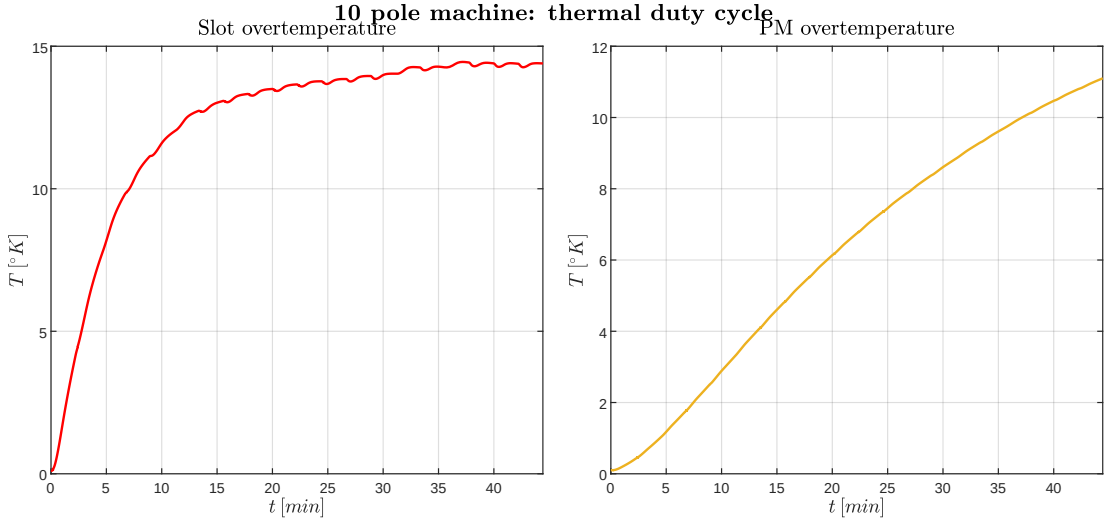

Figure 5.15: 10 pole machine: temperature trend during the **plough 60** duty cycle.

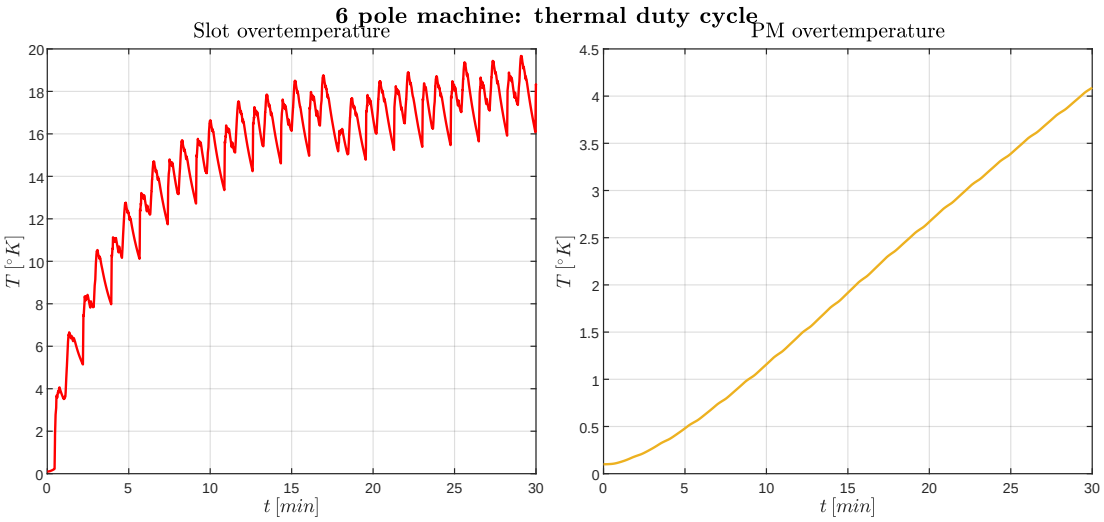

Figure 5.16: 6 pole machine: temperature trend during the **plough 100** duty cycle.

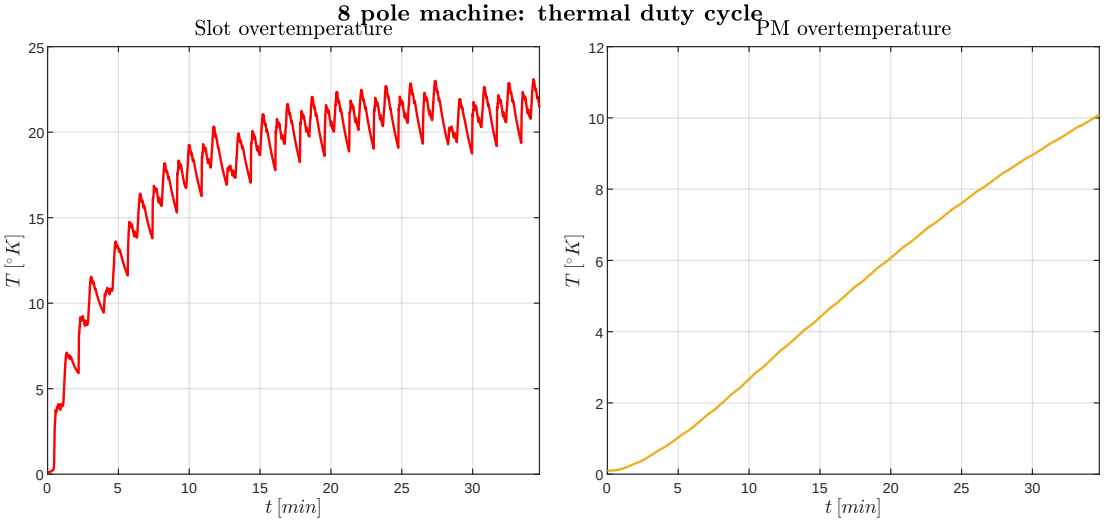

Figure 5.17: 8 pole machine: temperature trend during the **plough 100** duty cycle.

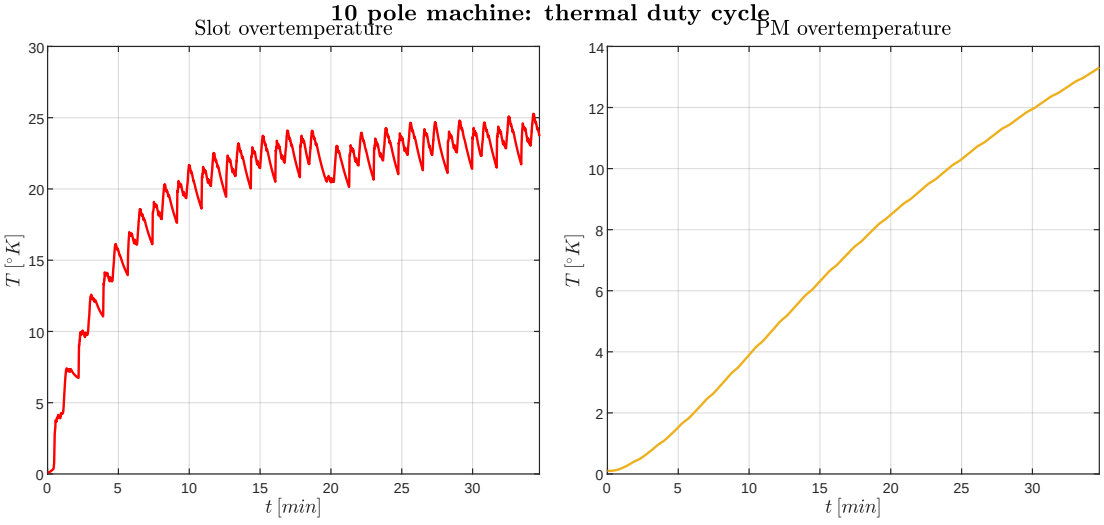

Figure 5.18: 10 pole machine: temperature trend during the **plough 100** duty cycle.

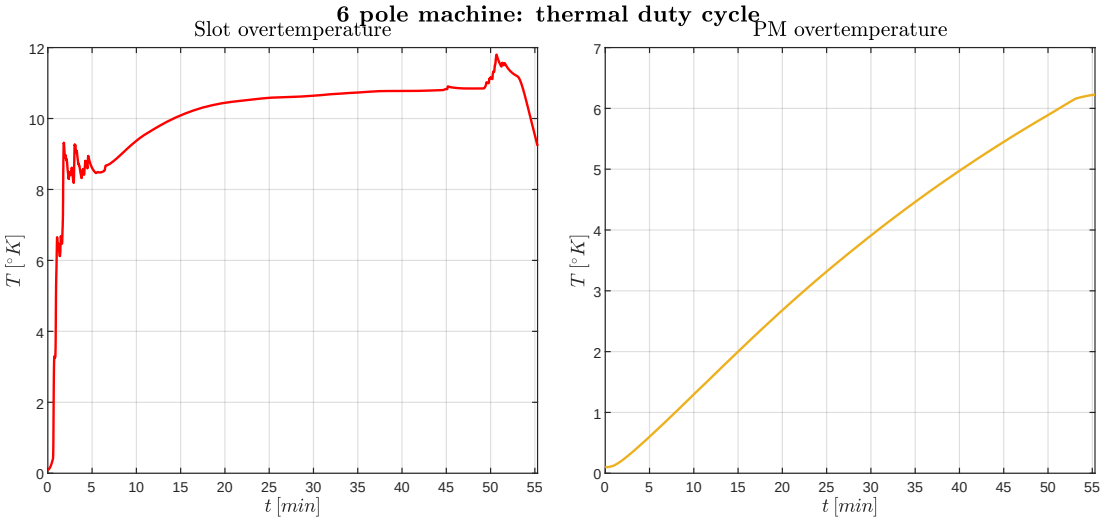

Figure 5.19: 6 pole machine: temperature trend during the **power harrow** duty cycle.

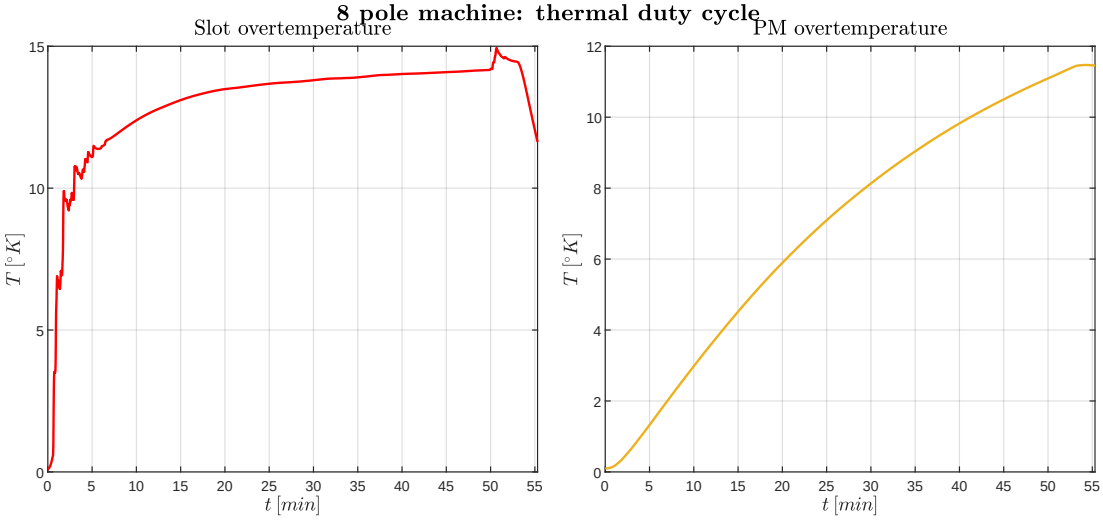

Figure 5.20: 8 pole machine: temperature trend during the **power harrow** duty cycle.

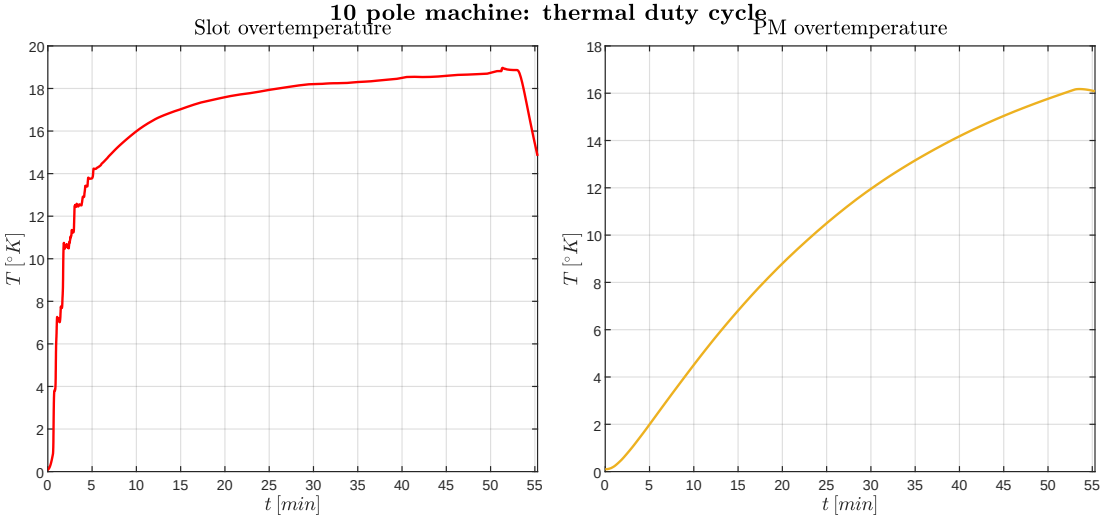

Figure 5.21: 10 pole machine: temperature trend during the **power harrow** duty cycle.

Conclusion

This work has faced the powertrain electrification for a 280 $[Hp]$ open field farming tractor.

A mild-hybrid parallel architecture with a power management based on a simple threshold logic has been chosen. It has been presented how the torque and speed trends can be found out by modeling the power balance at the engine shaft with a one-mesh mechanical circuit which takes as sources some duty cycles of the original powertrain, whose quantities must be referred to the engine shaft. To simulate a few hybrid powertrains the original ICE has been supposed and consequently three downsized engines have been chosen. It has been described how and how much the mechanical characteristic of the original ICE can be inferred from available measurements of torque and speed taken at the engine shaft during real working conditions. The torque specifications needed to begin the preliminary sizing of the EM have been chosen using the thermal equivalent torque method, that has been implemented by processing the output of the mechanical circuit model with a low-pass filter. Hence a thermal time constant has been supposed to select the wanted specifications at rated load and maximum overload. Moreover the size constrains and other requirements given by the chosen hybrid architecture have been identified and severely taken into account in the EM design.

Three SPM motor with different number of poles has been designed. The preliminary sizing procedure has been oriented to the cost-effectiveness of the machines as much as possible, without forget the wanted performances and the imposed constrains. The displacement limitation in particular has been very challenging and a dedicated preliminary sizing method has been developed to cope with it. Various sizing attempts have been made for each number of pole varying the magnet grade (NdFeB), the number of slots and the magnet thickness. The main dimensions of the machines as well as the number of slots and the magnet parameters have been finally chosen among several chances. Distributed fractional-slot winding with copper wire conductors have been preferred for all the three motors. Then the stator and the rotor stacks have been designed and the material costs have been compared between the three motors.

Detailed electromagnetic analysis have been done on the three designed machines using both analytical estimations and finite element analysis. The unload behavior as well as the on-load performances are satisfactory: all the three motors generates sinusoidal *emfs* with low harmonic contents and the cogging torque is very limited thanks to the chosen winding layout; the rated torque specifications and the overload capabilities are fulfilled with acceptable ripples. The machines are less saturated than expected, so they result a bit oversized in terms of power capabilities and they require a lower feeding voltage. Thus in further designs it is suggested to size the conductor for a lower current and a higher voltage keeping the induction under 2 $[T]$ also at maximum overload. In this way the voltage capabilities of power electronic components can be better exploited and the overall Joule losses in the electric drive are reduced. The losses and the efficiency of the three motors have been mapped carefully. The iron and permanent magnet losses in particular have been computed through a series of FEA considering all the losses contributions.

In the end the thermal behavior of the machines have been tested both at steady state and under a real duty cycle. A thermal FEA has been implemented to obtained the temperature map under rated load at steady state, while the transient simulations have been done by solving an equivalent lumped parameters thermal network, where both the stator and rotor have been taken into account. Despite the actual thermal time constants outcomes far below than the values supposed before the preliminary sizing, the slot overtemperature remains under the maximum value of $140°C$ even in the most critical duty cycle. Nevertheless the safety mar-

gin recommended by the IEC standard is overcome. So, to avoid damages on the insulating materials, it is recommended to limit the overload capability of the EM. The acceleration performances of the vehicle will be affected but they are not fundamental in farming tractors. The slot overtemperatures during the other operations remain under the safety margin of $125°C$ recommended for H class insulating materials. No issues come from the magnets, although the steady state temperatures computed with FEA are higher than expected in the 8 and 10 pole machines, due to the higher magnets loss density.

The purpose of this project is to assess the feasibility of the electric motors design through the equivalent thermal torque method in an application not yet deeply studied. As a beginning investigation, it offers many further developments. Different hybrid powertrains can be considered as well as different power management systems. Moreover, even with the same architecture presented in this thesis, it is possible to choose different specifications for the EM sizing and other type of electrical machines can be designed, analyzed and compared. Furthermore the inverter and battery pack sizing has not been covered in this work, but from the few information given it can be stated that also their design is not straightforward. Finally the complexity of the application presented in this project involves many engineering fields: a careful mechanical redesign of the clutches, flanges and engine shaft is needed; the vehicle control system requires heavy modification; energy consumption evaluations and performances analysis should be done on a detailed model of the tractor to compare different powertrains and different couplings between engines and electric motors. In addition the definition of proper standard duty cycles based on agriculture characteristic operations could make further electrification projects easier and it could boost the industrialization of electrified agricultural machinery.

This thesis provides valid suggestions and practical examples about the design of SPM motors for a hybrid farming tractor. Despite the achieved results, there is still a lot of work to do in this field.

Appendix

This appendix reports extract from the NdFeB magnets datasheet and the technical drawings of the three designed motors. Figures are not labeled.

Nxx?? Material		Br		Hc (Hcb)		Hci (Hcj)		BHmax	
		mT	G	kA/m	Oe	kA/m	Oe	kJ/m^3	MGOe
N45	H	1,320	13,200	995	12,500	1,353	17,000	342	43
N48	H	1,370	13,700	995	12,500	1,353	17,000	366	46
N50	H	1,400	1,400	995	12,500	1353	17,000	382	48
N27	SH	1,030	10,300	804	10,100	1,592	20,000	199	25
N30	SH	1,080	10,800	804	10,100	1,592	20,000	223	28
N33	SH	1,130	11,300	844	10,600	1,592	20,000	247	31
N35	SH	1,170	11,700	875	11,000	1,592	20,000	263	33
N38	SH	1,210	12,100	907	11,400	1,592	20,000	286	36
N40	SH	1,240	12,400	939	11,800	1,592	20,000	302	38
N42	SH	1,280	12,800	963	12,100	1,592	20,000	318	40
N45	SH	1,320	13,200	1,003	12,600	1,592	20,000	342	43
N27	UH	1,030	10,300	764	9,600	1,989	25,000	199	25
N30	UH	1,080	10,800	812	10,200	1,989	25,000	223	28
N33	UH	1,130	11,300	851	10,700	1,989	25,000	247	31
N35	UH	1,170	11,700	875	11,000	1,989	25,000	263	33
N38	UH	1,210	12,100	875	11,000	1,989	25,000	287	36
N40	UH	1,240	12,400	899	11,300	1,989	25,000	302	38
N42	UH	1,280	1,280	875	11,000	1,989	2,500	318	40
N27	EH	1,030	10,300	780	9,800	2,387	30,000	199	25
N30	EH	1,080	10,800	812	10,200	2,387	30,000	223	28
N33	EH	1,130	11,300	836	10,500	2,387	30,000	247	31

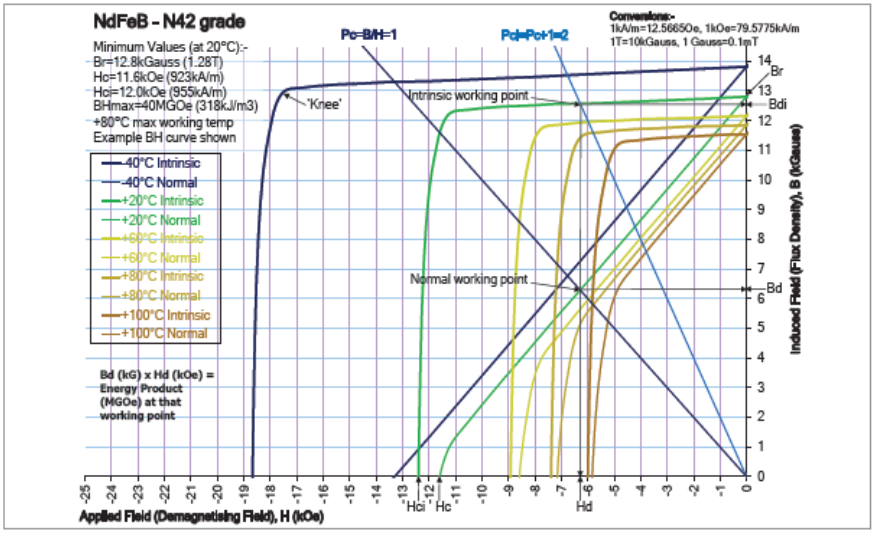

SEZ. A-A'

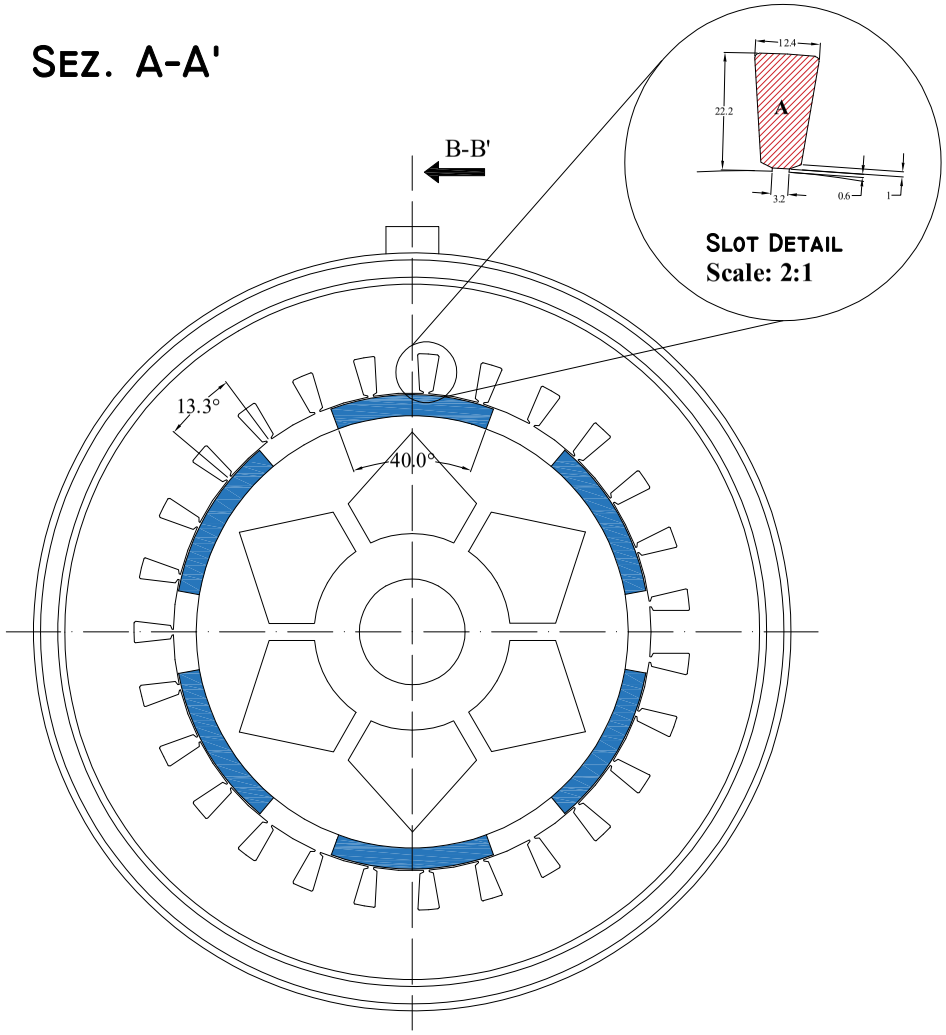

SEZ. B-B'

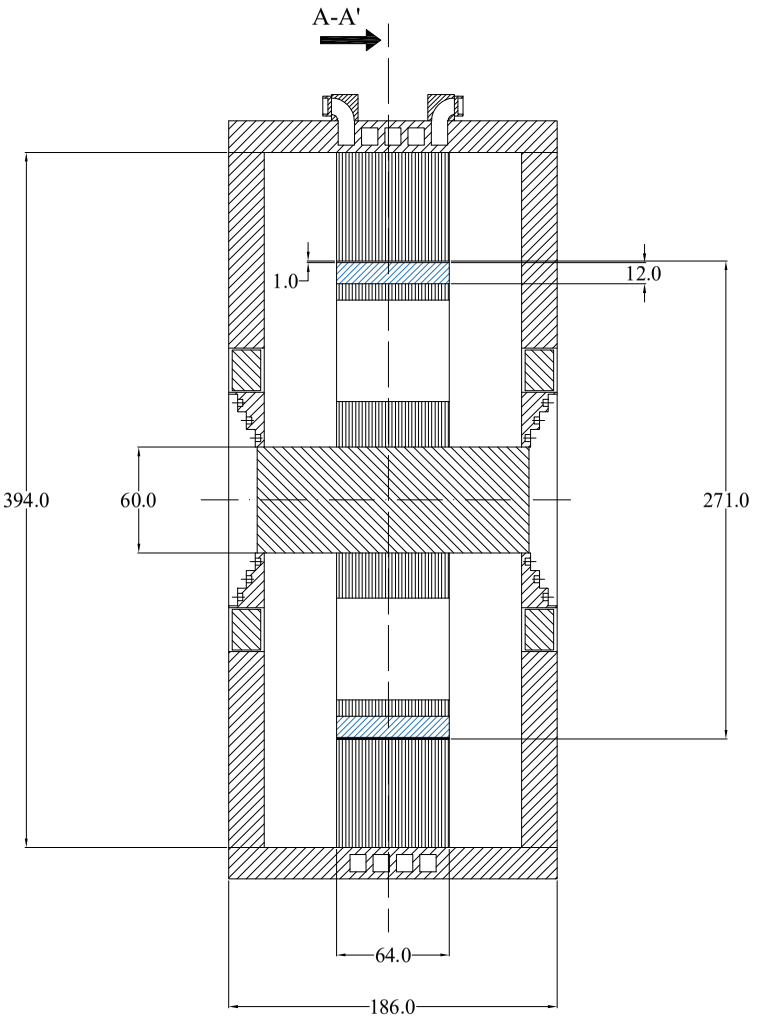

2p	D_s	D_e	Q_s	w_t	A
6	271	394	27	24.3	212

Gauge: M350-50A

SCALE: 1:2

Author: Elia Scolaro

SEZ. A-A'

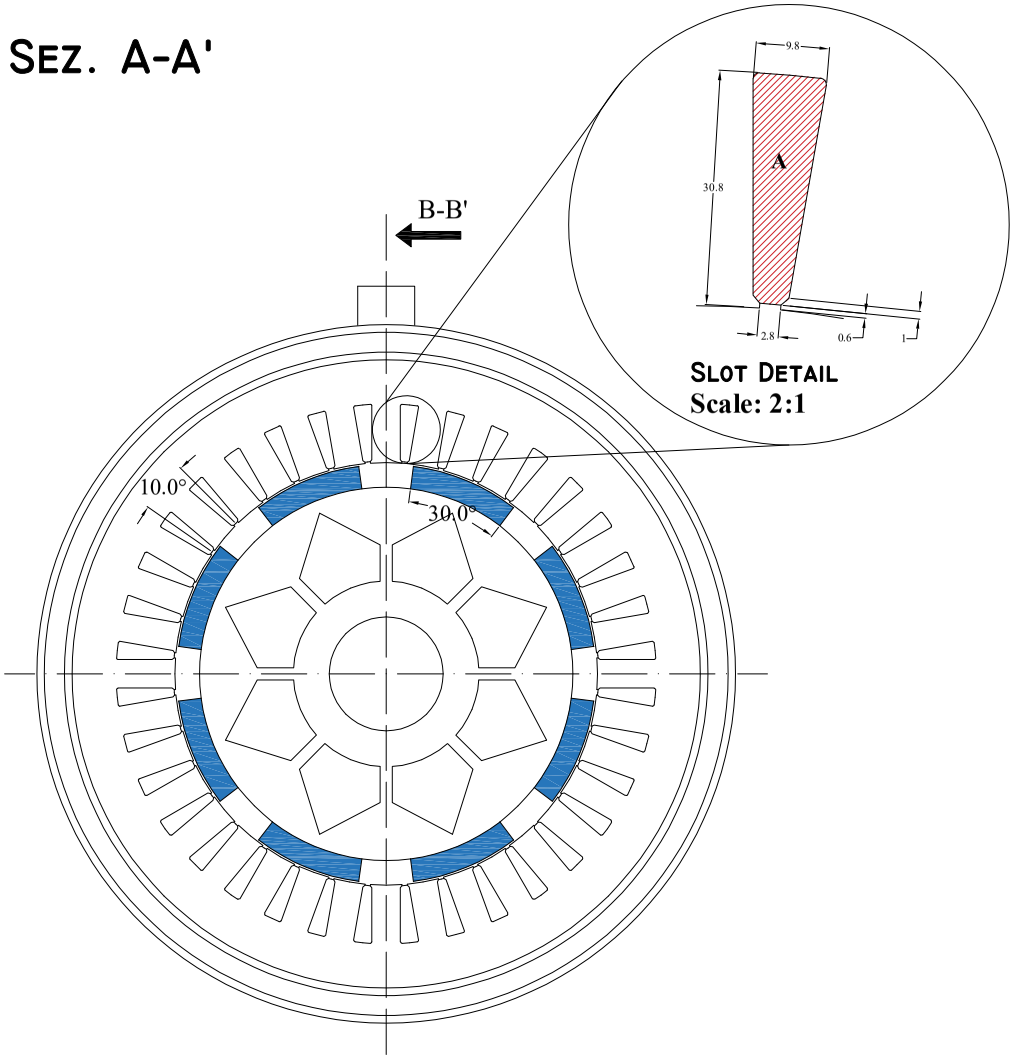

SLOT DETAIL
Scale: 2:1

SEZ. B-B'

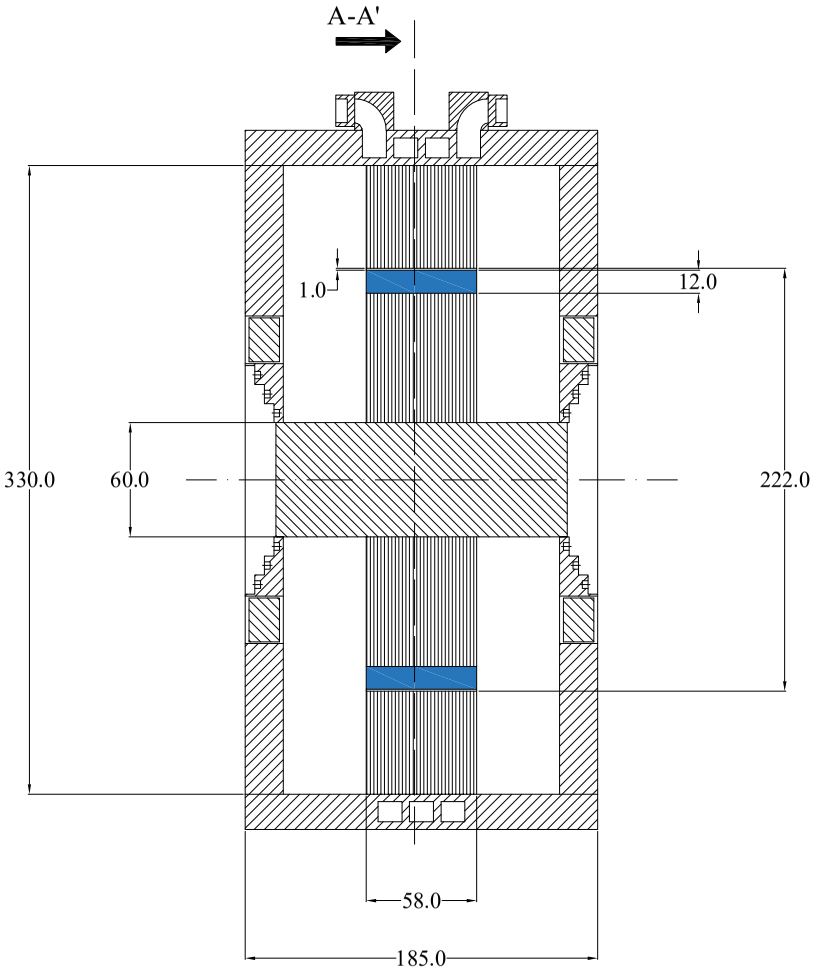

2p	D_s	D_e	Q_s	w_t	A
8	222	330	36	15.0	215

Gauge: M350-50A

SCALE: 1:2

Author: Elia Scolaro

SEZ. A-A'

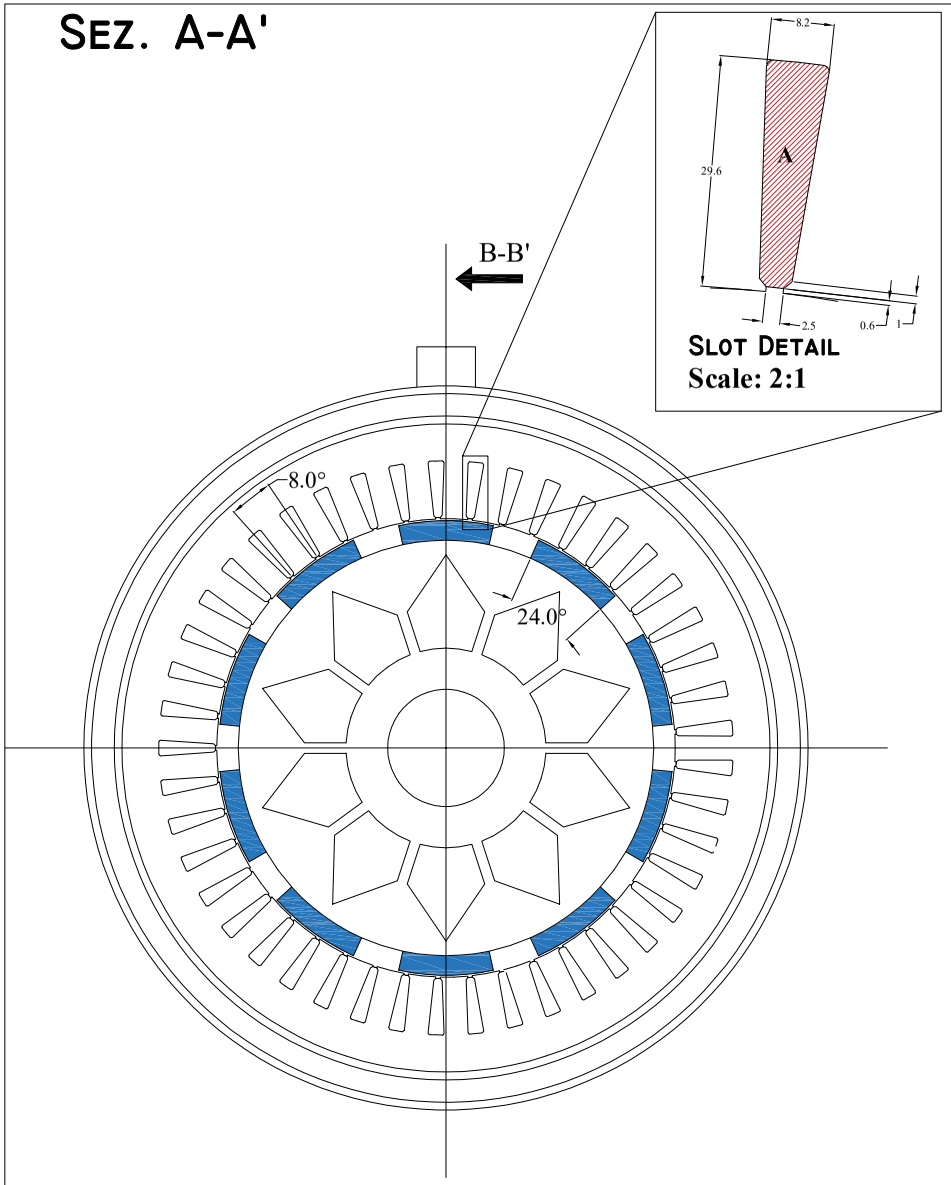

SEZ. B-B'

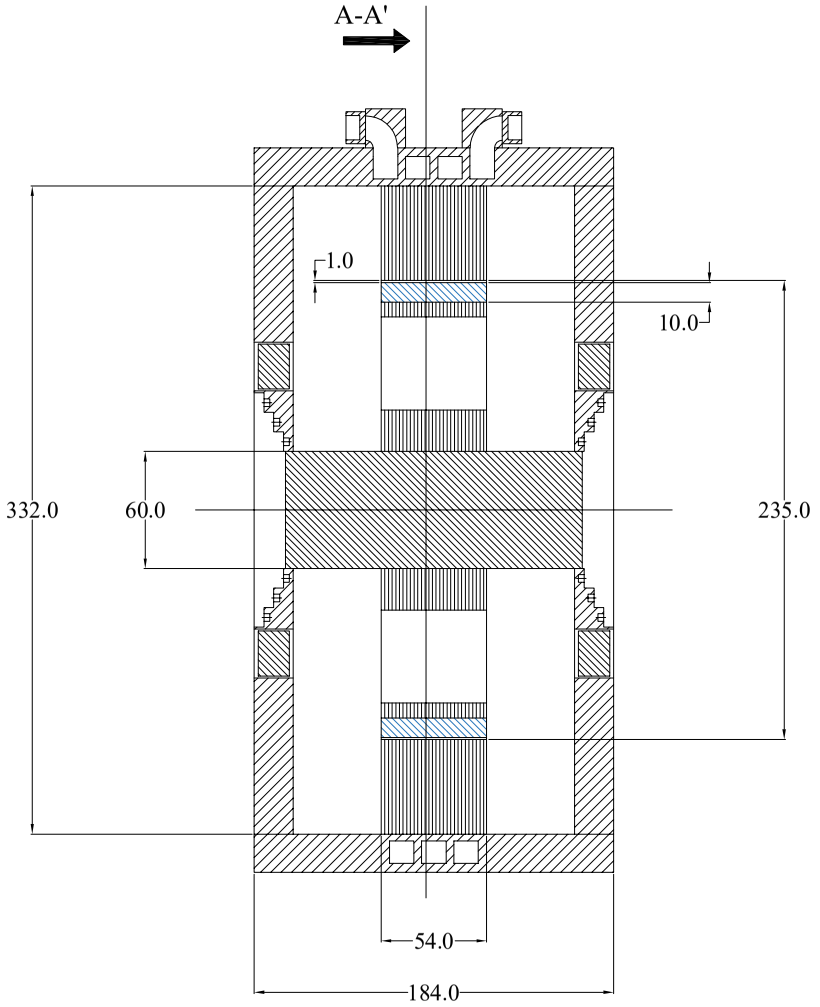

2p	D_s	D_e	Q_s	w_t	A
10	235	332	45	12.4	178

Gauge: M350-50A

SCALE: 1:2

Author: Elia Scolaro

Bibliography

[1] W. Aumer, M. Lindner, M. Geißler, and T. Herlitzius, "Electric tractor: Vision or future?," *Agricultural Engineering*, vol. 63, p. 14–15, Feb. 2008.

[2] J. Flint, D. Zhang, and P. Xu, "Preliminary market analysis for a new hybrid electric farm tractor," in *Proceedings of the 2014 International Conference on Global Economy, Commerce and Service Science*, pp. 98–102, Atlantis Press, 2014/01.

[3] X. Bin, L. Hao, S. Zheng-He, and M. En-Rong, "Powertrain system design of medium-sized hybrid electric tractor," *ITJ: Information Technology Journal*, vol. 23, pp. 7228 – 7233, 2013.

[4] G. Moreda, M. Muñoz-García, and P. Barreiro, "High voltage electrification of tractor and agricultural machinery – a review," *Energy Conversion and Management*, vol. 115, pp. 117 – 131, 2016.

[5] "Eu regulation on non-road vehicles emissions." https://dieselnet.com/standards/eu. Accessed: 2020-09-01.

[6] "Us regulation on non-road vehicles emissions." https://www.epa.gov/regulations-emissions-vehicles-and-engines/regulations-emissions-nonroad-vehicles-and-engines. Accessed: 2020-09-01.

[7] J. Barthel, D. Gorges, M. Bell, and P. Munch, "Energy management for hybrid electric tractors combining load point shifting, regeneration and boost," in *2014 IEEE Vehicle Power and Propulsion Conference (VPPC)*, pp. 1–6, 2014.

[8] S. Grammatico, A. Balluchi, and E. Cosoli, "A series-parallel hybrid electric powertrain for industrial vehicles," in *Vehicle Power and Propulsion Conference (VPPC), 2010 IEEE*, pp. 1–6, 2010.

[9] M. G. de Soto, L. Emmia, C. Benavides, I. Garcia, and P. G. de Santos, "Reducing air pollution with hybrid-powered robotic tractors for precision agriculture," *Biosystems Engineering*, vol. 143, pp. 79 – 94, 2016.

[10] D. Troncon, L. Alberti, S. Bolognani, F. Bettella, and A. Gatto, "Electrification of agricultural machinery: a feasibility evaluation," in *2019 Fourteenth International Conference on Ecological Vehicles and Renewable Energies (EVER)*, pp. 1–7, 2019.

[11] R. R. Melo, F. L. M. Antunes, S. Daher, H. H. Vogt, D. Albiero, and F. L. Tofoli, "Conception of an electric propulsion system for a 9 kw electric tractor suitable for family farming," *IET Electric Power Applications*, vol. 13, pp. 1993–2004, 2019.

[12] A. Lajunen, P. Sainio, L. Laurila, J. Pippuri-Mäkeläinen, and K. Tammi, "Overview of powertrain electrification and future scenarios for non-road mobile machinery," *Energies*, vol. 11, p. 1184, 05 2018.

[13] M. Ehsani, Y. Gao, and A. Emadi, *Modern electric, hybrid electric, and fuel cell vehicles: fundamentals, theory, and design.* CRC press, 2009.

[14] H. Gao and J. Xue, "Modeling and economic assessment of electric transformation of agricultural tractors fueled with diesel," *Sustainable Energy Technologies and Assessments*, vol. 39, p. 100697, 2020.

[15] D. Troncon and L. Alberti, "Case of study of the electrification of a tractor: Electric motor performance requirements and design," *Energies*, vol. 13, p. 2197, May 2020.

[16] O. Lagnelöv, G. Larsson, D. Nilsson, A. Larsolle, and P.-A. Hansson, "Performance comparison of charging systems for autonomous electric field tractors using dynamic simulation," *Biosystems Engineering*, vol. 194, pp. 121 – 137, 2020.

[17] "Finite element method magnetics: website homepage." http://www.femm.info/wiki/HomePage. Accessed: 2020-09-01.

[18] O. D. Momoh and M. O. Omoigui, "An overview of hybrid electric vehicle technology," in *2009 IEEE Vehicle Power and Propulsion Conference*, pp. 1286–1292, 2009.

[19] M. Kebriaei, A. H. Niasar, and B. Asaei, "Hybrid electric vehicles: An overview," in *2015 International Conference on Connected Vehicles and Expo (ICCVE)*, pp. 299–305, 2015.

[20] A. Somà, F. Bruzzese, and E. Viglietti, "Hybridization factor and performances of hybrid electric telescopic heavy vehicles," in *2015 Tenth International Conference on Ecological Vehicles and Renewable Energies (EVER)*, pp. 1–9, 2015.

[21] K. Nevala, J. Penttinen, and P. Saavalainen, "Developing of the anti-slip control of hydrostatic power transmission for forest tractor and optimisation of the power of diesel engine," in *AMC'98 - Coimbra. 1998 5th International Workshop on Advanced Motion Control. Proceedings (Cat. No.98TH8354)*, pp. 475–480, 1998.

[22] M. Anwar, M. G. Rasul, and N. Ashwath, "Combustion characteristics of an agricultural diesel engine fuelled with papaya and stone fruit biodiesel: A comparison," in *2019 IEEE 2nd International Conference on Renewable Energy and Power Engineering (REPE)*, pp. 26–31, 2019.

[23] P. Dabove and A. M. Manzino, "Gps mass-market receivers for precise farming," in *2014 IEEE/ION Position, Location and Navigation Symposium - PLANS 2014*, pp. 472–477, 2014.

[24] N. Bianchi and S. Bolognani, *Metodologie di progettazione delle macchine elettriche*. CLEUP, 2001.

[25] C. Jia, W. Qiao, and L. Qu, "Modeling and control of hybrid electric vehicles: A case study for agricultural tractors," in *2018 IEEE Vehicle Power and Propulsion Conference (VPPC)*, pp. 1–6, 2018.

[26] D. Troncon, L. Alberti, and M. Mattetti, "A feasibility study for agriculture tractors electrification: Duty cycles simulation and consumption comparison," in *2019 IEEE Transportation Electrification Conference and Expo (ITEC)*, pp. 1–6, 2019.

[27] "Cummins engines datasheets." https://www.cummins.com/engines/qsm. Accessed: 2020-09-01.

[28] "Perkins engines datasheets." https://www.perkins.com/en_GB/products/new/perkins/industrial/industrial-diesel-engines.html. Accessed: 2020-09-01.

[29] "Deutz engines datasheets." https://www.deutz.com/en/products/engines. Accessed: 2020-09-01.

[30] "Fpt industrial engines datasheets." https://www.fptindustrial.com/global/en/engines/agriculture. Accessed: 2020-09-01.

[31] W. Leonhard, *Control of electrical drives*. Springer, 2001.

[32] Z. Q. Zhu and D. Howe, "Electrical machines and drives for electric, hybrid, and fuel cell vehicles," *Proceedings of the IEEE*, vol. 95, no. 4, pp. 746–765, 2007.

[33] M. Facco, "Progetto di motori a magneti permanenti per powertrain ibrido elettrico di macchina agricola," Master's thesis, Università degli Studi di Padova, Padova, ITA, 2018.

[34] P. Vas, *Sensorless vector and direct torque control*. Oxford Univ. Press, 1998.

[35] "Ferrite magnets datasheet." https://www.eclipsemagnetics.com/media/wysiwyg/datasheets/magnet_materials_and_assemblies/ferrite_ceramic_datasheet.pdf. Accessed: 2020-09-01.

[36] "Alnico magnets datasheet." https://www.eclipsemagnetics.com/media/wysiwyg/datasheets/magnet_materials_and_assemblies/alnico_magnets_datasheet_rev2.pdf. Accessed: 2020-09-01.

[37] "Neodimium magnets datasheet." https://www.eclipsemagnetics.com/media/wysiwyg/datasheets/magnet_materials_and_assemblies/ndfeb_neodymium_iron_boron-standard_ndfeb_range_datasheet_rev1.pdf. Accessed: 2020-09-01.

[38] "Samarium-cobalt magnets datasheet." https://www.eclipsemagnetics.com/media/wysiwyg/datasheets/magnet_materials_and_assemblies/samarium_cobalt_magnets_datasheet.pdf. Accessed: 2020-09-01.

[39] L. Alberti, E. Fornasiero, and N. Bianchi, "Impact of the rotor yoke geometry on rotor losses in permanent-magnet machines," *IEEE Transactions on Industry Applications*, vol. 48, no. 1, pp. 98–105, 2012.

[40] N. Bianchi, *Electrical machine analysis using finite elements.* CRC Press, 2005.

[41] "Rotating losses in a surface mount permanent magnet motor." http://www.femm.info/wiki/SPMLoss. Accessed: 2020-09-01.

[42] D. Ishak, Z. Q. Zhu, and D. Howe, "Eddy-current loss in the rotor magnets of permanent-magnet brushless machines having a fractional number of slots per pole," *IEEE Transactions on Magnetics*, vol. 41, no. 9, pp. 2462–2469, 2005.

[43] "Glycol solution properties." https://www.engineeringtoolbox.com/ethylene-glycol-d_146.html. Accessed: 2020-09-01.

[44] C. Bonacina, A. Cavallini, and L. Mattarolo, *Trasmissione del Calore*. CLEUP, 1992.

[45] P. Shams Ghahfarokhi, A. Kallaste, A. Belahcen, and T. Vaimann, "Analytical thermal model and flow network analysis suitable for open self-ventilated machines," *IET Electric Power Applications*, vol. 14, no. 6, pp. 929–936, 2020.